Università degli Studi di Napoli "Federico II"

Dipartimento di Scienze Fisiche

Doctorate School in Fundamental and Applied Physics

XXIII Cycle

Thesis

Novel tools for manipulating the photon orbital angular momentum and their application to classical and quantum optics

Supervisor:
Prof. Enrico Santamato

Candidate:
Sergei Slussarenko

Contents

Chapter 1

Introduction

1.1 Introduction

It is well known that light can carry mechanical properties. After the development of the Maxwell wave theory of light, Poynting showed that an electromagnetic wave carries defined linear momentum and energy flux through the plane, transverse to the propagation direction. From the classical point of view the value $\boldsymbol{H} \times \boldsymbol{E}$ is the linear momentum per unit volume and from the quantum point of view each photon has a definite projection of the linear momentum on the propagation direction, equal to $\hbar k$, where k is the wave vector and $\hbar$ is reduced Planck constant. Another degree of freedom – angular momentum is also well recognized by now. The first theoretical research, made by Poynting in 1909 [1] showed that a circularly polarized light beam carries a flux of angular momentum equal to $\frac{\lambda}{2\pi}u$, where u and λ are the average energy density and beam wavelength. Expanding this result to the quantum mechanical framework, a circularly polarized beam carries an angular momentum equal to $\hbar$ per photon with sign depending on the helicity of the polarization. The presence of the angular momentum was later confirmed and measured experimentally in a series of the experiments, performed by Beth [2, 3]. This "spin" angular momentum (SAM), however, is not the only one; photons can carry an another type, called orbital angular momentum (OAM), that may be present in a beam, which is produced by the transverse components of the linear momentum. The OAM was left outside general attention of scientists for a long time, remaining more a mathematical formality than an actual property of light to be exploited, since the contribution of these two types of angular momentum are indistinguishable in general.

A significant breakthrough happened when, in 1992, Allen et al. [4] showed that certain types of beams can carry a definite amount of OAM per photon in the similar way as a circularly polarized beam carry a definite value of SAM per photon. The main result of their work was that in the

paraxial approximation the contribution of spin and OAM can be clearly separated and that the beams having a phase factor of $\exp(i\ell\varphi)$, where φ is the transverse angular coordinate and ℓ is an integer number, carry a definite amount of OAM per photon, equal to $\ell\hbar$, which is conserved under propagation in homogeneous medium. This phase factor forms a continuous spiraling phase profile of the beam known as "optical vortex". The work opened a new, infinite dimension degree of freedom similar to the spin, but independent on the vectorial property of the light and associated to the phase structure of the beam. Since 1992 the attention towards OAM is increasing every year and the OAM-carrying beams have already found their place in many fields of classical and quantum optics. One of the most

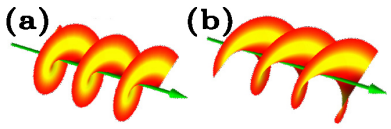

Figure 1.1: An example of the spiraling phase profile of the OAM carrying optical vortex. (a) the order of the vortex is equal to $\ell = 1$, (b) - the order of the vortex is equal to $\ell = 2$.

noted properties of OAM is how the OAM-carrying beam interact with the absorbing matter. Is is well known, that if a circularly polarized beam is absorbed by a particle a transfer of angular momentum happens that makes the particle rotate around its axis. The picture is different in the case of OAM where a micron-sized particle is rotated around the beam center instead. An illustration of this different mechanical coupling can be seen in Fig. 1.2, where the two types of optical traps are used to induce different kinds of rotation. The last rotation is impossible to achieve with polarized beam and the use of OAM has already found a wide number of applications in the optical tweezers where manipulation of small particles is needed.

OAM has also found its place in communication and computation, both classical and quantum. OAM eigenmodes, can be used as an alphabet for free-space communication [6]. The multidimensionality of the OAM space allows to expand the amount of the information, carried at the same time, to the theoretically infinite value, while the polarization space is limited to a single bit. A research, where more than one radio channel have been carried in the same electromagnetic wave of radio frequencies, was performed with excellent results, bringing the concept of OAM outside the optics field and carrying it closer to the every-day applications [7]. In the quantum optics field, classical bits are substituted by qubits, or higher-level systems, called qudits. Since the first proof of quantum nature of the OAM [8] this degree of freedom became one of the most promising candidates for the realization of the qudits with photons. This opens a wide road to many quantum information and quantum cryptography algorithms, that till now remained

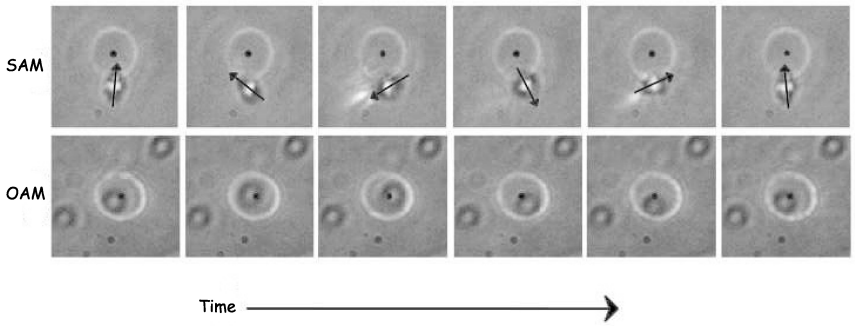

Figure 1.2: video frames of a movie, demonstrating the angular momentum transfer from the beam to a particle. In the line above the SAM is transferred, resulting in the rotation (indicated by an arrow) of the particle around its axis. In the lower line the OAM is transferred instead and the particle is rotated around the beam center, marked by a dark dot [5].

under study. Another promising development is the use of both OAM and SAM spaces, to encode information into a single photon, allowing to create multi-entangled and hybrid-entangled photon pair states, as well as single-photon entanglement, where two Hilbert spaces of the same particle are found in a non-separable state. OAM concept is also expanding in other fields of physics, like astronomy [9], diffraction-free optical microscopy [] or condensed matter physics [10, 11]. For a historical review of the development of this field the readers are referred to the book [12] where a collection of checkpoint articles is reported and for more recent developments of the study, reviews [13, 14, 15, 16, 17] may be also useful.

For now, the introduction of the OAM-based devices into the real world is mostly limited by difficulties of the creation of the beams that carry OAM. Some historical techniques,that require astigmatic lenses or complex interferometric setups are cumbersome, instable or difficult to mount and to align. The holographic technique, that uses computer generated holograms to control the phase profile of the beam is extremely versatile when the necessary hologram is generated by a spatial light modulator (SLM), however high costs of the latter confines this method to the research laboratories only.

In 2006 a novel liquid crystal device, called “q-plate”, was invented and realized in the laboratory of the University of Naples by Marrucci et al. [18, 19]. The q-plate is a birefringent waveplate whose optical axis direction is not uniform, but varying point per point. By transferring the topological charge that is formed by the anisotropy pattern, into the impinging beam the q-plate allows to generate OAM-carrying beams of the order defined by the pattern of the optical axis. The q-plate, despite its simplicity, offers new and highly efficient generation process that, in authors opinion, may change

significantly the possibilities of the OAM application. While the structure of the q-plate is not considerably more complex than a waveplate, q-plate can generate OAM-carrying beams with theoretically 100% efficiency with no specific requirements for the input light. The structure of the generated beams depends on the input polarization, allowing fast switching rates, never achieved with any known technique. The possibility to tune, or switch the q-plate generation efficiency with temperature or electric field broadens further the q-plate universality.

The objective of this thesis consisted mainly of the study of the q-plates, their manufacturing techniques, properties, q-plate-based devices, and their applications in classical and quantum optics. A number of novel results were obtained during this study, namely:

- the LC q-plates with unit topological charge were manufactured using the photoalignment technique for the first time;
- a photoalignment technique was used for manufacturing new LC q-plates with different topological charges, including fractional charges that were not realizable by previously used methods;
- electrical tunability of the q-plates was demonstrated for the first time, along with the analysis of the structure of the beam outgoing from the q-plate;
- the control of the generated beam OAM structure by polarization was demonstrated and a global phase was transferred from spin space to the OAM degree of freedom;
- a novel setup, based on the q-plate, for the high-alphabet optical communication was proposed and demonstrated;
- a proposal for a novel universal unitary gate, able to manipulate SAM and OAM degrees of freedom of the single photon at the same time was done;
- the entanglement of the SAM and OAM spaces of single photon and correlated photon pair was realized for the first time. The entanglement was tested by violation of the Bell's inequalities.

Apart the research of the q-plate and its applications, another device able to control the OAM, was studied, the Polarizing Sagnac interferometer (PSI). The PSI consists of a Sagnac interferometer with a tilted Dove prism inside. This device not only allowed to broaden the possibilities for q-plate application and was used for the analysis of the q-plate generating properties, but by itself is able to perform a wide class of operations on the OAM-carrying beams in both the SAM-OAM degrees of freedom, like sorting the different

orders of the OAM, realizing unitary quantum gates in the single photon spinorbit basis and generating specific entangled states.

The thesis is divided in five chapters according to the following structure:

Introduction. The current introduction chapter.

Angular momentum of light. A general introduction to the subject of the angular momentum of light and OAM-carrying beams together with the description of the most known devices used for OAM generation.

Q-plate. In this chapter the q-plate structure and functioning is introduced. After that the q-plate manufacturing techniques are described and the manufactured q-plates performance is studied.

Classical applications of the q-plate. In this chapter the applications of the q-plate in classical optics are discussed. The polarization control of the generation process and the communication device based on the q-plate are demonstrated. A more detailed description of the polarizing Sagnac interferometer is given in this chapter too.

Quantum applications of the q-plate. Quantum optics and information applications of the q-plate are shown in this chapter, namely the Universal Unitary Gate is proposed and the hybrid SAM-OAM entanglement is demonstrated.

The structure does not follow any chronological scheme and doesn't cover all the research done on the q-plate during last four years; mainly the works where the author was involved, directly related to this thesis were selected, with explicit citation of the published papers.

1.2 Notation

Here I will introduce the notation that will be mostly used in all the thesis, starting from the description of the polarization states of the photon, orbital angular momentum of the photons and some basic assumptions and labels.

Polarization states

In this thesis the Dirac notation will be used mostly. A bi-dimensional polarization space will be labeled by a ket-vector $|S\rangle_\pi$, where capital letter S will denote a certain polarization state and the suffix $_\pi$ labels the polarization space. Among the basic ones, the linear horizontal and vertical polarizations will be labeled as $|H\rangle_\pi$ and $|V\rangle_\pi$ respectively. Other important polarization states are the circular left $|L\rangle_\pi$ and the circular right$|R\rangle_\pi$ given by

$$
\begin{aligned}
|L\rangle_\pi &= \frac{1}{\sqrt{2}}(|H\rangle_\pi + i|V\rangle_\pi) \\
|R\rangle_\pi &= \frac{1}{\sqrt{2}}(|H\rangle_\pi - i|V\rangle_\pi),
\end{aligned} \tag{1.1}
$$

with the inverse relations

$$
\begin{aligned}
|H\rangle_\pi &= \frac{1}{\sqrt{2}}(|L\rangle_\pi + |R\rangle_\pi) \\
|V\rangle_\pi &= \frac{1}{i\sqrt{2}}(|L\rangle_\pi - |R\rangle_\pi).
\end{aligned} \tag{1.2}
$$

Circular polarization states are the eigenstates of the photon Spin Angular Momentum (SAM) operator $\hat{S}_z$

$$
\begin{aligned}
\hat{S}_z|L\rangle_\pi &= |L\rangle_\pi \\
\hat{S}_z|R\rangle_\pi &= -|R\rangle_\pi,
\end{aligned} \tag{1.3}
$$

with eigenvalues equal to ± 1 in units of $\hbar$, respectively.

Another linear polarization basis is made by the antidiagonal and diagonal polarization stated $|A\rangle_\pi$ and $|D\rangle_\pi$ that correspond to the polarization plane rotated through $\pm 45^\circ$ from the horizontal one:

$$
\begin{aligned}
|A\rangle_\pi &= \frac{1}{\sqrt{2}}(|H\rangle_\pi + |V\rangle_\pi) \\
|D\rangle_\pi &= \frac{1}{\sqrt{2}}(|H\rangle_\pi - |V\rangle_\pi).
\end{aligned} \tag{1.4}
$$

With these basis states, any elliptical polarization can be given as a superposition of any two orthogonal states ($|L\rangle_\pi$ and $|R\rangle_\pi$ or $|H\rangle_\pi$ and $|V\rangle_\pi$ or $|A\rangle_\pi$ and $|D\rangle_\pi$).

A common geometrical representation of the polarization state of a photon is the Poincaré sphere. It is a sphere of unit radius whose surface points are associated to a certain polarization. The poles of the sphere are usually mapped to basis states, for example $|L\rangle_\pi$ for the North pole and $|R\rangle_\pi$ for the South one. Then, any other point on the surface can be associated to a certain superposition of these two basis states. Linear polarizations in this case will lie on the equator of the sphere while all other elliptical polarization states will be mapped with the other points on the hemispheres. The Poincaré sphere is a graphical representation of the $SU(2)$ space and defines the polarization state up to a global phase only.

OAM space

Unlike the polarization space which is bi-dimensional, the OAM space has infinite dimensions. An eigenstate of this space will be denoted by the ket $|\ell\rangle_o$ where ℓ defines the OAM order and suffix $_o$ labels the OAM space. Selecting only the two states $|\ell\rangle_o$ and $|-\ell\rangle_o$ we can form a 2D subspace inside the total OAM space that will be equivalent to the SAM. The equal-weight superpositions of the basis states inside this subspace will be labeled analogously to the polarization state as

$$\begin{aligned} |h_\ell\rangle &= \frac{1}{\sqrt{2}}(|\ell\rangle_o + |-\ell\rangle_o) \\ |v_\ell\rangle &= \frac{1}{i\sqrt{2}}(|\ell\rangle_o - |-\ell\rangle_o) \end{aligned} \tag{1.5}$$

and

$$\begin{aligned} |a_\ell\rangle &= \frac{1}{\sqrt{2}}(|h_\ell\rangle + |v_\ell\rangle) \\ |d_\ell\rangle &= \frac{1}{\sqrt{2}}(|h_\ell\rangle - |v_\ell\rangle). \end{aligned} \tag{1.6}$$

In the most literature a beam carrying definite value of OAM is described by a Laguerre-Gaussian mode LG_{lp} where ℓ and p are azimuthal and radial quantum number respectively. This description is often inappropriate since since most of the devices that generate optical vortices (holograms, phase plates, q-plates, etc) usually do not produce pure LG_{lp} modes but a superposition of the modes with same ℓ number, but different p numbers [20, 21]. While the generated beam still carries a definite amount of OAM per photon which is invariant under free space propagation, the radial intensity structure is more complex than in a normal LG beam and changes under free propagation, in general. Whenever the radial profile has no relevance, I will denote these, more general OAM eigenfunctions as LG_ℓ. Whenever the OAM eigenstates $|\ell\rangle$ are associated to a LG_ℓ function then the equal weight superpositions $|h_\ell\rangle$, $|v_\ell\rangle$, $|a_\ell\rangle$ and $|d_\ell\rangle$ are given by Hermite-Gaussian functions that will be labeled as HG_ℓ, again without particular description to the radial profile of the beam. An equivalent of the SAM Poincaré sphere can also be introduced for the 2D subspaces of the OAM with fixed opposite ℓ [22, 23]. In this case the eigenstates $|\ell\rangle_o$ and $|-\ell\rangle_o$ are usually mapped to the North and south pole of the sphere and similarly to the previous case the linear HG_ℓ superpositions will be located at the equator of the sphere. All other points of the surface will correspond to an arbitrary superposition of $|\ell\rangle_o$ and $|-\ell\rangle_o$, giving a more complex structured beam.

Spinorbit space

A complete description of the photon state is formed by a tensor product of both SAM and OAM spaces, linear momentum space (which is also quan-

tized) and radial profile function:

$$|PSI\rangle = |S\rangle_\pi \otimes |\ell\rangle_o \otimes |k\rangle \otimes |u\rangle_\rho, \tag{1.7}$$

where ket $|k\rangle$ defines the direction of the propagation of the photon and $|u\rangle_\rho$ describes the radial profile of the beam. Selecting the first two we can obtain the spinorbit space that will be of particular attention in the thesis. A state $|S_\pi, \ell_o\rangle = |S\rangle_\pi |\ell\rangle_o$ gives the complete description of the SAM and OAM structure of the beam.

Since all the polarization kets will be labeled with uppercase letters, while the OAM kets – with lowercase letters, the suffixes $_\pi$ and $_o$ will often be omitted so to not overload the formalism.

Chapter 2

Angular momentum of light

2.1 Introduction

In the Maxwell's wave theory of light, all the calculations basically start from a system of four equations that describe the propagation of the electromagnetic waves. In the absence of the electric sources in vacuum these Maxwell equations are written as

$$\nabla \cdot \boldsymbol{E} = 0 \tag{2.1}$$

$$\nabla \cdot \boldsymbol{B} = 0 \tag{2.2}$$

$$\nabla \times \boldsymbol{E} = -\frac{\partial \boldsymbol{B}}{\partial t} \tag{2.3}$$

$$\nabla \times \boldsymbol{B} = \frac{1}{c^2}\frac{\partial \boldsymbol{E}}{\partial t} \tag{2.4}$$

where $\boldsymbol{E}$, $\boldsymbol{B}$ and c are the electric field vector, magnetic field vector and the speed of light in vacuum, respectively. Its worth mentioning the relation $c = \frac{1}{\sqrt{\epsilon_0 \mu_0}}$ that ties the speed of light c with the electric permittivity ϵ_0 and magnetic permeability μ_0. According to the wave theory, the linear $\boldsymbol{p}$ and angular $\boldsymbol{j}$ momentum densities are defined as

$$\begin{aligned} \boldsymbol{p} &= \epsilon_0 \boldsymbol{E} \times \boldsymbol{B} \\ \boldsymbol{j} &= \epsilon_0 \boldsymbol{r} \times (\boldsymbol{E} \times \boldsymbol{B}). \end{aligned} \tag{2.5}$$

The total linear and angular momentum values are obtained by integrating $\boldsymbol{p}$ and $\boldsymbol{j}$ over the volume. In the case of the monochromatic waves of frequency ω

$$\boldsymbol{E} = (\boldsymbol{E}(\boldsymbol{r})e^{i\omega t} + \boldsymbol{E}^*(\boldsymbol{r})e^{-i\omega t})/2 \tag{2.6}$$

$$\boldsymbol{B} = (\boldsymbol{B}(\boldsymbol{r})e^{i\omega t} + \boldsymbol{B}^*(\boldsymbol{r})e^{-i\omega t})/2 \tag{2.7}$$

the magnetic field $\boldsymbol{B}$ can be expressed as a function of the electric field

$$i\omega \boldsymbol{B} = \nabla \times \boldsymbol{E}. \tag{2.8}$$

Substituting Eq. (2.8) into (2.5) and integrating over the volume $\int d\boldsymbol{r}$ we can get the total linear

$$\boldsymbol{P} = \frac{\epsilon_0}{2i\omega} \int d\boldsymbol{r} \sum_{j=x,y,z} E_j^* \nabla E_j \tag{2.9}$$

and angular

$$\boldsymbol{J} = \frac{\epsilon_0}{2i\omega} \int d\boldsymbol{r} \sum_{j=x,y,z} E_j^* (\boldsymbol{r} \times \nabla) E_j + \frac{\epsilon_0}{2i\omega} \int d\boldsymbol{r} \boldsymbol{E}^* \times \boldsymbol{E} \tag{2.10}$$

momenta. The form of (2.10) suggests a separation of total angular momentum into two terms, one being independent from the coordinate $\boldsymbol{r}$ and other, being an explicit function of the coordinates. The first one, is usually called "spin" angular momentum and the second one, coordinate-dependent, is interpreted as "orbital" angular momentum. Such superficial subdivision is not always correct (since OAM can also be an intrinsic property of the beam) and under deeper investigation in the general case a number of significant problems arise. The question of the OAM and SAM separation for an arbitrary wave is still under theoretical discussion and will not be touched in this thesis. In the paraxial approximation, however, this approach can be developed without any loss of validity.

2.2 Wave equation and paraxial approximation

To describe the propagation of the light wave, the system of equations (2.1) the electric and magnetic fields in vacuum and in the Lorentz gauge are usually expressed through the vector potential $\boldsymbol{A}$ and scalar potential ϕ as

$$\boldsymbol{B} = \nabla \times \boldsymbol{A} \tag{2.11}$$

$$\boldsymbol{E} = -\nabla\phi - \frac{\partial \boldsymbol{A}}{\partial t}. \tag{2.12}$$

A straightforward calculation shows that the vector potential $\boldsymbol{A}$ obeys the wave equation

$$\left(\nabla^2 - \frac{1}{c^2}\frac{\partial^2}{\partial t^2}\right)\boldsymbol{A} = 0. \tag{2.13}$$

Separating the time variable as $\boldsymbol{A}(x,y,z,t) = \boldsymbol{A}(x,y,z)e^{i\omega t}$ we get the Helmholtz equation of the vector potential

$$\nabla^2 \boldsymbol{A} + k^2 \boldsymbol{A} = 0, \tag{2.14}$$

where $k^2 = \omega^2/c^2$.

The paraxial approximation consists in the assumption that the transverse dimensions of the beam are much smaller than the typical longitudinal

sizes. In this framework we can search for a solution of Eq. 2.14 in the form of a wave, propagating along the z axis:

$$\boldsymbol{A} = \boldsymbol{x}u(x, y, z)\exp(-ikz). \tag{2.15}$$

The wave is assumed to be a linearly polarized, for simplicity and $\boldsymbol{x}$ is the unit vector in the direction of the x axis, defining the polarization plane of the wave. Substituting (2.15) in into the Helmholtz equation we get the following form

$$\nabla^2 u - 2ik\frac{\partial u}{\partial z} = 0. \tag{2.16}$$

Since the laser beams represent one of the best physical realization of the paraxial beams it is convenient to pass to the dimensionless variables, using typical Gaussian beam parameters as the normalization values. Such parameters are the beam waist ω_0 and the diffraction length $l = k\omega^2$. Redefining the variables as $x = X\omega_0$, $y = Y\omega_0$ and $z = Zl$ we get

$$\frac{\partial^2 u}{\partial X^2} + \frac{\partial^2 u}{\partial Y^2} - 2i\frac{\partial u}{\partial Z} + \frac{{\omega_0}^2}{l^2}\frac{\partial^2 u}{\partial Z^2} = 0. \tag{2.17}$$

The relation ω_0/l is considered small in the paraxial approximation, allowing us to neglect the last term, containing $\frac{\partial^2 u}{\partial Z^2}$. The paraxial wave equation (PWE) is then given by

$$\frac{\partial^2 u}{\partial x^2} + \frac{\partial^2 u}{\partial y^2} - 2ik\frac{\partial u}{\partial z} = 0. \tag{2.18}$$

Before passing to the specific solutions of the paraxial wave equation let's estimate first what conditions must be applied to the solution of the form (2.15) so they can transport a definite amount of OAM per photon, as it was done by [4]. The electric and magnetic fields, expressed through the vector potential will be

$$\boldsymbol{E} = -i\omega\left[\boldsymbol{A} + \frac{1}{\omega^2\epsilon_0\mu_0}\nabla(\nabla\cdot\boldsymbol{A})\right] = \tag{2.19}$$
$$-i\omega\left[\left(u + \frac{c^2}{\omega^2}\frac{\partial^2 u}{\partial x^2}\right)\boldsymbol{x} + \frac{c^2}{\omega^2}\frac{\partial^2 u}{\partial x\partial y}\boldsymbol{y} + \frac{c^2}{\omega^2}\left(\frac{\partial^2 u}{\partial x\partial z} + ik\frac{\partial u}{\partial x}\right)\boldsymbol{z}\right]e^{-ikz}$$

$$\boldsymbol{B} = \nabla\times\boldsymbol{A} = ik\left[\left(u + \frac{1}{ik}\frac{\partial u}{\partial z}\right)\boldsymbol{y} + \frac{i}{k}\frac{\partial u}{\partial x}\boldsymbol{y}\right]e^{-ikz} \tag{2.20}$$

Defining the previously used small parameter ω_0/l as s and expanding Eqs. (2.19) and (2.20) in dimensionless variables we get

$$\boldsymbol{E} = -i\omega\left[\left(u + s^2\frac{\partial^2 u}{\partial X^2}\right)\boldsymbol{x} + s^2\frac{\partial^2 u}{\partial X\partial Y}\boldsymbol{y} + \left(s^3\frac{\partial^2 u}{\partial X\partial Z} + s\frac{\partial u}{\partial X}\right)\boldsymbol{z}\right]e^{-ikz} \tag{2.21}$$

$$\boldsymbol{B} = ik\left[\left(u - is^2\frac{\partial u}{\partial Z}\right)\boldsymbol{y} + is\frac{\partial u}{\partial Y}\boldsymbol{z}\right]e^{-ikz} \tag{2.22}$$

If we neglect the terms of order higher than first, but conserve the $\partial u/\partial z$ term in $\boldsymbol{B}$, we can get a simple expression for the linear momentum density

$$\boldsymbol{p} = \Re(\epsilon_0\boldsymbol{E}\times\boldsymbol{B}) = \frac{1}{2}i\omega\epsilon_0(u^*\nabla u - u\nabla u^*) + \omega k\epsilon_0|u|^2\boldsymbol{z} \tag{2.23}$$

As we can see, the left part of the equation separates into two terms, the transverse component of the linear momentum p_φ and the longitudinal one p_z. To get the expression of the angular momentum it is convenient to pass to the cylindrical coordinates (ρ, φ, z) first and separate the angular dependence in the following form

$$u(\rho, \varphi, z) = u(\rho, z)e^{i\ell\varphi}, \tag{2.24}$$

since the j_z component of the angular momentum will depend on the transverse part of the linear momentum p_φ. Substituting (2.24) into Eq. (2.23) we get the form of the p_φ as

$$p_\varphi = \frac{1}{\rho}\omega\epsilon_0\ell|u|^2 \tag{2.25}$$

and j_z as

$$j_z = \omega\epsilon_0\ell|u|^2. \tag{2.26}$$

From the ratio between j_z and p_z

$$\frac{j_z}{p_z} = \frac{\ell\lambda}{2\pi} \tag{2.27}$$

and ratio between j_z and energy density $c\boldsymbol{p}$

$$\frac{j_z}{w} = \frac{\ell}{\omega} \tag{2.28}$$

we get the result similar to the one, found by Poynting for the angular momentum, transported by a circularly polarized beam with the difference that ℓ values are not limited to ± 1, as in the case of the spin. Moreover, since our relation describes a linearly polarized beam, no spin component of the angular momentum is present and all the contribution is due to the orbital angular momentum of light. To get the description of total angular momentum, carried by a paraxial beam we must consider the light with arbitrary elliptic polarization

$$\boldsymbol{A} = (\alpha\boldsymbol{x} + \beta\boldsymbol{y})u(\rho, z)e^{i\ell\varphi}e^{-ikz} \tag{2.29}$$

with complex coefficients α and β related as $|\alpha|^2 + |\beta|^2 = 1$. Repeating all the calculations, that were done for the linearly polarized light, we get linear momentum density as

$$\boldsymbol{p} = \frac{1}{2} i\omega\epsilon_0 (u^* \nabla u - u \nabla u^*) + \omega k \epsilon_0 |u|^2 \boldsymbol{z} + \\ + i\omega(\alpha\beta^* - \alpha^*\beta) \left(\frac{\partial}{\partial y}\boldsymbol{x} - \frac{\partial}{\partial x}\boldsymbol{y} \right) |u|^2. \tag{2.30}$$

The new term is polarization dependent and the factor $(\alpha\beta^* - \alpha^*\beta)$ is related to the phase shift of two, perpendicularly polarized, components of the beam, or in other words – to the Stokes parameter σ_z that describes the projection of the spin along the propagation direction z. We can now recover the total angular momentum density along the propagation direction j_z obtaining

$$j_z = \omega\epsilon_0 \ell |u|^2 - \frac{\epsilon_0}{2} \omega\rho\sigma_z \frac{\partial |u|^2}{\partial \rho}. \tag{2.31}$$

Evaluating the ratio between j_z and energy density again we get

$$\frac{j_z}{w} = \frac{\ell}{\omega} - \frac{\sigma_z \rho}{2\omega|u|^2} \frac{\partial |u|^2}{\partial \rho}. \tag{2.32}$$

The relation of the total angular momentum along the propagation direction and total energy of the beam that is obtained by integrating the j_z and w over the volume will give the following elegant, yet expected, result

$$\frac{J_z}{W} = \frac{\ell + \sigma_z}{\omega}. \tag{2.33}$$

In the absence of ℓ component this result again reduces to the Poynting calculations [1] for the circularly polarized light. The additional term is, however independent on the polarization of the beam and is in fact OAM.

There are many solutions of the paraxial wave equation, fitting the conditions described above, that can carry OAM, the most well known being Laguerre-Gaussian modes $LG_{\ell p}$. These modes were also analyzed in the seminal work of Allen and coworkers, together with the introduction of the idea of the OAM in paraxial beams and till now they are the most widespread description of the beams that carry orbital angular momentum.

2.3 Laguerre-Gaussian modes

The $LG_{\ell p}$ are the complete and orthogonal set of solutions of the paraxial wave equation (2.18). Their analytical form in the cylindrical coordinates is given by

$$u_{\ell,p} = \frac{C}{(1 + z^2/{z_R}^2)^{1/2}} \left[\frac{\rho\sqrt{2}}{\omega(z)} \right] L_p^\ell \left(\frac{2\rho^2}{\omega^2(z)} \right) \exp\left(\frac{-\rho^2}{\omega^2 z} \right) \\ \exp\left(\frac{-ik\rho^2 z}{2(z^2 + z_R^2)} \right) \exp\left(i(2p + \ell + 1) \tan^{-1} \frac{z}{z_R} \right) \exp(i\ell\varphi) \tag{2.34}$$

where the parameters are normalization constant C, Rayleigh range z_R, $\exp\left(i(2p+\ell+1)\tan^{-1}\frac{z}{z_R}\right)$ is the Guoy phase shift, beam radius $\omega(z)$ and LG_p^ℓ are the Laguerre associated polynomials. The beam waist is at $z=0$. The radial index p defines the number of the $p+1$ radial nodes and the azimuthal index ℓ defined the $2\pi\ell$ variation of the phase along the closed loop around the center of the beam in the transverse plane. Such variation is due to the $\exp(i\ell\varphi)$ factor and is also the source of the so called phase singularity at the center of the beam. This phase singularity arises at the points where the field is undefined and thus the amplitude of the beam must take zero value. The 3D helical structure of the phase front, together with the "doughnut" intensity of a $LG_{1,0}$ beam are shown in Fig. 2.1. An example of the cross section of the beam phase structure at fixed z and their radial profiles are shown in the Figs. 2.2 and 2.3

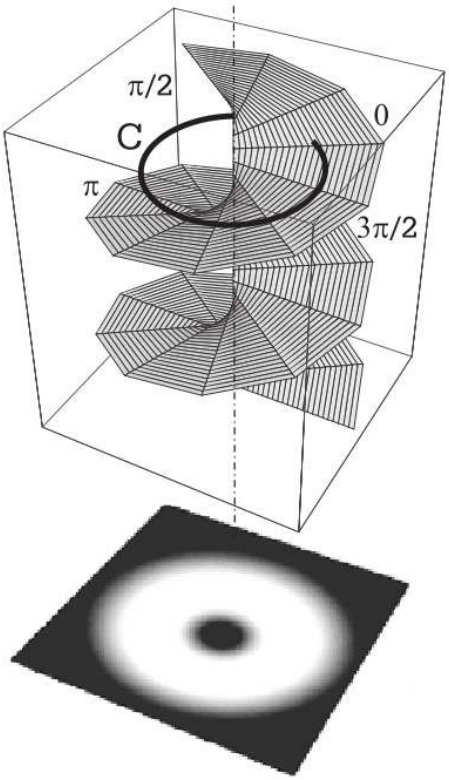

Figure 2.1: The phase structure and the beam intensity of the $LG_{1,0}$ mode with $\ell=1$ and $p=0$ [8].

Substituting the analytical form of the Laguerre-Gaussian modes into Eqs. (2.23) will give us the following expression for the linear momentum

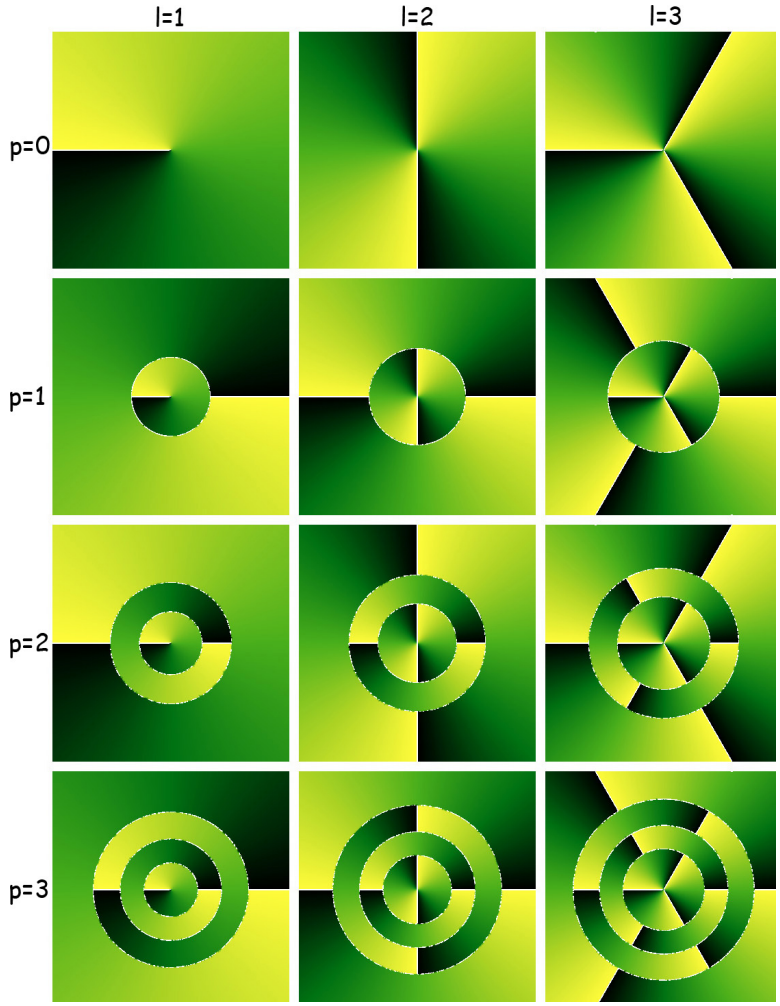

Figure 2.2: Examples of the phase structure of the $LG_{\ell,p}$ modes for the first three values of ℓ and p quantum number. The phase is increased from 0 to 2π with the color change from black to yellow respectively.

density of the $LG_{\ell,p}$ mode of linearly polarized light [4]

$$\boldsymbol{p} = \frac{1}{c}\left(\frac{\rho z}{(z^2+z_R^2)}|u|^2\boldsymbol{\rho} + \frac{\ell}{k\rho}|u|^2\boldsymbol{\varphi} + |u|^2\boldsymbol{z}\right) \tag{2.35}$$

The term along the $\boldsymbol{\varphi}$ unit-vector gives rise to the orbital angular momentum, while the $\boldsymbol{\rho}$ and $\boldsymbol{z}$ terms describe the beam expansion and the linear momentum density along the propagation direction. Calculating the angular momentum density $\boldsymbol{j} = \epsilon_0\boldsymbol{\rho} \times \langle \boldsymbol{E} \times \boldsymbol{B}\rangle$ yields

$$\boldsymbol{j} = -\frac{\ell}{\omega}\frac{z}{r}|u|^2\boldsymbol{\rho} + \frac{r}{c}\left(\frac{z^2}{(z^2+z_R^2)} - 1\right)|u|^2\boldsymbol{\varphi} + \frac{\ell}{\omega}|u|^2\boldsymbol{z}. \tag{2.36}$$

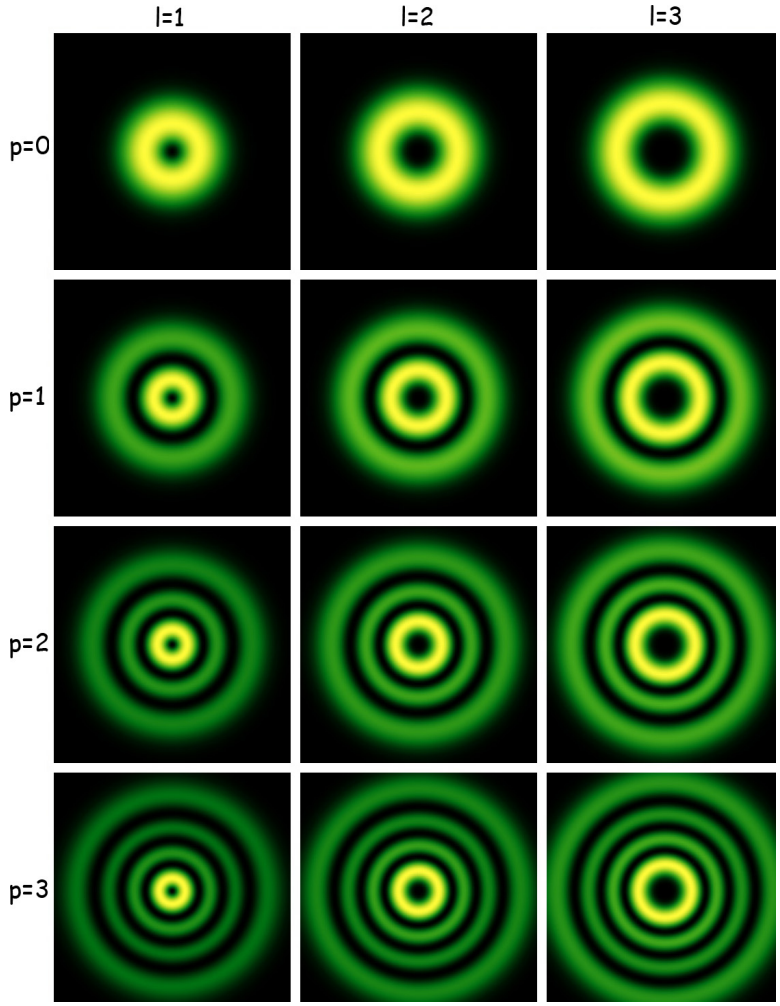

Figure 2.3: Examples of the normalized intensity profiles of the $LG_{\ell,p}$ modes for the first three values of ℓ and p quantum number. The intensity increases from 0 to 1 with the color change from black to yellow respectively.

The $\boldsymbol{\rho}$ and $\boldsymbol{\varphi}$ terms are axially symmetric, leaving only the contribution along the propagation direction into the total OAM, after the integration over the volume.

A well-known relation between Laguerre and Hermite polynomials allows us to express the $LG_{\ell,p}$ modes in terms of another complete family of PWE solutions in cartesian coordinates – Hermite-Gaussian modes $HG_{m,n}$

$$u^{HG}_{m,n} = C^{HG}_{m,n}(1/\omega)\exp\left(-ik\frac{x^2+y^2}{2R}\right)\exp\left(-\frac{x^2+y^2}{\omega^2}\right)$$
$$\exp\left(-i(n+m+1)\psi\right)H_m(x\sqrt{2}/\omega)H_n(y\sqrt{2}/\omega). \qquad (2.37)$$

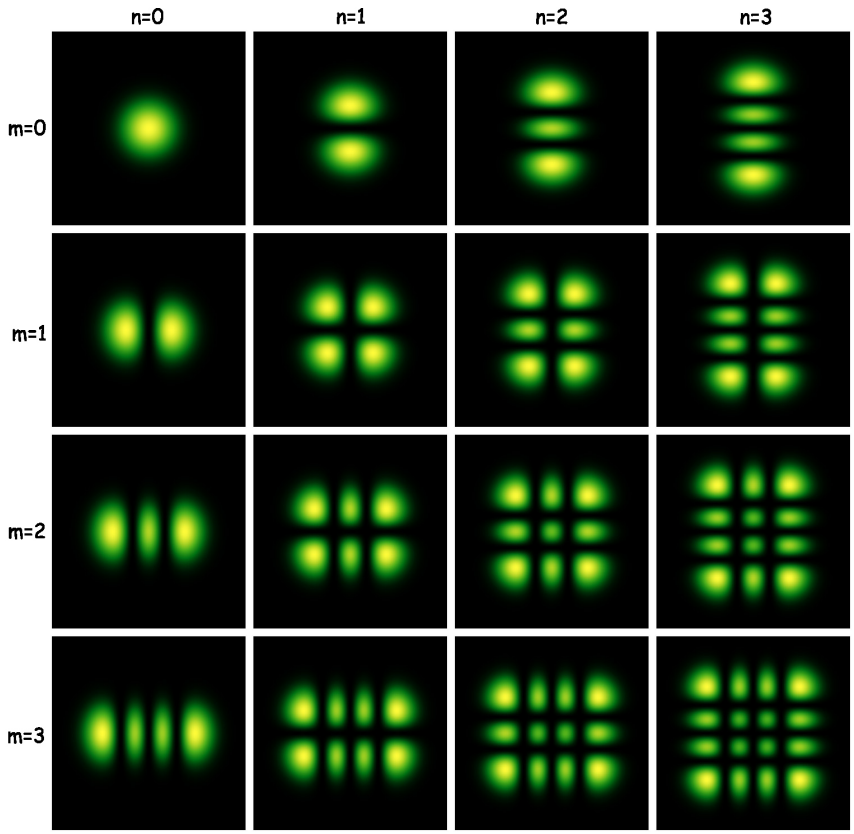

Figure 2.4: Examples of the normalized intensity profiles of the $HG_{m,n}$ modes for the first four values of m and n quantum number. The intensity increases from 0 to 1 with the color change from black to yellow respectively.

Rewriting them in the cylindrical coordinates yields

$$u^{LG}_{m,n} = C^{LG}_{m,n}(1/\omega)\exp\left(-ik\frac{\rho^2}{2R}\right)\exp\left(-\frac{\rho^2}{\omega^2}\right)\exp\left(-i(n+m+1)\psi\right)$$
$$\exp\left(-i(m-n)\varphi\right)(-1)^{min(m,n)}(\rho\sqrt{2}/\omega)L^{|m-n|}_{min(m,n)}(2\rho^2/\omega^2), \quad (2.38)$$

where the previously used indexes ℓ and p are now equal to $\ell = n - m$ and $p = min(m, n)$. An $LG_{\ell,p}$ mode can be expressed as a sum of finite number of the corresponding $HG_{m,n}$ modes according to the following relation

$$u^{LG}_{m,n} = \sum_{k=0}^{N} i^k b(m,n,k) u^{HG}_{N-k,k} \quad (2.39)$$

where $N = m + n$ is the mode order and

$$b(m,n,k) = \left(\frac{(N-k)!k!}{2^N n!m!}\right)^{\frac{1}{2}} \frac{1}{k!}\frac{d^k}{dt^k}[(1-t)^n(1+t)^m]|_{t=0}. \quad (2.40)$$

The i^k factor in (2.39) implies that there is a $\pi/2$ phase shift between every consecutive summand. A similar relation can be written for the $HG_{m,n}$ modes, rotated through 45° around the beam axis:

$$u^{HG}_{m,n}((x+y)/2,(x-y)/2,z) = \sum_{k=0}^{N} b(m,n,k)u^{HG}_{N-k,k}(x,y,z) \tag{2.41}$$

with the i^k factor absent and the coefficients $b(m,n,k)$ defined as in (2.40).

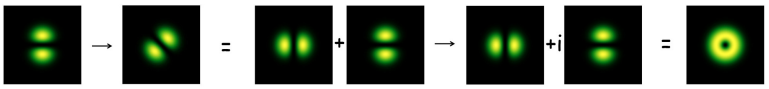

Figure 2.5: An example of the $HG_{0,1} \to LG_{1,0}$ transformation.

Given these relations, a following scheme may work as an example of a HG→LG transformation: a $HG_{0,1}(x,y,z)$ mode is rotated through 45° becoming a $HG_{0,1}((x+y)/2,(x-y)/2,z)$ mode, that in turn can be expressed as a sum of two modes

$$HG_{0,1}(\frac{x+y}{2},\frac{x-y}{2},z) = (HG_{1,0}(x,y,z) + HG_{0,1}(x,y,z))/\sqrt{2}. \tag{2.42}$$

After that, by introducing a phase shift of $\pi/2$ this sum can be transformed into a $LG_{1,0}$ mode, as illustrated in Fig. 2.5. Such technique was one of the first, used for the OAM-carrying beams generation, when a rectangular cavity was used to generate a HG laser beam and a set of cylindrical lenses was used to introduce the necessary phase shift between the separate components of the superposition (2.42), by acting separately on the Guoy phase of each component. Having a significant historical importance, this method is rarely used nowadays, due to its complexity and poor versatility.

While the $LG_{\ell,p}$ modes represent an elegant and simple illustration of the PWE solutions that carry a definite amount of OAM per photon, the real, widely used generation methods are unable to create a pure Laguerre-Gaussian mode. The actual beams, still possessing the desired $\exp(i\ell\varphi)$ phase factor, have a much complex radial intensity structure. The question of the beam intensity profile is usually neglected due to its complexity. Both phase holograms and spiral phase plates, that act only on the phase structure, in fact, produce not the pure $LG_{\ell,p}$ mode but an infinite superposition of the Laguerre-Gaussian modes with fixed ℓ, but varying p number. A more detailed study led to a discovery of a novel family of the PWE solutions, called Hypergeometric-Gaussian modes [20, 21].

2.4 OAM generation methods

A number of techniques and setups, that may be used to create beams that carry orbital angular momentum were proposed during last two decades, and some of them are now extensively used in the laboratories. In this section I will overview two important OAM generation methods, namely the holographic technique and spiral phase plate. The first one is the most versatile and widespread way to manipulate and create any wanted phase profile structure and the second is a fixed optical component, specially designed for creation of optical vortices of the given order.

A hologram is in general a picture of the interference of the certain beam (called "image") with the reference wave. Once registered, if we illuminate afterwards the hologram with the reference beam, it is possible to recover the phase and intensity structure of the image beam. If the interference picture, however is calculated analytically, or numerically, there is no need of actual image beam to exist. Such calculated holograms are called Computer-Generated Holograms (CGH). The calculated hologram can be registered on a special sensitive material (like photographic film) or a computer-controlled device, the Spatial Light Modulator (SLM).

The main hologram parameter is its efficiency, i.e. the ratio between the intensity of the requested output state and the total impinging beam intensity. Holograms can be of two types: amplitude and phase hologram. The first one is created by modulating the transparency of the medium, so the image beam is reconstructed when the hologram absorbs the light of the reference beam in one zones and makes it pass in others. The second one has uniform transparency, but the interference pattern is recorded into the optical retardation of the medium. After passing such structure, the beam recovers the previously recorded phase structure. The amplitude holograms are easier constructed, but have a limited efficiency, compared with the phase ones. Both types can be realized by a spatial light modulator. SLM is essentially a small pixellized screen with the transparency, or optical retardation of every pixel controlled by a PC. Comparing to the standard holograms that can be usually written only once, the SLM allows relatively fast switching (up to kHz) of the holograms. The main disadvantage of such devices, is however their high cost, fragility and pixellization, that limits the efficiency of the generated holograms much below the theoretical estimations.

An idea of the holographic generation of the optical vortices was proposed in 1990 [24], even before the discovery that the beams with the spiraling phase profile carry OAM. The hologram used to generate such beams was made by simulating the interference between a tilted plane wave $u_p = u_0 e^{i(k_x x + k_z z)}$ and an optical vortex $u_\ell = u_0 e^{i(k_z z + \ell\varphi)}$ of the same amplitude at the $z = 0$ plane and angle $\theta = \arcsin \frac{k_x}{k}$. The interference will be given then by

$$I = 2|u_0|^2(1 + \cos(k_x x - \ell\varphi)). \tag{2.43}$$

In the case of the two plane waves the pattern will be a normal diffractive grating with the sequence of the black and white lines of equal width and distance between them. In the case of the interference with the helical beam, a splitting of the lines occurs where the phase singularity is situated, as shown in Fig. 2.6. The ℓ value can be recovered from difference between the number of the lines above the singularity and the one below, giving, for example, a splitting of the one line into three in the case of $\ell = 2$. Such holograms were called "fork"-holograms (or "pitchfork"-) for their fork-like pattern. If a plane wave is incident on such a hologram (taking an amplitude

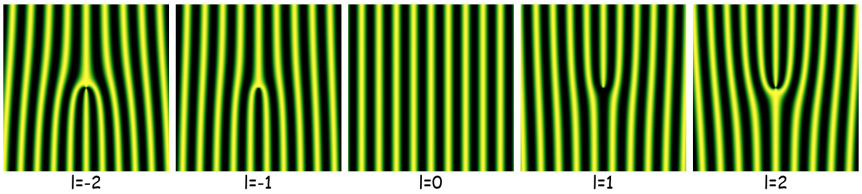

Figure 2.6: Interference patterns of the tilted plane wave and a helical beam of various order.

hologram for simplicity), the transmitted wave state will be given by

$$u_t = T(x, y)u_0, \tag{2.44}$$

with the hologram transmission function T, equal to

$$T(x, y) = \frac{1}{2}(1 + \cos(k_x x - \ell\varphi)). \tag{2.45}$$

Expanding Eq. 2.44 will give us the following sum:

$$u_t = \frac{u_0}{2}\left(1 + \frac{1}{2}e^{i(k_x x - \ell\varphi)} + \frac{1}{2}e^{-i(k_x x - \ell\varphi)}\right). \tag{2.46}$$

As we can see, apart from the fraction of the beam that passes unchanged, in the first diffractive order the wave has acquired a helical phase profile of order ℓ for the positive order and $-\ell$ for the negative one. In simple words, such hologram leaves the beam untouched in the zeroth order, adds the $\exp(i\ell\varphi)$ factor in the first order and adds the $\exp(-i\ell\varphi)$ factor in the negative first order. Same is applied, when the impinging beam is not a plane wave, but an optical vortex. This can be used for the OAM detection purposes, when for example a beam with OAM order $\ell = -1$ is sent through the hologram with $\ell = 1$. In this case the beam in the first order will have not a doughnut profile, but a bell-shaped one with no OAM, allowing to filter it with an optical fiber, placed where the singularity of the beam is expected to be.

Phase holograms do not absorb the light and the modulation is induced in the phase of the beam. The transmission function for the previous example will be given by

$$t(x,y) = e^{ia\frac{1}{2}(1+\cos(k_x x-\ell\varphi))} = e^{ia\frac{1}{2}} \sum_{n=-\infty}^{+\infty} i^n J_n(a) e^{in(k_x x-\ell\varphi)}, \tag{2.47}$$

where a is the phase depth of the hologram and J_n is the Bessel function of order n. Phase holograms usually give higher efficiency, due to the lack of absorbtion.

The sinusoidal (whose fringe shape is given by a cos or sin) amplitude hologram theoretically gives only the first positive and negative orders of diffraction (together with the zero order). The phase holograms spread the input power into several diffraction orders. There are other kinds of holograms with different shape of the fringes that provide other power distribution among diffraction orders. We will enumerate the four most noted ones:

1. Sinusoidal grating

$$g(x,y) = \frac{1}{2}[1+\cos(k_x x-\ell\varphi)] \tag{2.48}$$

2. Blazed grating

$$g(x,y) = \frac{1}{2\pi} Mod(k_x x-\ell\varphi, 2\pi) \tag{2.49}$$

3. Binary grating

$$g(x,y) = \frac{1}{2}[1+Sign(\cos(k_x x-\ell\varphi))] \tag{2.50}$$

4. Triangle grating

$$g(x,y) = \frac{1}{\pi} Sign(k_x x-\ell\varphi)[\pi - Mod(k_x x-\ell\varphi), 2\pi] \tag{2.51}$$

where $Mod(m,n)$ is the remainder of the division of m by n and $Sign(m)$ is the sign function $m/|m|$. The examples of these hologram types are shown in Fig. 2.7 and their efficiencies and generated order numbers are listed in the Table. 2.1.

Certain types of holograms, like blazed phase holograms, can give a very high nominal efficiencies, reaching 100% with only one diffraction order. In practice, however the real efficiency value is limited by the manufacturing and recording processes in the case of static holograms, or by the presence of pixels, in the case of the holograms generated by a SLM. Such imperfections may change number of orders generated and the intensity distribution between them. The typical hologram efficiencies thus rarely exceed 40%.

Figure 2.7: Four different types of the same $\ell = 1$ hologram. From left to right the fringes shape is given by a sinusoidal, blazed (saw-tooth), binary and triangular functions.

Table 2.1: Maximum nominal efficiencies calculated as the ratio of the intensity in the first diffraction order over the total input intensity for the different types of gratings and different types of holograms.

Grating type	Amplitude hologram		Phase hologram	
	Orders	Efficiency	Orders	Efficiency
Sinusoidal	zero and ±first	6.25%	all	33.85%
Blazed	all	2.53%	first	100%
Binary	odd	10.13%	odd	40.52%
Triangular	odd	4.10%	all	29.81%

The holographic technique allows to generate an arbitrary beam and is extremely versatile, allowing dynamic computer-guided switching. The main drawbacks are, however relatively poor efficiency, diffractive nature of the generating process and elevate costs of the spatial light modulators.

Another object, used to create beams with the helical phase profile is called Spiral Phase Plate (SPP) and it was developed in 1994, specially for the optical vortex generation [25]. The SPP is a solid, transparent, dielectric plate with one plane and one spiraling side, as shown in Fig. 2.8. Due to the varying thickness of this plate the impinging beam will gain an additional, coordinate-dependent phase shift. If the dimension of the step of the spiraling side is equal to d then the phase variation will be given by

$$\delta = \frac{(n_1 - n_2)d}{\lambda}\varphi, \tag{2.52}$$

where n_1 and n_2 are the refractive indices of the SPP and surrounding medium respectively. The condition, necessary to generate an optical vortex is that the total phase change around the center of the plate must be an integer multiple of 2π, meaning that the spiral step must be equal to

$$d = \frac{\ell\lambda}{(n_1 - n_2)}\varphi. \tag{2.53}$$

The manufacturing of a SPP requires a high level of mechanical precision

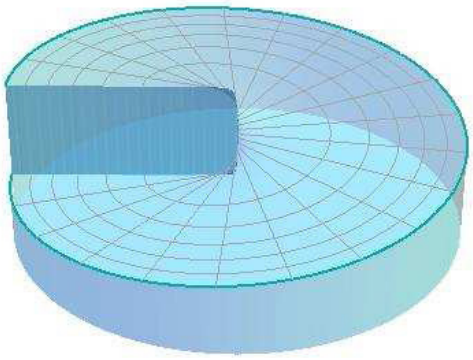

Figure 2.8: A spiral phase plate.

to realize the condition (2.53) and provide the correct shape of the spiraling side, with continuous and correct increase of the thickness of the SPP. The spiraling side of the SPP, however, is usually made by an approximation with the number of plane tilted sectors. Such approach is realized easier at the expense of the quality of the generated beam.

The spiral phase plate is much less universal, compared to the holograms, since it can generate only one fixed OAM order and it works only at the wavelength for which it was fabricated.

Chapter 3

Q-plate

3.1 Introduction

All the previously mentioned OAM generating techniques have a number of serious drawbacks and limitations. The interferometric setups and astigmatic lens converters are unstable and require particular input state that is not easy to generate, SSPs are difficult to manufacture, and holograms have poor generation efficiency. The most promising tool which is spatial light modulator, can be used to generate any phase structure of the beam and can be controlled by PC, however their high cost limits the adoption of SLM outside the laboratory. The pixel structure of the SLM working area also limits the generation efficiency much below the theoretical one (with a typical value of 40%). The working speed of an SLM is also limited by kHz in the best cases.

Recently, a novel device called "q-plate", able to manipulate the OAM was introduced by Marrucci et al. [18, 19]. The q-plate is essentially a birefringent plate, whose optical axis is continuously varying point per point in the transverse plane. Such inhomogeneous orientation of the optical axis induces an additional phase, that varies in the transverse plane, into the impinging beam. The q-plate belongs to a class of optical components that is called Pancharatnam-Berry optical elements (PBOE) and their action is based on the concept of geometrical phase introduced by S. Pancharatnam in 1956 [26] and later rediscovered by M.V. Berry in 1984 [27] with subsequent development and generalization. A simple description of the geometrical phase is as follows: if the state of a particle is adiabatically changed so that the final state is equal to the initial – an additional phase factor appears. Such phase factor depends only from the path on the projective-Hilbert space that describes the state change. In the case of the photon polarization, such path is a closed trajectory on the surface of the Poincaré sphere and the phase factor that appears is equal to half of the solid angle of the area, encompassed by the trajectory [28]. A typical demonstration of the

geometrical phase can be seen when a photon is made pass through a set of wave-plates that change its polarization state and the phase difference can be observed between the input and output states [1], or when a light beam is made pass through a single rotating wave plate, where an additional phase factor can be observer between same initial and final state of the light beam. In all these cases a uniformly polarized, in the transverse plane, beam undergoes a time-variant state change. During last decade, a different view on the geometrical phase was developed and demonstrated, where the polarization state manipulation is space-variant. In other words, the light beam undergoes a polarization change that is different in every point in the transverse plane [29]. As is was demonstrated both theoretically and experimentally, such polarization manipulation is accompanied by an additional space-variant phase change that is explained in terms of geometrical phases. Some of the devices, working on this principle were realized with the use of patterned sub-wavelength metallic gratings were carried out, namely diffraction gratings [30], helical mode generators [31], lenses [32] etc.

Let us see more in details how the light state is changed by the q-plate that is essentially a birefringent uniaxial wave plate with inhomogeneous orientation of the optical axis in the transverse plane. In the case of the angular dependence only, the local axis orientation α can be described by

$$\alpha(\varphi) = q\varphi + \alpha_0 \tag{3.1}$$

where φ is the azimuthal angle coordinate, q is the topological charge (from which the name "q-plate" appeared) and α_0 is a real value. The overall pattern of the optical axis distribution is defined by the topological charge, while the overall inclination of the axis is given by α_0. In the case of semi-integer q value the axis distribution will change smoothly and without disclinations in the axis orientation. Some of the patterns that correspond to the different topological charges are illustrated in Fig. 3.1.

The action on an impinging light beam can be easily described using the Jones matrices. The matrix, corresponding to the q-plate action in the linear polarization basis is given by

$$\hat{U}(q,\delta) = R(\alpha)\begin{pmatrix} e^{i\frac{\delta}{2}} & 0 \\ 0 & e^{-i\frac{\delta}{2}} \end{pmatrix} R(-\alpha) \tag{3.2}$$

where $R(\alpha)$ is the rotation matrix that corresponds to a rotation around angle α in the transverse plane. Straightforward calculations show that, taking in account Eq. (3.1), in the circular polarization basis, Eq. (3.2) can be reduced to

$$\hat{U}(q,\delta) = \cos\frac{\delta}{2}\begin{pmatrix} 1 & 0 \\ 0 & 1 \end{pmatrix} + i\sin\frac{\delta}{2}\begin{pmatrix} 0 & e^{i2q\varphi} \\ e^{-i2q\varphi} & 0 \end{pmatrix}. \tag{3.3}$$

[1] of course, after proper compensation of the dynamic, frequency-dependent phase change

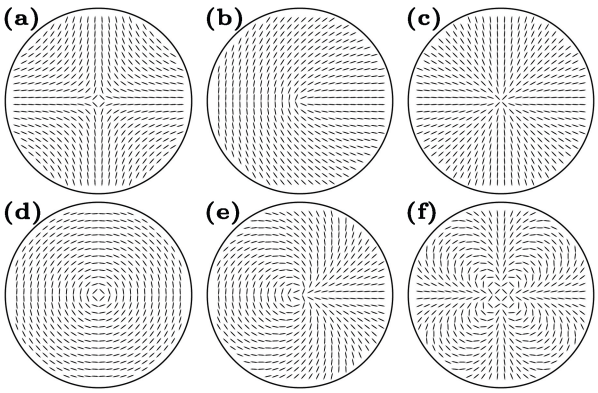

Figure 3.1: LC patterns that correspond to different topological charges: (a) – $q = -1$, (b) – $q = 0.5$, (c)-(d) – $q = 1$, (e) – $q = 1.5$, (f) – $q = 3$

As we can see, depending on the phase retardation, a portion of the impinging beam passes unchanged through the q-plate, while another has it's polarization helicity switched and gains an additional helical phase factor of $\exp(\pm i2q\varphi)$ that corresponds to the change $2q$ of the OAM order of the beam. Rewriting Eq. (3.3) in the Dirac notation the action of the q-plate on the circularly polarized beam with arbitrary OAM order ℓ is given by

$$\begin{aligned}\widehat{QP}|L,\ell\rangle &= \cos\frac{\delta}{2}|L,\ell\rangle + i\sin\frac{\delta}{2}|R,(\ell+2q)\rangle \\ \widehat{QP}|R,\ell\rangle &= \cos\frac{\delta}{2}|R,\ell\rangle + i\sin\frac{\delta}{2}|L,(\ell-2q)\rangle.\end{aligned} \tag{3.4}$$

This way, a portion of the circularly left polarized beam is transformed into the circularly right polarized beam with an increase of the OAM order of $2q$, while the circularly right polarized beam is converted into the left polarized with a decrement of the OAM order by the same $2q$. A particularly interesting case is the q-plate with $q = 1$. Such structure, being circularly symmetric, cannot change the total angular momentum of the light beam and, indeed, the variation of the OAM is equal to ± 2, while the SAM state is changed from ± 1 to the ∓ 1 giving the same amount of the angular momentum variation and leaving the total SAM+OAM unchanged. Such process was called **S**pin-**T**o-**O**AM **C**onversion (**STOC**)[33]. This is not applicable to the q-plates with topological charge that is different from $q = 1$, resulting into the transfer of angular momentum to the q-plate and not only SAM-OAM conversion onside the beam. However, for the sake of brevity the conversion process for all the q-plates will be indicated as STOC later on. The phase retardation δ of the q-plate can be changed externally, by varying the temperature of the LC cell [33], by applying electric field to the LC layer and other. When $\delta = \pi$, that is equivalent to the half-wave phase retardation, the q-plate performs complete state conversion leaving no pho-

tons unchanged. Such q-plate will be called "tuned" thereafter. A q-plate can generate OAM carrying beams starting from the normal gaussian laser mode. The generation efficiency can, in theory, reach 100% and is tunable to arbitrary value and for arbitrary input wavelength. The q-plate, being a thin LC cell is easy to align and manipulate and is highly transparent thus allowing to use more than one q-plate in cascade. Another significant advantage is that the output OAM state is polarization dependent, allowing fast switching of the output modes with rates much higher than the SLM can provide. This point will be discussed later in the chapter 4.1. While the general picture of the q-plate action can be described by Jones matrices, a detailed study of the light propagation inside the q-plate with precise description of the radial modes structure was done elsewhere [21]. In the following sections I will describe the manufacturing processes of different types of the q-plates and their characterization in terms of efficiency and tunability.

3.2 Q-plate fabrication

3.2.1 Rubbing

Patterned orientation of the optical axis is achievable with soft materials like liquid crystals, liquid crystal polymers, photosensitive polymers and other. Liquid crystal (LC) can be structured to have desired pattern by a surface induced alignment, when the topological charge is first imprinted into a thin substrate of polymer or similar surfactant inducing the alignment onto the LC. The surface anisotropy can be created by rubbing the aligning layer with velvet fabric [34]. The LC, when put in contact with the layer will then align along (or perpendicular, depending on the surfactant and LC type) the rubbing direction.

Rubbing was the original technique used in our laboratory for q-plates fabrication [18, 33]. Rubbing allows to create q-plates with unit topological charge (Fig. 3.1 (b)). The process is the following: two fused silica glasses, previously cleaned, were coated with a thin layer of DuPont PI2555 polyimide (a polymer of imide monomers) using spin-coater. Such polyimide (PI), when put in contact with the LC, creates planar (i.e. parallel to the surface) orientation of the molecules of LC. After the coating, glasses were soft-baked to vaporize the solvent and cured in the oven at 220°C for two hours. The polymerized coating was then circularly rubbed by a rotating velvet cloth so to induce a circular pattern on the coated surfaces. At the center of the rotation where no anisotropy is created, a defect is formed. After that, the glasses, separated by mylar spacers of $7\mu m$, were put together and a nematic LC (E7 or E63 from Merck) was injected between them. The glasses were precisely aligned so to have the two topological defects superimposed and the inner sides of the glasses parallel to each other.

During construction, the glasses parallelism was controlled constantly using reflections of He-Ne laser beam from the sample inner sides, and the LC alignment and singularities position was checked by a polarizing microscope with crossed polarizers. After the LC relaxation, the molecules were oriented along the rubbing directions so the surface pattern was induced into the LC. The glasses were glued by epoxy glue afterwards. Both azimuthal and radial transverse patterns that corresponds to the $q = 1$ topological charge are achievable by such technique. The second one (Fig. 3.1(c)) can be realized by choosing specific materials with which the LC will be oriented perpendicular to the rubbing directions. The polarizing microscope image of the center of the q-plate, made by the rubbing technique is shown in Fig. 3.2(a). The photo was taken with crossed polarizers and the dark arms correspond to the zones, where the alignment of the LC was parallel to one of the polarizers, so no light passes, since no change in polarization state was induced by the QP in those zones. Another variation of the rubbing method is to induce anisotropy only on one substrate,while providing degenerate planar [19] or homeotropic (perpendicular to the glass substrate) alignment of the LC by choosing proper surfactant and substrate treatment. These approaches simplify the alignment process of the glass substrates since there is no need of superimposing the two central defects. In the case of degenerate planar alignment, however, a disclination line is formed along the diameter [19].

3.2.2 Photoalignment

A more recent and promising technique of LC alignment is photoalignment. In this case the desired orientation of the LC is achieved by illuminating the material (bulk dye-doped LC or thin film surfactant) with linearly polarized light of appropriate wavelength, usually UV. The first studies of surface induced photoalignment were performed with dye-doped polymer and pure dye layers [35], photopolymers [36, 37], polyimides (PI) [38], and others. In all these cases the anisotropy is induced into the surface material by the polarized light that in turn reorients the adjacent LC molecules, usually perpendicular to the polarization direction. Even if the process is similar, the physical mechanisms involved may differ drastically. Comparing to the rubbing, the photoalignment, is a clean and non-contact technique, do not introduce surface defects or damage and electrostatic charges, allows to control the pretilt angle and the anchoring energy of the LC cells. The research area of photoalignment is vast and rapidly developing, so only few techniques of surface induced photoalignment that were used for the q-plate fabrication will be discussed. A more detailed description of different photoalignment methods and their applications in modern science and industry can be found in [39]. For the specific case of q-plate manufacturing, photoalignment has some additional advantages. Between them, the most important ones are:

- Aligning by the light beam allows to align two layers of the surfactant simultaneously. This way, the q-plate may be assembled before the pattern is induced. Such possibility simplifies a lot the procedure of alignment of the glass substrates, since there is no need of precise superimposing of the two central defects (that are automatically superimposed when created) and the substrate parallelism may be achieved and controlled by the standard techniques, used in the LC cell assembly.
- Dependence of the alignment from the light polarization widens the range of possible patterns that can be imprinted into the LC cell, allowing to induce any topological charge into the LC, while the circular rubbing allows to create only circularly symmetric patterns with charge $q = 1$ shown in Figs. 3.1 (c) and (d).

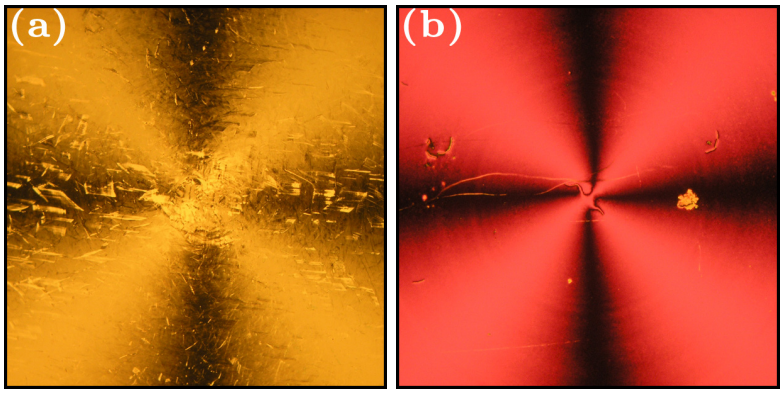

Figure 3.2: $q = 1$ q-plate polarizing microscope images with orthogonal polarizers. (a) – a QP made with rubbing technique, (b) – a QP made with UV photoalignment

3.2.3 Polyimide photoaligned q-plates

[40] The process involved in the photoalignment with the thin polyimide film as a surfactant is called photodegradation (or depolymerization). A coated and cured thin film of PI usually has it's polymer chains oriented randomly. Under exposure to linearly polarized UV light, the probability of absorbing of the photons by the PI is higher for the chains that have their absorbtion oscillators oriented parallel to the polarization plane, meaning that these chains are most likely to be destroyed by the incident illumination, while the others remain unbroken. This way, the direction of the unbroken chains, which is perpendicular to the incident polarization, will define the alignment of the LC. Since the photodegradation consists in destruction of the chemical bonds, an overexposure of the aligning surface will destroy

previously induced anisotropy [38, 41, 39]. Such irreversible photochemical processes make difficult to control the alignment process and layer purity, that can be contaminated by the products of the photodegradation. PI materials, however posses high thermal stability and are usually not sensitive to the visible region of the light.

The PI photoalignment was used by the author to create high quality q-plates with $q = 1$ topological charge. A New Wave "Tempest 20" Nd:YAG pulsed laser[2], operating at 355nm wavelength, 20Hz repetition rate and pulse FWHM of 4ns, was used as a polarized light source for this purpose. The vertically polarized laser beam illuminated a previously coated by PI from Nissan Chemicals and assembled sample through an angular mask, made from two razor blades, so to illuminate only one sector of around 20° of the sample. The sample, attached to a precision rotation mount (GM-1RA from Newport) was placed so to superimpose the rotation center of the support with the vertex of the angular mask and then rotated by an electric motor. After the exposure, the cell was filled with LC. The illuminated surfaces induced an alignment to the LC layer orienting the molecules perpendicular to the incident vertical polarization direction. The best results were obtained with the exposure time of 1h 20m and pulse energy of 35 mJ/cm^2. By changing the incident polarization it is possible to realize any $q = 1$ pattern with arbitrary value of α_0. A polarizing microscope picture of a QP made by this technique is shown in Fig. 3.2(b). The optical properties of these q-plates will be discussed in chapter 3.3.

Operating with the materials that are sensitive to UV light allows to create q-plates with very stable patterns that can be used with any wavelength of visible and infrared region of light. However such technique requires particular light sources and optical components (lenses, polarizers, etc.) made with SiO_2, or other UV-transparent material, that usually have higher cost as compared to the standard ones.

3.2.4 Azo-dye photoaligned q-plates [42]

I also manufactured q-plates with a different photoalignment technique, where a thin layer of azo-dye molecules was used as a surfactant. Azo-dyes are chemical compounds with general formula in form of $R - N = N - R'$, where R and R' are aryl functional groups. Under the illumination by the linearly polarized light, such azo-dye molecules reorient themselves perpendicular to the polarization direction. More detailed descriptions of the mechanisms involved can be found elsewhere [39].

The material used as a surfactant was sulphonic azo-dye SD1 from

[2] access to this laser and necessary equipment were kindly provided by Prof. Giancarlo Abbate and Dr. Vladimir Tkachenko from the laboratory of "Electro-Optical Devices Made with Liquid Crystals and Polymers", Dipartimento di Scienze Fisiche, Università degli Studi di Napoli "Federico II", Naples, ITALY

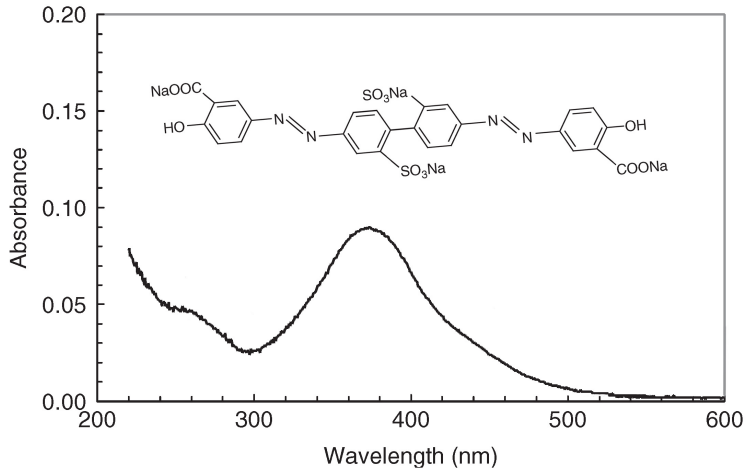

Figure 3.3: Absorbtion spectra before UV irradiation and the chemical structure of the sulfonic azo-dye SD1 [39], that was used as photoaligning surfactant for the q-plates with topological charges, different from $q = 1$.

Dainippon Ink and Chemicals. It's chemical structure and absorbtion spectra are shown in Fig. 3.3. Such material can be photoaligned not only with the UV light, but with the 400-450 nm blue-violet region of the visible radiation. A good source of such light is a blue high-power LED that can be bought commercially. The use of visible light photoalignment allows to exclude the use of high-cost polarizers and optical components that are necessary for the UV. Another feature of the SD1 is the so called optical rewritability, i.e. the possibility to rewrite previously induced alignment by another one. This is possible due to the particular mechanism of the photoalignment of this dye that doesn't involve any photochemical reactions, cis-trans isomerization, or photodegradation of the material and consists in pure rotation of the molecules [39]. The photoalignment that involves this mechanism provides the best anchoring energy, comparable with the PI rubbing and is less sensitive to the non-uniformity of the aligning radiation, since the overexposure will not destroy the alignment, but instead will increase the stability of the pattern.

The setup, used to manufacture the q-plates is similar to the one used for the fabrication of the UV photoaligned q-plates. The sample and polarizer, however were attached to the rotating mounts (GM-1RA from Newport) that were controlled by a PC software through two stepping motors. An additional SiO_2 cylinder (made of two hemicylinder lenses from Harrick Scientific Corporation) was placed after the angular mask so to eliminate the diffraction and focus the triangular spot onto the sample. An OmniCure "Series 1000" mercury lamp of 180mW/cm^2 light power was used as the collimated light source and all the components were put on an optical rail

to ensure the alignment of the rotation center of the sample with the vertex of the angular mask.

The glasses for the cell were spincoated with a 1% solution of SD1 in dimethylformamide (DMF) at 3000 rpm for 30 seconds and soft baked at 100°C for 5 min. The substrates were assembled together and $6\mu m$ dielectric spacers were used to define the cell gap. After the exposure, the cells were filled with MLC 6080 liquid crystal mixture from Merck.

With the precise control of the rotation steps of the two mounts it was possible to create q-plates with different topological charges. The topological charge induced is given by $q = 1 \pm \frac{\omega_p}{\omega_s}$, where ω_p and ω_s are the angular speeds of the polarizer and sample and $+$ and $-$ signs correspond to the opposite and same rotation direction of the two mounts, respectively. This way, for example, the $q = 1$ charge is realized by fixing the polarizer ($\omega_p = 0$) and the charge $q = 1/2$ is achieved if the sample is rotated twice faster than the polarizer, in the same direction. The parameter α_0 was controlled by the initial orientation of the polarizer. Using this setup, q-plates with charges -1, 0.5, 1, 1.5, 3, and others were fabricated. Some of the pictures of the samples, placed between crossed polarizers are shown in Fig. 3.4.

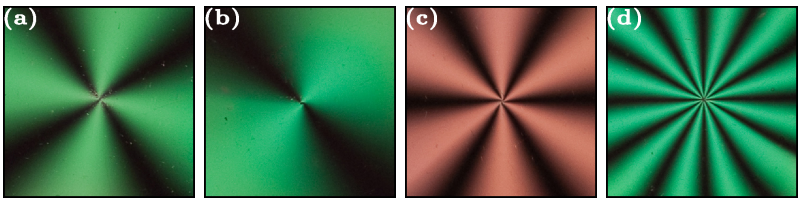

Figure 3.4: Photos of the q-plates with different topological charges placed between crossed polarizers: (a) – $q = -1$, (b) – $q = 0.5$, (c) – $q = 1.5$, (d) – $q = 3$

This work was performed by the author in the framework of joint collaboration between research groups of Prof. Enrico Santamato and Prof. Vladmir Chigrinov from Hong Kong University of Science and Technology, Kowloon, Hong Kong, at the facilities of the Center for Display Research in Hong Kong University.

Q-plates with use of liquid crystal polymers were realized elsewhere [43].

3.3 Q-plate electric field tunability [40, 42]

As it was previously shown in Eq. (3.4), the power fraction of the light that is converted by the q-plate depends on the phase retardation of the cell, and the maximum conversion, with theoretical efficiency of 100%, is achievable when the q-plate retardation is half-wave, i.e. $\delta = \pi$. Fabrication of the q-plates with defined and uniform phase retardation requires high precision

manufacturing methods and precise control of the birefringent layer, if the q-plate is made by polymer material, such as liquid crystal polymer [43]. In the case of LC, however, the optical retardation can be tuned externally, changing the temperature of the q-plate, or applying an electric field to the LC layer. The ability to control the STOC process by temperature was already shown and the efficiencies of more than 95% were achievable with temperature-tuned q-plates [33]. In this section I will discuss the electrical tunability of the q-plates.

It is well known, that LC molecules reorient themselves if an electric field is applied. Such effect is called Frederiks transition [44]. Due to the anisotropy of dielectric and diamagnetic permittivity of the LC, if an external electric or magnetic field is applied to the bulk LC a certain molecules orientation will correspond to the minimum of the free energy. In the case of positive birefringence, the director of the LC is preferably oriented along the field and in the case of negative birefringence the molecules are likely to stay perpendicular. When the LC orientation do not correspond to the minimum free energy condition, a strong enough external field (so to overcome the elasticity of the LC) may induce reorientation of the molecules. The voltage, required for reorientation and reorientation speed depends on the properties of the LC and surfactant material, anchoring energy, alignment and other parameters. If the LC film has planar alignment at both borders, then the Frederiks transition will have a threshold value of the applied field, below which no changes in the cell will occur. Threshold value has a complex dependence on the surfactant and LC type, method used to induce alignment, anchoring energy and other. The threshold value vanishes when at least one of the borders has vertical (homeotropic) alignment of the LC. To prepare an electrically tunable LC cell, glass substrates with conductive and transparent coating are used. The most known material with such properties is indium tin oxide (ITO). ITO is a solid solution of In_2O_3 (90%) doped with SnO_2 (10%). It has a good conductivity together with the transparency in the visible and UV region of light. Since the ITO coated glass is commercially available and no additional coating is needed, the total cell assembling procedure is the same as in the case of normal q-plate manufacturing. At the same time there are more strict requirements for the cleanness of the glass, since the hydrophobic behavior of the ITO differs from the one of the bare glass substrate, and efficient cleaning from organic contamination is necessary to guarantee the uniform distribution of the surfactant material during spincoating. Electrically tunable q-plates were made with all the methods, discussed in section 3.2: PI rubbing, PI photoalignment and SD1 photoalignment. The transmittance of all the samples was around $87 \pm 1\%$. The main contribution to the losses was the lack of antireflection coating on the glass substrates and no significant difference was found between the samples, prepared by different techniques. These losses are easily compensated by a corresponding coating so all our results were normalized with

respect to the transmittance of the q-plates. The characterization of the q-plates efficiency and tunability is basically divided in two parts:

- an analysis of the STOC dependence from the electric field and of the maximum and minimum conversion efficiencies of the q-plate;
- a test of the mode purity of the converted part of the beam.

Since in the case of circular input polarization, the outcoming converted and non-converted parts of the beam are put into orthogonal polarizations, an easy method to analyze the STOC efficiency exists. The experimental setup, used for such measurement is shown in Fig. 3.5. A linearly polarized laser beam is converted into circularly polarized by the quarterwave plate $QWP1$ and to made pass through a q-plate. The output light state is a superposition of the converted and non-converted photons that have orthogonal circular polarization state, according to (3.4). This superposition is subsequently converted into linear vertical and horizontal polarization state by another quarter-wave plate $QWP2$ and then separated by a polarizing beam-splitter (PBS). This way, if the incident polarization state is $|V\rangle$ and the optical axes of $QWP1$ and $QWP2$ are rotated through an angle of $-\pi/4$ then the non-STOC part of the beam, that will have $|H, 0\rangle$ will be transmitted by the PBS, while the STOC part, in the state $|V, \ell\rangle$ will be reflected by the PBS. The two exit gates of the PBS can be swapped by rotating the $QWP2$ through an angle of $\pi/2$. The q-plate, placed between the QWPs was connected to an AC power supply, so to control the electric field, applied to the LC film. The alternating current is usually used instead of a constant voltage so to eliminate the possible charge accumulation on the borders of the LC layer. Such accumulation may happen in the case of the DC voltage due to the presence of ionic impurities inside the nematic LC and may interfere with the functioning of the sample and even damage it. All the electrically tunable q-plates were analyzed this way. Some images of the outcoming beam profiles are shown in Fig. 3.6. These pictures were taken by sending a circularly polarized beam into q-plates with different topological charges. The applied voltages were corresponding to the maximum conversion efficiency or an intermediate value where only a portion of the beam was converted. In the case of maximum STOC a typical "doughnut" shape is observed, with the radius of the dark region, proportional to the OAM order. If the STOC efficiency is not at maximum the singularity decays into a set of smaller dark spots, with their number equal to the ℓ value. The parameter, chosen to characterize the q-plate tunability was the contrast ratio between the converted part intensoty P_c and non-converted P_u, defined as $\rho = (P_u - P_c)/(P_u + P_c)$. The plots of the contrast ratios as a function of the applied voltage for the samples, prepared with rubbing and PI photoalignment are shown in Fig. 3.7. Both plots show a clear presence of the threshold - voltage value under which no reaction

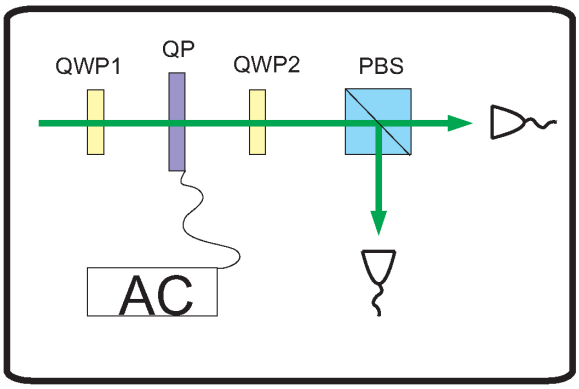

Figure 3.5: The setup used for the q-plate tuning characterization, based on the polarization separation of the converted and non-converted parts of the beam. The Q-plate (QP) is sandwiched between the two quarterwave plates QWP1 and QWP2, rotated though an angle of $\pm 45°$. The orthogonally polarized portions of the beam are then separated by a PBS and STOC and non-STOC components are sent into the detectors.

of the LC happens, a typical effect in the LC cells with planar alignment. Once the threshold is surpassed a reorientation of the LC happens, changing the birefringence Δn of the cell. This change is accompanied by the phase retardation change and is visible as the oscillations of the converted (and non converted on the other side) power fraction of the beam. The phase retardation is given by $\Delta\phi = 2\pi\Delta n d/\lambda$, where d is the thickness of the cell and λ is the wavelength of the impinging light. The q-plates prepared with the rubbing had mylar spacers and during the assembling no strong pressure was applied to the cell. In contrast, the q-plates made with PI photoalignment had different assembling process. This resulted in big difference in the actual cell gap (thickness of the LC layer) of the q-plates, influencing the total phase retardation change and thus the period of the oscillations. As we can see from Fig. 3.7, the rubbed q-plate had very high number of the oscillations immediately after the threshold value, while the photoaligned q-plate has only one maximum in all the region of the applied voltages, meaning that the real cell gap of the rubbed q-plate had much higher value that $6\mu m$. The maximum conversion efficiency (normalized with respect to the transmittance) was $94 \pm 1\%$ for the rubbed q-plate and $99 \pm 1\%$ for the PI photoaligned q-plate. It is worth noting, that even taking into account the absence of the antireflection coating, that gives around 82% of the total conversion efficiency, the q-plates overcome by far the most used up to now holographic technique with typical maximum efficiencies of 40% and presents a very good alternative for the OAM generation.

Same characterization was done for the q-plates made with SD1 photoalignment. Since all the SD1 samples were prepared with the same proce-

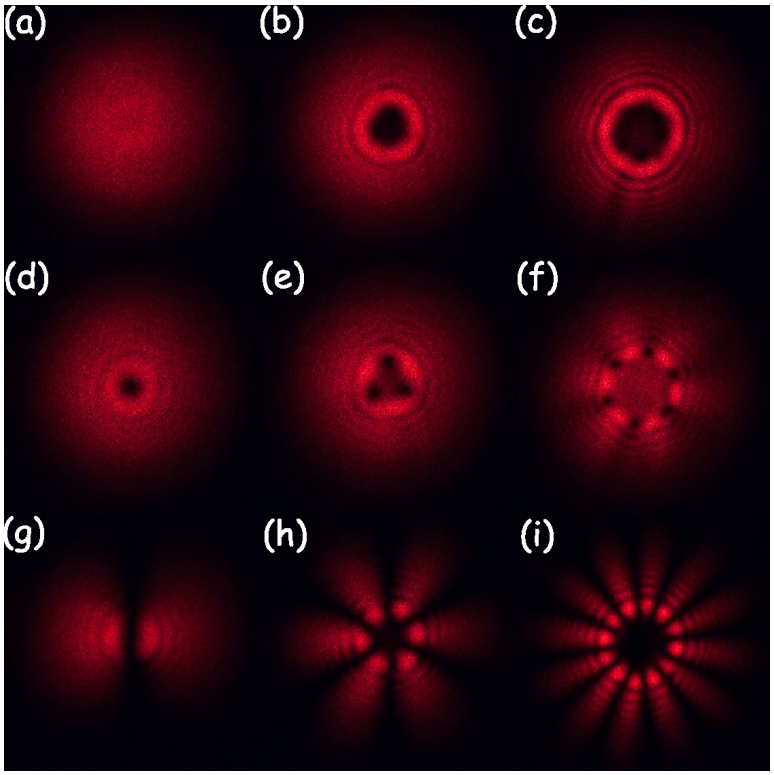

Figure 3.6: Beam profiles after passing the q-plate. (a) – the q-plate is tuned to $\delta = 0$, performing no STOC; (b)-(d) – the q-plates with $q = 1.5$, 3 and 0.5 are tuned to the maximum STOC, generating $\ell = 3$, 6 and 1 beams respectively; (e)-(f) – the q-plates with charges 1.5 and 3 are detuned to an intermediate phase retardation, resulting in a superposition of TEM_{00} and OAM beams; (g)-(i) – corresponding Hermite-Gaussian HG_ℓ modes with $\ell = 1$, 3 and 6.

dure and same materials, the qualitative and quantitative results were similar, so only $q = 0.5$ q-plate characterization curve is reported in Fig. 3.8. The measurements, however, were taken for two different wavelengths, 534.5 nm and 633 nm, of the input laser beam. The maximum conversion efficiency for the analyzed sample was found to be $99.8 \pm 0.1\%$. The threshold value of 1.5 V is also in correspondence with the typical values for the liquid crystal MLC 6080 mixture, photoaligned by the SD1 surfactant.

Since there are usually more than one maximum of the conversion efficiency a question about the working voltage region selection arises. For the LC-based electro-optical devices a region between last minimum and maximum (or last two maximums) is usually selected. Despite the light nonlinearity in the STOC dependence from the voltage applied (that can be seen as the change of the oscillations period for the high voltages), there are

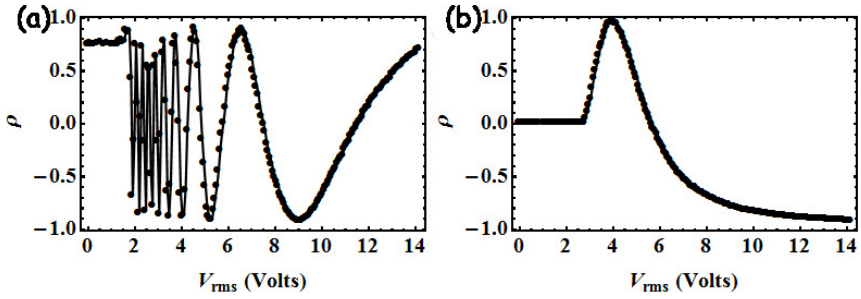

Figure 3.7: Normalized power of the converted part of the input beam as a function of the voltage, applied to two different q-plates. (a) – q-plate made with rubbing, (b) – polyimide photoaligned q-plate. The measurements were taken at the cells temperature $30°C$.

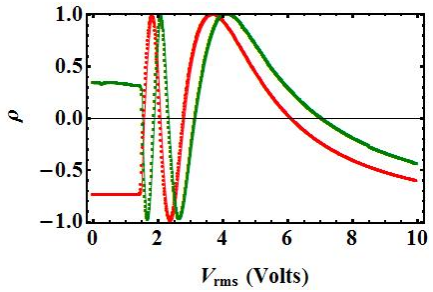

Figure 3.8: Normalized power of the converted part of the input beam as a function of the voltage, applied to the LC cell made by SD1 photoalignment. Red line - 633 nm input beam wavelength, green line - 534.5 nm input beam wavelength. The converted power values were normalized with respect to the total light power output from the q-plate. The measurements were taken at the cells temperature $25°C$. Data refer to the $q = 0.5$ q-plate.

some significant advantages for this choice. First of all the behavior of the cell is much more stable when the voltages are far from the threshold, so the power source has no strict requirements for stability and step resolution of the voltage generated. Second, the temperature stability is also higher far from the threshold, so the occasional temperature change will not influence the STOC efficiency when the high voltage is applied. Another important point is the speed of the LC reorientation that depends on the voltage applied. While the reorientation process is slow for the voltages close to the threshold, its speed increases significantly with the increase of the electric field applied. The switching times of the PI and SD1 photoaligned q-plates were also tested by sending two successive voltages pulses corresponding to the minimum and maximum conversion efficiency. The outcoming converted power fraction was analyzed by an oscilloscope and the time dependence of

the conversion efficiency is shown in Fig. 3.9 for the PI photoaligned q-plate and Fig. 3.10 for the SD1 photoaligned q-plate. The switching time of the

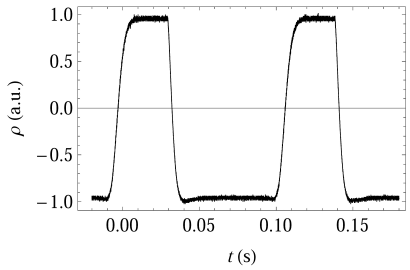

Figure 3.9: Q-plate time behavior upon sending two consecutive electric pulses that correspond to the minimum and maximum conversion voltages. Data refer to the $q = 1$ q-plate, prepared by PI photoalignment.

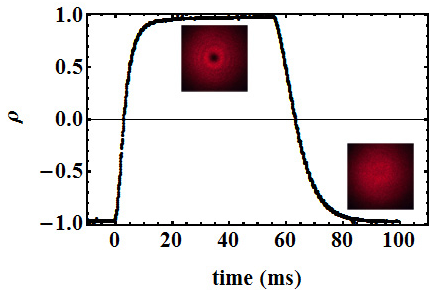

Figure 3.10: Q-plate time behavior upon sending two consecutive electric pulses that correspond to the minimum and maximum conversion voltages. The insets show the switching of the optical vortex beam of $\ell = 1$ order. Data refer to the $q = 0.5$ q-plate.

nematic LC, of course, cannot compete with the frequencies of the electro-optical devices and the electric functioning of the q-plate by itself is limited to the same working speeds as SLM (that is also an LC based device). High working speed, however may be useful to compensate the occasional instability of the power supply or temperature change.

The next step of the q-plate analysis is the measurement of the purity of the generated mode. Such measurement must be based not on the polarization separation of the converted and non-converted part of the beam, but on the study of the phase structure of the converted part of the beam only. A qualitative estimation can be done by seeing the interference pattern of the OAM-carrying beam and a plane or spherical wave (see Fig. 3.11). The interference picture must give typical fork-like or spiral-like pattern where from the number of line dislocations (in the case of plane wave interference) or from the number of spirals (in the case of spherical one) the OAM or-

der of the beam can be recovered. This measurement, however gives little information about the possible residual TEM_{00} beam fraction or other "impurities" of the phase profile and can only give a confirmation of the q-plate functioning, but not the details of its efficiency. Moreover the counting of fringes or spirals can become difficult for the higher orders of the OAM.

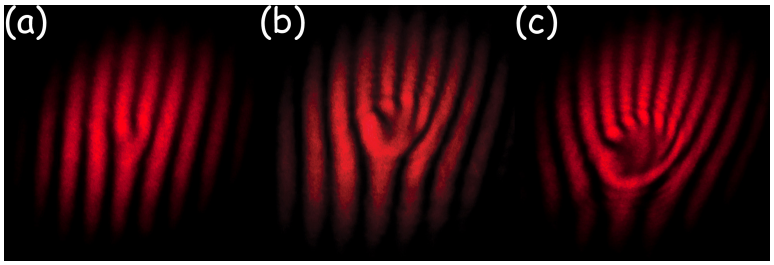

Figure 3.11: Interference patterns of the optical vortex modes of order (a) – $\ell = 1$, (b) – $\ell = 3$, (c) – $\ell = 6$ and a plane wave. The mode order ℓ is equal to the difference between the fringes number below and above the singularity.

Another method that allows to reconstruct the beam OAM structure is to project the beam onto a fork hologram of corresponding order. In this case, depending on the purity of the OAM mode, a portion of the beam will be converted onto the TEM_{00} mode that can be selected with a pinhole or a single-mode optical fiber. After the normalization with respect to the hologram efficiency a percentage of the OAM content can be recovered from this measurement. This technique was used to test the temperature tunable q-plates [33]. A tomography of the OAM content can also be done by holograms [45]. In this case, the process is identical to the Stokes parameters measurements of the polarization state, where instead of the projection by polarizer onto different polarization basis states, different holograms are used to project the incoming OAM state onto $|\ell\rangle$, $|-\ell\rangle$, $|h_\ell\rangle$, $|v_\ell\rangle$, $|a_\ell\rangle$ and $|d_\ell\rangle$. This method allows to reconstruct the density matrix of the OAM state even when the actual OAM space used has higher number of dimensions than 2D.

A technique different from the holograms to test the cleanness of the mode may involve interferometric sorting setups [46, 47]. These interferometers allow to spatially sort the beam according to the order of the OAM it carries with theoretical 100% efficiency. Such sorting can, for example, separate the TEM_{00} part of the beam from the optical vortex part. Similar setup was used to test the electrically tunable q-plate made with the rubbing technique. The setup and its functioning will be described briefly in this section, while a more detailed study of the interferometer and its applications will be given in section 4.2. The device, used to test the q-plate is Polarizing Sagnac interferometer (PSI). The Sagnac interferometer is made up of a polarizing beam splitter (PBS) and three mirrors (M), as shown in

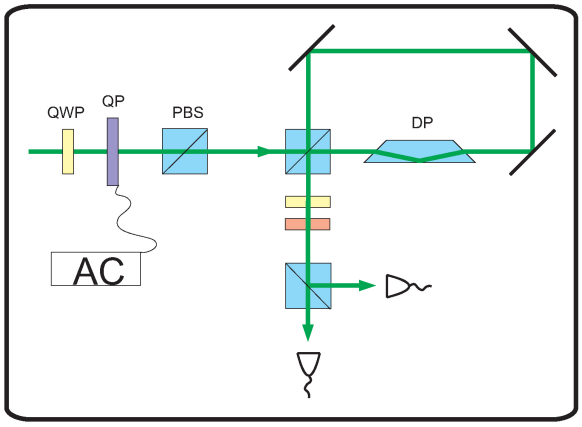

Figure 3.12: The setup used for the q-plate mode purity analysis, based on the Polarization Sagnac interferometer

Fig. 3.12 and a Dove prism is inserted in one arm of the interferometer. The $|H\rangle$- and $|V\rangle$-polarized components of the beam emerging from the q-plate are initially separated by the PBS and travel through the interferometer in opposite directions until they are recombined on exit by the same PBS. Equal optical paths of the counterpropagating beams render this interferometer particularly noise insensitive, thus removing the need for active control of the interferometer length [48]. The Dove prism is a special type of prism, widely used in image processing. The Dove prism is shaped as a isosceles triangle whose single angle is cut parallel to the base. Such prism produces a mirror reflection of the impinging beam without changing it's propagation direction and if two Dove prisms, rotated through a relative angle of α are put in cascade, the outcoming beam is rotated through the angle 2α with respect to the incident one. A plane wave propagates through the Dove prism with no changes at all. In the case of optical vortices that have cylindrical symmetry no image (intensity) rotation happens, but the spiral phase plane is rotated only. This way the reflection in the Dove prism tilted at angle θ adds a phase factor $\exp(2i\ell\theta)$ to the OAM eigenstate $|\ell\rangle$ and changes $|\ell\rangle$ into $|-\ell\rangle$. In our case, moreover, because of the counterpropagation, the $|H\rangle$-polarized beam sees the Dove prism tilted at angle θ and the $|V\rangle$-polarized beam sees the Dove prism tilted at angle $-\theta$. For the $\ell = 2$, if the Dove prism is rotated through the 22.5° the relative phase change between $|H\rangle$ and $|V\rangle$ components of the beam is equal to $\exp(2i2\pi/8) = \exp(i\pi/2)$. If the initial polarization state is, for example, $|A,\ell\rangle = \frac{1}{\sqrt{2}}(|H\rangle + |V\rangle)|\ell\rangle$ it is converted into $|D,\ell\rangle = \frac{1}{\sqrt{2}}(|H\rangle - |V\rangle)|\ell\rangle$ by the PSI. The plane wave ($\ell = 0$ mode), instead, remains in the same polarization state, unaffected by the Dove prism. This way the converted and non-converted portion of the beam are separated in polarization and then in the propagation direction (by a

PBS) even if the initial polarization state was the same for both components. This type of sorting is no more based on the polarization, but on the beam phase structure only, even if the result of the sorting consists in the polarization separation of the two different components of the beam.

To test our q-plates, the outcoming beam was antidiagonally polarized by a polarizer (loosing 50% of intensity) and sent through the PSI. After the PSI the $|A\rangle$ and $|D\rangle$ components were converted into $|H\rangle$ and $|V\rangle$ polarizations by a halfwave plate and separated by the PBS. An additional quarterwave plate was placed after the PSI so to compensate polarization and phase changes, induced by the Dove prism and mirrors. The measurements of the contrast ratio between the two exits of the PBS were taken and are shown in Fig. 3.13. The correlation of the contrast ratio, measured by the setup, shown in Fig. 3.5 and the measurements done by the PSI was found to be 99.6%. The $q = 0.5$ q-plate made by the SD1 photoalignment was

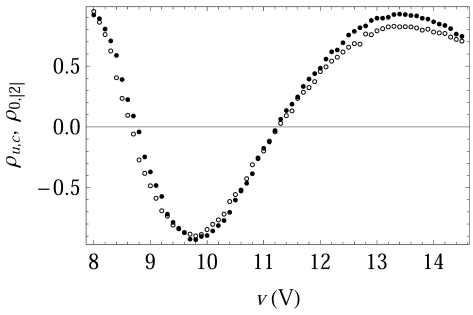

Figure 3.13: Contrast ratio $\rho_{u,c}$ vs voltage for unconverted-converted components of the output sorted with respect to polarization (dots). Contrast ratio $\rho_{0,|2|}$ vs voltage for OAM $\ell = 0$ and $\ell = |2|$ components of the output beam measured with Dove-Sagnac sorter (circles). Data refer to q-plate, prepared by the UV-photoalignment technique.

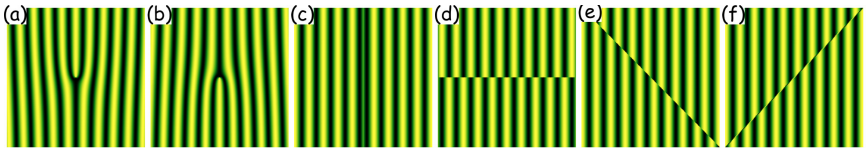

Figure 3.14: Examples of the six CGHs, used for the quantum state tomography. The holograms correspond to the projection operators on the basis states $|1\rangle_o$, $|-1\rangle_o$, $|h_1\rangle_o$, $|v_1\rangle_o$, $|a_1\rangle_o$ and $|d_1\rangle_o$ respectively.

also tested in terms of mode purity. For doing this a quantum tomography technique was adopted. A set of six holograms (see Fig. 3.14) project the OAM state into the six basis states $|1\rangle$, $|-1\rangle$, $\frac{1}{\sqrt{2}}(|1\rangle + (|-1\rangle)$, $\frac{1}{\sqrt{2}}(|1\rangle - (|-1\rangle)$, $\frac{1}{\sqrt{2}}(|1\rangle + i(|-1\rangle)$ and $\frac{1}{\sqrt{2}}(|1\rangle - i(|-1\rangle)$. The difference between

intensities measures is then used to reconstruct the density matrix of the state in the same way as the Stokes parameters are used to reconstruct the polarization matrix. The measurements were done for the circularly right and left polarization inputs, that correspond to the $|1\rangle$ and $|-1\rangle$ OAM states generated (in the case of maximum conversion tuning of the q-plate) and the linearly polarized input light that, together with the polarizer can be used to generate and equalweight superposition of the $|1\rangle$ and $|-1\rangle$ states (this technique will be discussed more in details in the chapter 4). The corresponding density matrices are reported in Figs. 3.15 (a)-(c) for all three states measured and the fidelities of the states generated were $97.5 \pm 0.5\%$, $99.4 \pm 0.5\%$ and $98.9 \pm 0.5\%$ of the $\ell = 1$, $\ell = -1$ and superposition states respectively. An additional test was done on the q-plate with $q = 0.5$, aimed

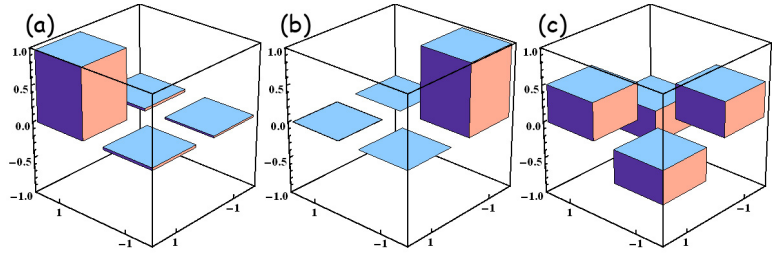

Figure 3.15: Real parts of the density matrices of the OAM states (a) – $|1\rangle$, (b) – $|-1\rangle$ and (c) – $\frac{1}{\sqrt{2}}(|1\rangle - i(|-1\rangle)$, generated by a $q = 0.5$ q-plate, reconstructed via quantum state tomography.

to show experimentally the strong correlation between the polarization and OAM states of the output light from the q-plate. For doing that, the q-plates was illuminated with an elliptically polarized TEM_{00} beam, and the generated beam was analyzed in three different ways:

- the polarization state was analyzed with the circular polarizer, so to detect the fraction of the intensity that was in $|R\rangle$ polarization state and then the OAM state of the whole output beam was analyzed with a fork hologram, so to detect the fraction of the intensity that carried the $|1\rangle$ OAM state

- the polarization state was analyzed with the circular polarizer, so to detect the fraction of the intensity that was in $|R\rangle$ polarization state and then the analyzed fraction of the beam was tested with the hologram, so to detect the fraction of the selected beam that was in the $|1\rangle$ OAM state

- the OAM state was analyzed with the fork hologram, so to detect the fraction of the intensity that was in $|1\rangle$ OAM state and then this analyzed fraction of the beam was tested with the polarizer, so to

detect the fraction of the selected beam that was in the $|R\rangle$ polarization state

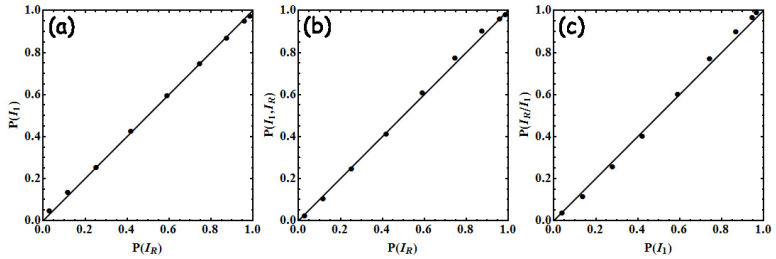

Figure 3.16: Correlations between each two signals for the three different types of measurements.

The first test allowed to find out how the total number of the $|R\rangle$ state correlates with the total number of the photons in the $|1\rangle$ state, without a precise information if the $|R\rangle$ photons are in the $|1\rangle$ OAM state or not. The latter two measurements allow to find the conditioned probabilities $P(R/1)$ and $P(1/R)$ that correspond to the probability of $|R\rangle$- polarized photon to be in the $|1\rangle$ state and viceversa. According to the theory, both the correlation between the number of the $|R\rangle$ polarized photons and $|1\rangle$ OAM photons and the two conditioned probabilities should give unit value, meaning that every photon in the $|R\rangle$ state must carry OAM order $\ell = 1$ and every $|1\rangle$ photon in turn must have circular right polarization. The experimental results showed that the standard deviation from the unit value is equal 0.015, 0.01 and 0.023 for the three corresponding relations.

Chapter 4

Classical Optics applications

4.1 Polarization controlled OAM eigenmodes generation and associated geometrical phase [49]

The q-plate action on the impinging laser beam is not limited to the generation of the pure OAM eigenmodes of fixed $\ell = 2q$ order. While for the circularly polarized input TEM_{00} beam the operation, performed by the q-plate is described by Eqs. (3.4), in the case of the arbitrary elliptical polarization the outgoing state will be not a pure mode, but a complex superposition of different OAM modes of opposite sign in different polarization states. The aim of the work, described below, was to demonstrate an easy and efficient control of the OAM state of a light beam that can be achieved by the STOC process. Arbitrary and continuously controllable linear combinations of LG_2 modes have been generated in a very simple way and with efficiency exceeding 90% by manipulating the input beam polarization only, creating a one-to-one equivalence between a certain polarization states and 2D OAM states that covers all the Poincaré sphere. Our method provides a highly efficient tool that, for example, can be advantageously used to create photonic qudits involving both SAM and OAM degrees of freedom, thus enlarging the amount of information carried by single photons.

The required mapping of the SAM and OAM spaces can be described as

$$(\alpha|L\rangle + \beta|R\rangle)|0\rangle \leftrightarrow (\alpha|2\rangle + \beta|-2\rangle)|D\rangle, \tag{4.1}$$

where α and β are complex coefficients, satisfying the normalization condition $|\alpha|^2 + |\beta|^2 = 1$.

The experimental setup is shown in Fig. 4.1. The polarization of the light beam entering the q-plate is controlled by the QHQH waveplate sequence $QW(90°)HW(-\gamma/4)QW(0°)HW(90°+\delta/4)$, where the orientation angles of each plate counted from the horizontal plane are in parentheses. As can be easily shown, this sequence of waveplates applies to the input polarization state first an SU(2) transformation consisting of a rotation of angle γ around

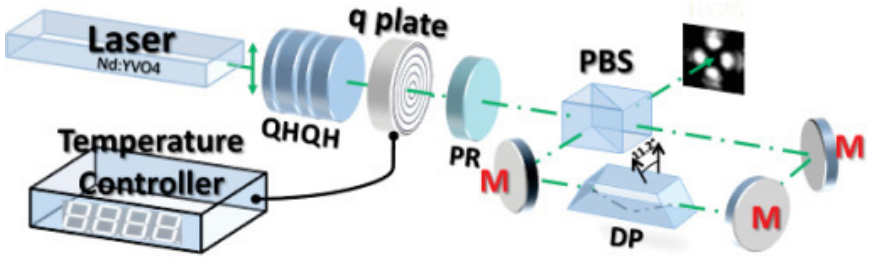

Figure 4.1: Experimental setup for generating polarization-controlled linear combinations of LG_2 beams. Legend: HQHQ - set of waveplates to control the beam polarization; PR - polarization rotator; PBS - polarizing beam-splitter; DP - Dove prism; M - mirror.

the y axis of the SAM Poincaré sphere and then a rotation of an angle δ around the z axis. After this QHQH set, we inserted a tuned q-plate (QP), a polarization rotator (PR) of 45° and a Polarizing Sangac interferometer (PSI), already described in the chaper 3. In the PSI, the Dove prism was rotated by 11.25° from the horizontal plane. The QP, PR, and PSI are the heart of our apparatus, because they realize the required mapping (4.1). From Eqs. (3.4), the action of the q-plate on an elliptically polarized TEM_{00} beam is given by

$$\widehat{QP}(\alpha|L\rangle + \beta|R\rangle)|0\rangle = \alpha|R,2\rangle + \beta|L,-2\rangle = \\ = \frac{1}{\sqrt{2}}[|H\rangle(\alpha|2\rangle + \beta|-2\rangle) - i|V\rangle(\alpha|2\rangle - \beta|-2\rangle)] \tag{4.2}$$

where the charge of the q-plate is taken as $q = 1$ for simplicity. From Eq. (4.2) we see that insertion of a linear polarizer after the QP would already select the desired linear combination of $|2\rangle$ and $|-2\rangle$ states. Such method is very simple, but this would also reduce the maximum conversion efficiency to 50% [50]. The PSI scheme shown in Fig. 4.1 allows one to increase the theoretical efficiency to 100%. In order to calculate the overall effect of the PSI we must add to the action of the Dove prism the action of the three mirrors and BPS that add an odd number of reflections to both the counterpropagating beams, so the final value ℓ of the OAM after the interferometer is the same as in the input beam. With the substitutions $|H,\ell\rangle \to e^{2i\ell\theta}|H,\ell\rangle$, $|V,\ell\rangle \to e^{-2i\ell\theta}|V,\ell\rangle$ and setting $\theta = \pi/16$ in Eq. (3.4) we obtain, up to the phase factor, the state after the PSI as

$$\Psi_{out} = (\alpha|2\rangle - i\beta|-2\rangle)|D\rangle. \tag{4.3}$$

The resulting beam is fully polarized and the OAM state is a linear combination of $|\pm 2\rangle$ modes with the coefficients uniquely related to α and β. The phase difference of $\pi/2$ between the two terms on the right can be eliminated by means of the PR, located before the PSI, which introduces a retardation

of $\pi/2$ between the circular polarization components of the input beam. With such compensation, the correct SAM-OAM Poincaré spheres mapping (4.1) was achieved.

To show the flexibility of our apparatus in manipulating the light OAM, we performed a set of measurements in which we slowly modulated the polarization of the input TEM_{00} beam in order to drive the state of the output beam along a predetermined trajectory on the OAM Poincaré sphere. In this way, arbitrary states in the $|\ell| = 2$ subspace were easily and continuously generated starting from a TEM_{00} laser beam. The power conversion efficiency from TEM_{00} $|H\rangle$ polarization to $|\ell| = 2$ modes was found to exceed 90% for all the modes. This efficiency is larger than the typically obtainable ($\simeq$40%) with blazed holograms. In our experiments, we measured the OAM content of the output beam in several points on the Poincaré sphere by recording the intensity profile and the pattern obtained by interference with a $|D\rangle$-polarized TEM_{00} mode as reference beam. For the sake of brevity, the interferometric apparatus adopted to record such interference patterns has not been reported in Fig. 4.1. The results are shown in Figs. 4.2-4.4. In the measurements we used a 532-nm TEM_{00} $|H\rangle$-polarized laser beam

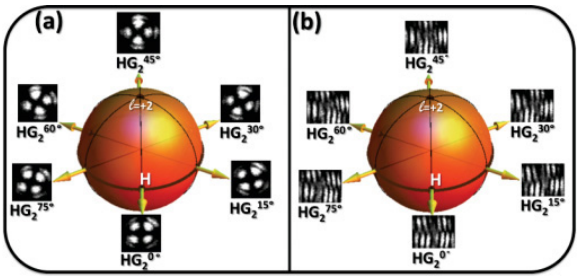

Figure 4.2: Trajectory along the equator of the Poincaré sphere. H is the starting and ending point of the closed path. (a) Intensity profiles of generated beams corresponding to differently rotated HG_2 modes. (b) Corresponding interference patterns with a $|D\rangle$-polarized TEM_{00} reference beam. As the state travels along the equator both the intensity and interferogram patterns rotate through an angle between 0° and 90°.

and thermally tuned q-plate [33]. Fig. 4.2 shows the intensity profiles and interferograms of the HG_2 modes represented by the points located on the equator of the OAM Poincaré sphere. The modes shown in Fig. 4.2 were generated by fixing the axis of the first halfwave plate in the QHQH sequence to 0° and rotating the axis of the second halfwave plate from 90° to 180°. The input polarization state circulates along the equator of the SAM Poincaré sphere starting from $|H\rangle$, i.e. $\gamma = 0$ and $0 \leq \delta \leq 2\pi$, denoted by the point H on the sphere. The rest of the apparatus mapped the equator of the SAM sphere into the equator of OAM sphere, which represents a continuous sequence of HG_2 modes whose transverse intensity and phase distributions

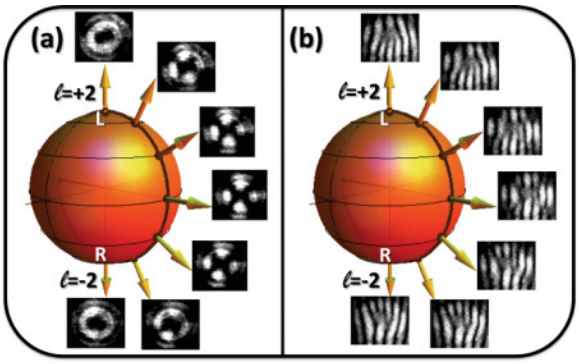

Figure 4.3: Trajectory along a meridian of the Poincaré sphere.(a) Intensity profiles of generated beams corresponding to different linear combinations of $LG_{\pm 2}$ modes. (b) Corresponding interference patterns with a TEM_{00} $|D\rangle$-polarized reference beam.

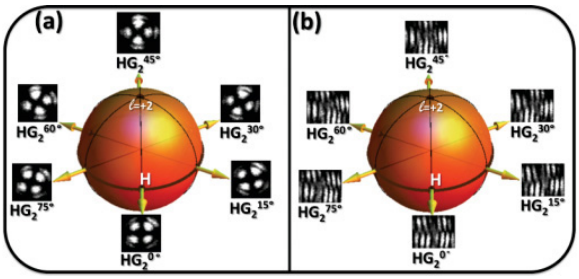

Figure 4.4: A possible closed path over the OAM-Poincaré sphere. The path L $\rightarrow$ H $\rightarrow$ A $\rightarrow$ L starts and ends at the North pole, which is associated to $|+2\rangle$. H is the point associated to the $|h\rangle$ and A is the point associated to $|a\rangle$. (a) Intensity profiles of the generated beam at different points of the path. (b) Corresponding interference patterns with a TEM_{00} $|D\rangle$-polarized reference beam.

rotate counterclockwise from 0° to 90° with the global phase being π shifted over the closed path, as shown in Fig. 4.5(a). Such a phase shift over the cycle was inferred comparing the intensity profiles of the fringe patterns along the transverse direction of both the initial and the final states, represented in Fig. 4.5(a) by a dashed and a continuous line, respectively. Of course, when the initial state of the input beam is represented by a point located outside the equator, i.e., $\gamma \neq 0$ on the Poincaré sphere, the rotation of the axis of the second halfwave plate in the device QHQH from 90° to 180° will yield into a variation of δ from 0 to 2π. This will drive the OAM state along a parallel on the Poincaré sphere.

Analogously, the modes represented by the points located along a meridian trajectory on the OAM Poincaré sphere were produced fixing $\delta = 0$ and

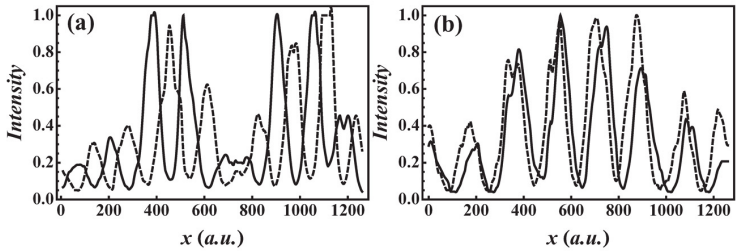

Figure 4.5: FIG. 5. Interference patterns for two different closed trajectories on the Poincaré sphere. (a) Circular path along the equator, as shown in Fig. 4.2. In this case, there is a π change in the phase when the path is closed. (b) Path shown in Fig. 4.4. In this case there is a $\pi/4$ change in the phase when the path is closed. Dashed and continuous lines show the fringes of the initial and final states, respectively.

driving γ from $-\pi/2$ to $+\pi/2$ in the QHQH device, i.e., rotating the axis of the first halfwave plate in the QHQH device from $+22.5°$ to $-22.5°$. Figure 4.3 shows the continuous passage from the LG_2 mode, i.e., doughnut intensity and down-fork interferogram, to the HG_2 mode rotated by 45°, crossing the equator, up to the LG_{-2} mode, i.e., doughnut intensity again and up-fork interferogram. The field distributions of the modes corresponding to points located along a meridian at intermediate positions between the poles and the equator are also shown.

On the grounds of the previous two experiments, it is clearly possible to move between two arbitrary OAM states passing through a continuous series of states represented by the points of suitable arcs of parallels and meridians. Furthermore, in principle, any path connecting two arbitrary points on the Poincaré sphere could be realized by rotating simultaneously both the halfwave plates in the QHQH device in order to approximate as best as possible the path by a polygonal chain consisting of small arcs of parallel and meridians. Finally, we exploited this general feature in a simple case to drive the OAM state along a closed path L $\rightarrow$ H $\rightarrow$ A $\rightarrow$ L on the Poincaré sphere (see Fig. 4.4), hinged on the North pole L. Therefore, starting from the state $|2\rangle$ (point L in the figure), we rotated the first halfwave plate from $+22.5°$ to $0°$, the second halfwave plate being fixed at $90°$. After this operation, the OAM state turns to be $|h\rangle$ (point H in the figure). Then, the first halfwave plate being fixed at $0°$, the second halfwave plate was rotated from $90°$ to $112.5°$, producing the OAM state $|a\rangle = (|h\rangle + |v\rangle)/\sqrt{2}$ (point A in the figure), which is the HG_2 mode corresponding to the linear polarization state $|A\rangle$. Finally, the path was closed, maintaining the second halfwave plate fixed at $112.5°$ and rotating the first one from $0°$ to $+22.5°$. Fig. 4.4 shows some intensity profiles and interferograms corresponding to the closed

path considered. As inferred from the interferograms corresponding to the North pole in the initial and final states, closing the path results in the multiplication by a Pancharatnam geometric phase. The observed fringe shift due to Pancharatnam geometric phase over a cycle is shown in Fig. 4.5(b). The intensity profiles of the fringe patterns along the transverse direction are shown for both the initial and the final states simultaneously, maintaining the same origin for the transverse coordinate in both patterns for comparison. Dashed and continuous lines show the fringes related to the initial and final states, respectively.

Figure 4.5 shows both the phase shift related to the circulation along the equator (Fig. 4.5(a)) and that related to the circulation along the triangular path (Fig. 4.5(b)). As expected, in both cases a phase shift equal to half the solid angle subtended by the path on the OAM Poincaré sphere was found [28]. The geometrical phase acquired by a light beam when the OAM state is moved along a closed path on Poincaré sphere was observed some time ago [51]. However, in the last experiment the light OAM content was changed discontinuously by having the beam pass through a sequence of fixed Dove prisms and cylindrical lens converters. In the present case, the beam OAM was changed adiabatically and the phase continuously monitored along the path. Note that the Pancharatnam geometric phase is already present when we close the state path on the SAM Poincaré sphere of the input beam. One of the issues of our experiment is therefore to demonstrate that the STOC process is able to coherently transfer global phase shifts, such as geometric phase shifts, from the SAM to OAM degree of freedom. The one-to-one SAM mapping into the OAM Poincaré sphere allows phase measurements with constant fringe visibility along any path, in particular along a closed path, which is impossible in experiments on the Pancharatnam phase based on polarization only [28].

This works clearly showed the versatility of the q-plate as fast and efficient OAM generation device. Thanks to the q-plate it was possible to achieve easy and continuous control on the transverse modes of a laser beam. A particular Dove prism-based Sagnac polarizing interferometric configuration allowed us to generate with efficiency higher than 90% arbitrary combinations of LG_2 modes in the $|\ell| = 2$ subspace, by changing the polarization of the input TEM_00 laser beam. When closed paths are described on the SAM Poincaré sphere, identical closed path are described on the OAM Poincaré sphere and the resulting Pancharatnam geometric phase is transferred with no change from the SAM to the OAM degree of freedom. Our apparatus can work even in the single-photon regime, so it could be useful in many classical and quantum optics applications where easy, fast, and continuous manipulation of OAM is necessary.

Despite the q-plate being the core of the setup, Polarizing Sagnac interferometer is another promising tool for OAM manipulation that was also studied separately in greater detail.

4.2 Dove-prism Polarizing Sagnac Interferometer [52]

While sorting photons according to their different polarization states is very easily accomplished by polarizing beamsplitters and birefringent waveplates, sorting photons according to their different OAM modes is a more complex problem. Till now few techniques were proposed for this aim [24, 46, 47, 53]. The most used is a combination of a specific computer generated hologram with a pinhole or a single-mode fiber [24]. Such method, despite its universality (thanks to SLMs) suffers from the the low overall transmission efficiency of the hologram and optical fiber (or pinhole) system. Rarely the overall efficiency of such systems can exceed 40%. A number of setups, involving Mach-Zehnder interferometer and two Dove prisms [46, 47] or two confocal cylindrical lenses acting as OAM mode converters [53] was also proposed. These techniques have a theoretical efficiency of 100% and may be used in the single photon regime, but require high mechanical stability, careful path matching of the arms of the interferometer and careful positioning and alignment of the cylindrical lenses. The combination of the q-plate and a pinhole, or single-mode fiber can also work as a mode sorter [33] or as a device that transfers the OAM information into the SAM space that is easily analyzable by common methods [45]. Other detection methods proposed are usually not applicable in the single-photon regime.

The PSI setup, proposed in [45] and exploited in [49, 40] in fact is a variation of the previously proposed interferometric techniques. This setup allows to reach 100% sorting efficiency, works with single photons, and has a good stability because of the self compensation of the optical paths inside the interferometer. Moreover, the use of single Dove prism further simplifies the setup. In the following, I will further discuss and demonstrate experimentally the ability of the PSI to sort photons carrying different OAM values, and will present some additional applications of the same setup in the spinorbit processing, such as the realization of c-NOT gate, efficient photon spinorbit Bells states measurement and entanglement control of the spinorbit Schmidt state - a two-component non-maximally entangled state in the spinorbit Hilbert space.

Let us first generalize the approach to the PSI sorting. As it was previously mentioned, the Dove prism, inserted inside the interferometer, induces a phase shift that has different sign for the two counterpropagating components. Inserting in the Dove prism, rotated through an angle α with respect to the interferometer plane is equivalent to insert two Dove prisms in the two arms of the Leach interferometer [46], rotated with respect of each other through an angle 2α. After having passed through the interferometer, the two counterpropagating orthogonal polarizations $|H\rangle$ and $|V\rangle$ will gain a relative phase of $4\ell\alpha$, where ℓ is the OAM mode order. In this way, our setup is able to induce an ℓ dependent change of the polarization state of the incident beam. The OAM sign remains unchanged, however, because the total

number of reflections from mirrors, PBS and Dove prism is even for both polarizations. Neglecting scattering and absorption losses, the theoretical transparency of the PSI device is 100%. As shown in the next section, the PSI can simulate the Leach interferometer for OAM photon sorting beyond the $\ell = 0$ and $\ell = 2$ sorting, performed in Sec. 3.3. But it should be noticed that the PSI handles polarization too, so it can perform a wider set of operations in the OAM and also in the full photon spinorbit space. For example, when qubits formed by opposite OAM eigenstates $|\pm\ell\rangle$ are considered, the PSI may simulate a $\pi/2$ cylindrical lens converter, changing LG_ℓ modes into HG_ℓ modes [49].

The ℓ-dependent relative phase shift, induced by the PSI can be exploited for the sorting input photons sharing the same polarization state according to their different OAM values into orthogonal polarization states of the exit beam. The further separation over different path is then easily and efficiently accomplished by suitable waveplates and PBS. Let us assume the impinging photon having a definite value ℓ of OAM and definite polarization state $|\psi\rangle = a|H\rangle + b|V\rangle$. The action of the PSI with DP at angle α on such a photon state is given by

$$|\psi,\ell\rangle \xrightarrow{\widehat{PSI_\alpha}} ae^{2i\ell\alpha}|H,\ell\rangle + be^{-2i\ell\alpha}|V,\ell\rangle = -i\cos 2\ell\alpha|\psi,\ell\rangle + \sin 2\ell\alpha|\psi',\ell\rangle) \tag{4.4}$$

where $|\psi'\rangle = a|H\rangle - b|V\rangle$. We see that for input states with equally weighted $|H\rangle$ and $|V\rangle$ polarizations (i.e. states with $|a|^2 = |b|^2 = 1/2$), the states $|\psi'\rangle$ and $|\psi\rangle$ are orthogonal, so that they can be easily separated. In this work we assume always an equally weighted input polarization states [1]. Then, from Eq. (4.4) we see that if $2\ell\alpha = k\pi$ (integer k) the polarization state remains unchanged (up to a global phase factor), while if $2\ell\alpha = \pi/2 + k\pi$ the polarization state becomes orthogonal to the incident one. Setting, for example, the angle of the DP to $\alpha = \pi/4$ the PSI changes the polarization of the photons that carry odd values of OAM into the orthogonal state $|\psi'\rangle$, while the photons that carry even values of OAM remain in their $|\psi\rangle$ polarization state. Using a halfwave plate, with optical axis rotated through and angle of $\pi/8$, and a PBS located beyond the PSI the even and odd values of OAM are spatially separated for detection purposes. One or more cascaded PSIs may work as an OAM eigenstates sorter in the same way as the Leach interferometer [46, 47]. As the Leach interferometer, the PSI works in the single-photon regime and has nominal 100% transmission efficiency. The main advantages of the PSI are the use of a single Dove prism and the self-compensation of the optical paths so that no adjustments are required to obtain destructive interference. Unlike the Leach interferometer, however, the PSI handles the OAM content of the two orthogonal polarizations in a different way. This peculiar feature can be exploited for applications

[1] Examples are the diagonal, antidiagonal, left-circular, right-circular polarizations.

different from the OAM photon sorting. A few examples are outlined below.

OAM qubit measurement. In most applications of photon OAM to quantum information and computing, qubit are considered formed by the superposition of only two OAM states. Unlike in the photon spin, case, however, where the two states have opposite eigenvalues, in the case of photon OAM we may form qubits with any two eigenvalues ℓ_1 and ℓ_2. Qubit measurement requires that the two states are sent into different detectors. In the case of the photon SAM this task is accomplished by PBS. In the case of the photon OAM, suitable hologram can be exploited, but the overall efficiency is quite low, usually around 40% or less. Our PSI can be configured so to discriminate *any* pair of given OAM eigenstates $|\ell_1\rangle$ and $|\ell_2\rangle$ in a common initial polarization state by addressing them into orthogonal polarizations. In fact, evaluating Eq. (4.4) for $\ell = \ell_1$ and $\ell = \ell_2$ and imposing that the output polarization states are orthogonal, we find the condition

$$\cos 2(\ell_2 - \ell_1)\alpha = 0 \quad \Rightarrow \quad \alpha = \frac{(2k+1)\pi}{4(\ell_2 - \ell_1)} \tag{4.5}$$

with integer k. In most practical cases, opposite values of ℓ are used. To discriminate such states $|+\ell\rangle$ and $|-\ell\rangle$, the Dove prism must set at $\alpha = \pi/8\ell$. The two orthogonal polarizations at the PSI output are then sent into different paths by conventional PBS. When configured in this way, the PSI behaves in as an OAM beam splitter. The contrast ratio and overall transmission are limited only by constructive defects, so they may be very large as shown in the experimental section.

***TEM*$_{00}$ cleaning.** As said above, in many quantum applications qubits are formed combining the $|+\ell\rangle$ and $|-\ell\rangle$ OAM eigenstates. In these cases, may be of some importance to clean up all other OAM components. Because the OAM eigenstates are usually originated from TEM_{00} laser beams, it is of particular interest to clean up the beam from any residual $\ell = 0$ OAM component. The PSI can be used to this purpose by simply setting the angle of the DP at $\alpha = \pi/(4\ell)$ and polarizing the input photon along the antidiagonal direction. In fact, when Eq. (4.4) with $\alpha = \pi/(4\ell)$ is applied to the qutrit $|\psi_{in}\rangle = a|A,0\rangle + b|A,-\ell\rangle + c|A,\ell\rangle$ we obtain the output state $|\psi_{out}\rangle$ as

$$|\psi_{out}\rangle = -ia|A,0\rangle + b|D,-\ell\rangle - c|D,\ell\rangle, \tag{4.6}$$

so that the input $\ell = 0$ component is left in its initial antidiagonal polarization state and the two $\pm\ell$ components are put into the orthogonal diagonal polarization state. The $\ell = 0$ component can be then easily separated from the ℓ and $-\ell$ by a PBS placed at the output port of the device. Such $\ell = 0$ filtering is useful since most holograms, spiral

phase plates, q-plates etc., commonly used to generate OAM eigenvalues from TEM_{00} beam, do not produce OAM eigenstates with 100% purity due to misalignment and inaccuracies of fabrication. This sorting approach was exploited in the Sec. 3.3, to detect the purity of the eigenmodes, generated by an electrically tunable q-plate. It is worth noting that the $\ell = 0$ component of the input beam is not lost, but sent into one output port of the final PBS. We may then use the same device to filter out the the not zero OAM components leaving a very pure output TEM_{00} mode. This can be useful, for example, to face the serious problem to combine high power ($\simeq$ 100 W or more) with excellent beam quality in lasers systems [54] and Faraday isolators [55, 56] for gravitational wave detection.

Another class of the applications of the PSI is spinorbit quantum computation. Entangled nonseparable photon spinorbit states are the core of many quantum information applications. Such states do not show the most noted property of photon pair – non-locality – nevertheless they exhibit paradoxical quantum features related to the quantum contextuality that renders these single-photon entangled states very interesting for quantum computation purposes. In fact, operations like universal unitary gates, deterministic complete Bell measurement, etc., which are impossible in the two-photon case, can be realized in the case of single-photon with entangled degrees of freedom. Our PSI acts on the photon SAM and OAM simultaneously, so that it can realize some of the most important gates in the photon spinorbit space, such as the c-NOT gate, the unitary gate for Bell's states measurement or a gate to generate spinorbit states with controllable entanglement.

c-NOT gate. The controlled-NOT (c-NOT) gate is the key gate for most of the quantum algorithms based on two qubits. In fact, using c-NOT gates and global phase retarders it is possible to realize any unitary gate in the 4D two-qubit Hilbert space. The c-NOT gate flips the state of one of the qubits depending on the state of the other qubit. If the logical basis of the two-qubit state is given by the four kets $|0,0\rangle$, $|0,1\rangle$, $|1,0\rangle$ and $|1,1\rangle$ and the first qubit is the control one, then the c-NOT gate action performs the following logical operation

$$\begin{aligned} |0,0\rangle \overset{\widehat{cNOT}}{\longrightarrow} |0,0\rangle,\ |0,1\rangle \overset{\widehat{cNOT}}{\longrightarrow} |0,1\rangle \\ |1,0\rangle \overset{\widehat{cNOT}}{\longrightarrow} |1,1\rangle,\ |1,1\rangle \overset{\widehat{cNOT}}{\longrightarrow} |1,0\rangle. \end{aligned} \tag{4.7}$$

If the spinorbit space logical basis is given by $|R,-\ell\rangle$, $|R,\ell\rangle$, $|L,-\ell\rangle$ and $|L,\ell\rangle$, the PSI with the DP angle set to $\pi/8\ell$ performs an OAM c-NOT operation, changing the polarization state of the photons with OAM $+\ell$ into the orthogonal one and leaving the polarization of the photons with $-\ell$ unchanged. The exit polarization is transformed as

$|R\rangle \longrightarrow |A\rangle$, $|L\rangle \longrightarrow |D\rangle$ for the negative OAM value and $|R\rangle \longrightarrow |D\rangle$, $|L\rangle \longrightarrow |A\rangle$ for the positive OAM value. To come back into the circular basis an additional quarter-wave plate with its optical axis oriented at 90° is needed beyond the PSI so that the overall operation is given by

$$\begin{aligned} |L,\ell\rangle &\overset{cNOT+QWP}{\longrightarrow} |L,\ell\rangle; \quad |L,-\ell\rangle \overset{cNOT+QWP}{\longrightarrow} |R,-\ell\rangle \\ |R,\ell\rangle &\overset{cNOT+QWP}{\longrightarrow} |R,\ell\rangle; \quad |R,-\ell\rangle \overset{cNOT+QWP}{\longrightarrow} |L,-\ell\rangle \end{aligned} \tag{4.8}$$

The PSI behaves as a c-NOT gate with the polarization as control qubit, if we take as logical basis the states $|H,h_\ell\rangle$, $|H,v_\ell\rangle$, $|V,h_\ell\rangle$ and $|V,v_\ell\rangle$, where $|h_\ell\rangle = (|\ell\rangle + |-\ell\rangle)/\sqrt{2}$ and $|v_\ell\rangle = (|\ell\rangle - |-\ell\rangle)/i\sqrt{2}$ are the superpositions of OAM states, equivalent to the horizontal and vertical polarization states. In this case the OAM state of the $|H\rangle$ and $|V\rangle$ component will be rotated through an angle of $\pm\pi/4\ell$ respectively and the state of the outgoing photon is given by

$$\begin{aligned} |V,v_\ell\rangle &\overset{cNOT}{\longrightarrow} |V,d_\ell\rangle \overset{DP}{\longrightarrow} |V,v_\ell\rangle; \quad |V,h_\ell\rangle \overset{cNOT}{\longrightarrow} |V,a_\ell\rangle \overset{DP}{\longrightarrow} |V,h_\ell\rangle \\ |H,v_\ell\rangle &\overset{cNOT}{\longrightarrow} |H,a_\ell\rangle \overset{DP}{\longrightarrow} |H,h_\ell\rangle; \quad |H,h_\ell\rangle \overset{cNOT}{\longrightarrow} |H,d_\ell\rangle \overset{DP}{\longrightarrow} |H,v_\ell\rangle \end{aligned} \tag{4.9}$$

where $|a_\ell\rangle$ and $|d_\ell\rangle$ are the OAM states equivalent to the antidiagonal and diagonal polarization states. The final transformation $|d_\ell\rangle \rightarrow |v_\ell\rangle$ and $|a_\ell\rangle \rightarrow |h_\ell\rangle$ to return back into the initial basis is done by a second DP rotated at angle $\pi/8\ell$, placed beyond the PSI. The use of the PSI as a polarization c-NOT gate in the photon polarization-path space was already reported [48].

Bell's states measurements. A well known theorem forbids deterministic and 100% efficient detection of all the four Bell's states of a photon pair with a process that involves just linear optics. Up to now, the experimental realization of the Bell's states detection involves additional degrees of freedom, higher order entanglement, or give probabilistic result with non-unit fidelity. The situation is different in the case of single-particle entanglement, where such measurement is possible. The PSI with a DP oriented at angle $\pi/8\ell$ realizes an unitary optical gate which transforms each one of the four Bell states

$$\begin{aligned} |B_1\rangle &= (|H,h_\ell\rangle + |V,v_\ell\rangle)/\sqrt{2} \\ |B_2\rangle &= (|H,h_\ell\rangle - |V,v_\ell\rangle)/\sqrt{2} \\ |B_3\rangle &= (|H,v_\ell\rangle + |V,h_\ell\rangle)/\sqrt{2} \\ |B_4\rangle &= (|H,v_\ell\rangle - |V,h_\ell\rangle)/\sqrt{2} \end{aligned} \tag{4.10}$$

into the not entangled spinorbit basis $|H,h_\ell\rangle$, $|V,v_\ell\rangle$, $|V,h_\ell\rangle$ and $|H,v_\ell\rangle$. The last states can be analyzed with standard techniques to measure

the photon SAM and the OAM separately. The Bell state analysis gate can be realized by mounting the PSI as a polarization c-NOT gate, as described in the previous section, to obtain $|B_1\rangle \rightarrow |A, v_\ell\rangle, |B_2\rangle \rightarrow |D, v_\ell\rangle, |B_3\rangle \rightarrow |A, h_\ell\rangle, |B_4\rangle \rightarrow |D, h_\ell\rangle$. Finally, an half wave plate at 22.5° can be used to rotate the photon polarization back into the horizontal plane.

Schmidt state generation. It is well known that any two-qubit state, as the photon spinorbit state, can be put into the general Schmidt form

$$|\Psi_S\rangle = \cos(\theta)|H, h_\ell\rangle - \sin(\theta)|V, v_\ell\rangle \tag{4.11}$$

by means of unitary transformations acting on each degree of freedom separately. Conversely, given the state (4.11), any spinorbit state can be obtained by applying separate unitary transformations to the SAM and OAM degrees of freedom. The degree of entanglement of the state (4.11) is parametrized by the angle θ. The non-maximally entangled state (4.11) could be used, for example, to demonstrate the Hardy paradox [57] – a test of the quantum nature of the entanglement and a proof of contextuality (or in the case of two-particles – non-locality) of quantum mechanics.

To test our PSI we performed an experimental demonstration, realizing some of the applications proposed above. Since quantum optics experiments that involve single-photon entanglement can be simulated using coherent CW laser source, to test experimentally our PSI scheme we used a c.w. vertically polarized 532-nm TEM_{00} single frequency laser beam. To generate beams carrying non-zero OAM, we used a q-plate with unit topological charge. In our experiments the optical retardation δ of the q-plate was changed by thermal tuning. As it was shown in Sec. 4.1, a combination of a tuned q-plate and a linear polarizer, can generate any qubit in the $\ell = \pm 2$ OAM Hilbert subspace starting from an elliptically polarized TEM_{00}, according to

$$\alpha|L, 0\rangle + \beta|R, 0\rangle \longrightarrow \frac{1}{\sqrt{2}}|H\rangle(\alpha|2\rangle + \beta|-2\rangle) \tag{4.12}$$

where a polarizer after the q-plate was used to select the H polarization. The insertion of the polarizer reduces the conversion efficiency upper limit to 50% of the incident photons. The STOC process is reversible and allows the transfer back any OAM qubit into a corresponding polarization qubit according to [45]

$$\alpha|H, 2\rangle + \beta|H, -2\rangle \longrightarrow \frac{1}{\sqrt{2}}(\alpha|L, 0\rangle + \beta|R, 0\rangle). \tag{4.13}$$

The inverse STOC process is very useful in the detection stage, because

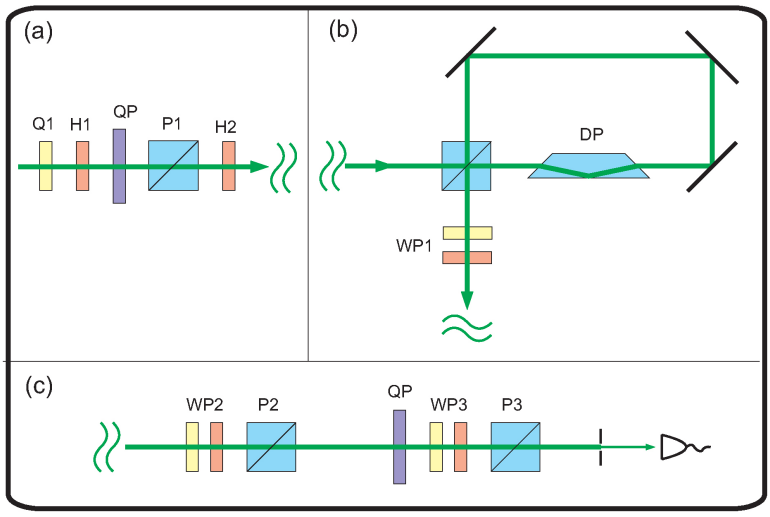

Figure 4.6: The experimental setup. (a) a QP with a set of optical components eventually placed or removed for creating the input states for each experimental demonstration, (b) the Polarizing Sagnac interferometer with a Dove prism, (c) detection system used to analyze the polarization and OAM state of the outgoing beam.

the information encoded in the OAM degree of freedom is transferred back in the light polarization, which is very easy to be analyzed. Our experimental setup is shown in Fig. 4.6 and is made of three stages. In the first stage, the OAM states are generated by a QP, placed after a set of quarter-wave plate $Q1$, half-wave plates $H1$ and $H2$ and polarizer $P1$, as shown in Fig. 4.6(a). Some of the optical components were removed or inserted back, depending on the desired photon state. The second stage was the PSI with the Dove prism inside, as shown in Fig. 4.6(b). A set of waveplates ($WP1$) was inserted at the PSI exit to compensate for eventual phase shifts and polarization changes introduced by the DP and mirrors as also to change the output polarization basis, when needed, to $|H\rangle, |V\rangle$. The third stage was for polarization and OAM analysis and is shown in Fig. 4.6(c). The photon state coming form the PSI was first analyzed in polarization by the waveplates $WP2$ and PBS $P2$ and then a second QP was used to transfer the OAM state into the corresponding polarization state of TEM_{00} mode (Eq. (4.13)), which was subsequently analyzed by waveplate $WP3$ and polarizer $P3$. The TEM_{00} mode in the output beam was selected by a spatial filter made by microscope objective and pinhole (not shown in the figure). The average transmittance of the PSI was 80%, mostly because of scattering and reflection losses from the optical components (no antireflection coating was used). In evaluating the efficiencies of the PSI processing in the spin-orbit space, we corrected for these losses. We performed several experiments

to test the different operations of the PSI.

In the first experiment, we used the PSI to clean up the TEM_{00} mode from the input beam. The input light was circularly polarized and sent into a QP. The optical retardation δ of the QP was changed so to obtain a mixture of $\ell = 0$ and $\ell = 2$ OAM eigenstates, according to Eq. (3.4). The polarizer $P1$ ensured antidiagonal polarization at the PSI input and the DP was rotated at $\alpha = \pi/8$. Figure 4.7 shows the data for the case $\ell = 2$. The $\ell = 2$ and $\ell = 0$ modes, shown in the figure, exit from the opposite ports of PBS $P2$ in Fig. 4.6(c). The measured contrast ratio of our cleaner was about 3.5:100.

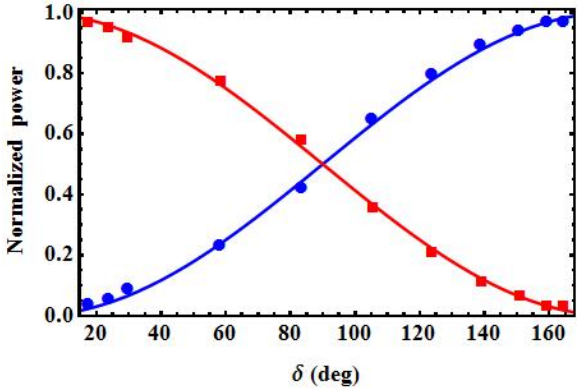

Figure 4.7: Filtering the TEM_{00} mode from the OAM carrying beam. Dots ($\ell = 2$) and squares ($\ell = 0$) represent the normalized intensities of the two exits of the final PBS $P2$ in Fig. 4.6(c), as functions of the QP optical retardation δ. The solid curve is the fit with $\sin^2 \delta/2$ and $\cos^2 \delta/2$ behavior expected from Eq. (3.4). The experiment was repeated for $\ell = -2$ with similar results.

In the second experiment, we used the PSI to separate opposite OAM eigenstates. The input state was created by sending the H-polarized laser light into a HWP at angle $\theta/2$, a QWP at 45° and finally into a QP tuned for optimal STOC, so to obtain beyond the polarizer $P1$ of Fig. 4.6 the OAM qubit $|\Phi\rangle = \cos 2\theta|+2\rangle - \sin 2\theta|-2\rangle)$ with antidiagonal polarization. After the QP tuning, the residual $\ell = 0$ component was negligible (less 1%). The OAM qubit superposition was changed by rotating the half-wave plate. The DP in the PSI was set at $\alpha = \pi/16$. The experimental results are shown in Fig. 4.8. The contrast ratio was 4.2:100 and the transmission efficiency larger than 90%, much larger than what can be obtained by holograms and spatial filter combination.

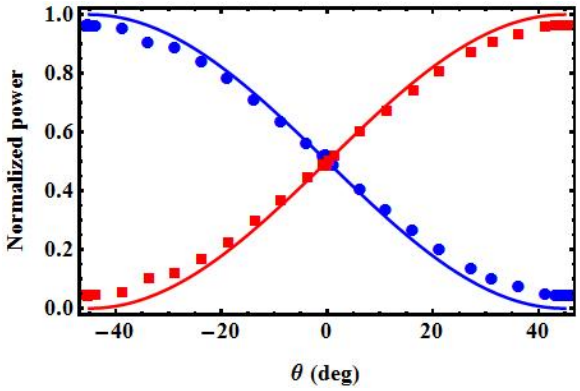

Figure 4.8: Sorting of the OAM eigenstates $|\pm 2\rangle$. Dots ($\ell = 2$) and squares ($\ell = -2$) represent normalized intensities of the two exits of the final PBS in Fig. 4.6(c), as functions of the angle θ of the half-wave plate, that controls the state of the input beam. The solid line is given by $\sin^2(\theta - \pi/4)$ and $\cos^2(\theta - \pi/4)$, according to theory.

In the third experiment, we implemented Bell's states detection with the PSI. The states (4.10) can be generated with a QP with 100% efficiency. The states $|B_1\rangle$ and $|B_4\rangle$ are generated directly by sending in in the QP a H and V-polarized TEM_{00} beam, respectively. The states $|B_3\rangle$ and $|B_2\rangle$ require an additional HWP at 45° beyond the QP, so to exchange the polarization states. The states (4.10) were disentangled by the PSI c-NOT operation described above with DP rotated at $\alpha = \pi/16$. The output base states $|H, h_2\rangle$, $|H, v_2\rangle$, $|V, h_2\rangle$ and $|V, v_2\rangle$ were analyzed in polarization and OAM separately by sending them into the four output channels of a setup formed by PBS and QPs for inverse STOC. The average contrast ratio in separating the $|h_2\rangle$ and $|v_2\rangle$ OAM state by the inverse STOC was 1.4:100. The intensities of the signals at each one of the four exit gates of our analysis setup are shown in Fig. 4.9. At least 94% of the intensity was concentrated in one exit gate at once, showing very good disentanglement by the c-NOT PSI operation.

In our final experiment, we used the PSI to create the photon spinorbit Schmidt state (4.11). Although some photon spinorbit states of the Schmidt form can be generated by simply sending through a QP an elliptically polarized TEM_{00} beam, this is not true for the state (4.11). This is because some unitary operations, as $\pi/2$-conversion, for example, are difficult to be implemented in the OAM subspace and require cylindrical lens converters (the Dove prism performs a π-conversion). Our PSI can do the OAM state $\pi/2$-conversion [49] and, hence, it can be exploited to create states as (4.11). In our experiment, we first turned the laser beam polarization into diagonal and then sent it through the QP and PBS to obtain with 50% nominal efficiency

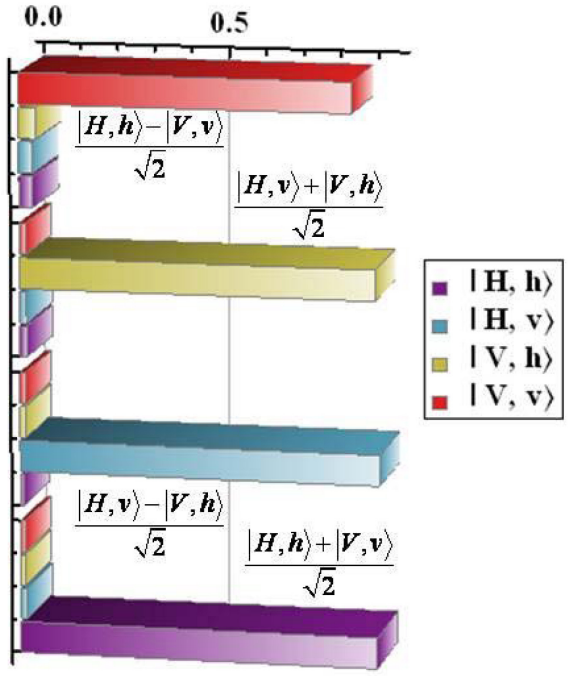

Figure 4.9: Bell's state detection. The photons coming from the PSI were first sorted by a PBS into their H and V polarizations and then sorted again by a QPs in each channel so to send the OAM h and v states into orthogonal polarizations by inverse STOC.

the state $|H, d_\ell\rangle$, with $\ell = 2$, in our case. The state $|H, d_\ell\rangle$ was then made to pass through a HWP at angle θ and sent directly into the PSI with Dove prism at $\alpha = \pi/8\ell = \pi/16$. A straightforward calculations shows that the photon spinorbit state at the PSI exit is precisely the Schmidt state (4.11) with θ replaced by 2θ. The degree of entanglement of this spinorbit state is controlled by rotating the HWP. We measured the intensity the $|H, h_2\rangle$ and $|V, v_2\rangle$ components of the Schmidt state generated by the PSI with the same apparatus used for the SAM and OAM analysis in the previous experiment on Bell states. The results are reported in Fig. 4.10. For the sake of completeness we measured by full spinorbit tomography the density matrix of one of the states with maximal spinorbit entanglement. The tomographic technique is commonly used in single photon quantum optics to measure qubits [58] and can be used also to characterize OAM photon states or even spinorbit photon states [22, 49, 59]. The main advantage of tomography is that both the amplitude and phase of the optical field can be retrieved without having recourse to interferometers. The basic idea is to measure the Stokes parameters $s_i (i = 1, ..., 3)$ by intensity differences in the horizontal/vertical basis and in the antidiagonal/digonal basis for the polarization

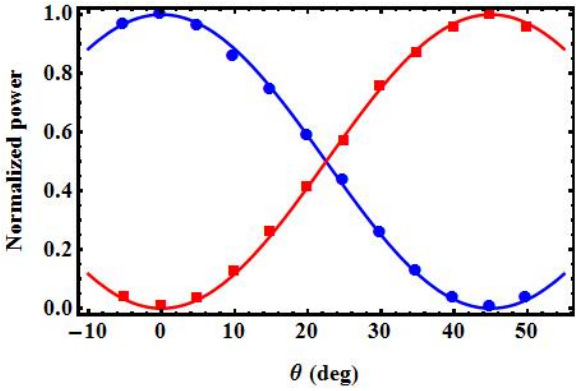

Figure 4.10: Normalized intensities, corresponding to the $|H, h_2\rangle$ (dots) and $|V, v_2\rangle$ (squares) component of the state (4.11) as functions of the angle θ of the HWP. Solid lines correspond to $\cos^2(2\theta)$.

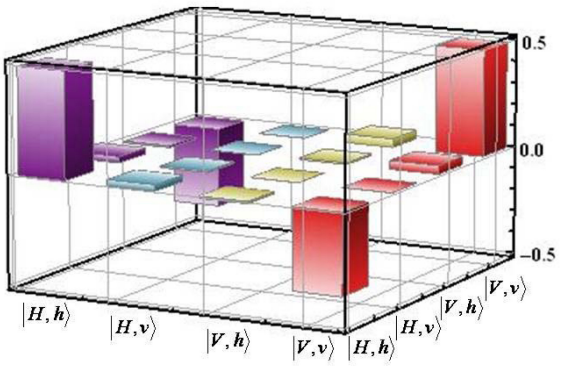

Figure 4.11: Density matrix of the near-maximally entangles Schmidt state, reconstructed via full spinorbit tomography

qubit and in similar bases for the OAM qubit [58]. In our measurements the tomography was carried out by using PBS and QPs with pinhole for inverse STOC as in the previous experiments. The results are shown in Fig. 4.11 and are in excellent agreement with theory. The measured average fidelity defined as the squared scalar product of the observed spinorbit state and the expected state (4.11) was 92%.

4.3 Generation and control of different order orbital angular momentum states by single q-plate [60]

A proposal for the use of OAM as the alphabet for the free space communication was already made in 2004 by Gibson et al. [6]. OAM, comparing to the polarization has a number of advantages, it is more stable under propagation and insensitive to the anisotropy of the medium, it is more secure since it is difficult to intercept the information carried by the OAM unnoticed. One of the main advantages is the multidimensionality of the OAM degree of freedom that allows to encode much more information into single photon. In the quantum regime, such high-order qubits, and their use for quantum information purposes has been shown to have several possible advantages. Photonic qudits have been so far mainly implemented using multi-photon systems or multi-path encoding and the alternative of using OAM encoding has been investigated only very recently. Up to now, single-photon OAM qudits with dimension $d = 3$ ("qutrits") and $d = 4$ ("ququarts") have been generated and employed, e.g., in quantum communication, quantum bit commitment, and quantum key distribution [61, 62, 63, 64]. Combined SAM-OAM ququarts have been also recently demonstrated [65]. However, the difficulty and low efficiency of OAM manipulation has so far represented a serious limitation. In particular, current sources of optical OAM are either very rigid (only one OAM value is generated, with no switching or modulation capability) or very inefficient (typically less than 40% of the input photons is converted into the desired OAM modes) and fairly expensive; electro-optical fast manipulation of OAM is virtually non-existent, while the OAM control flexibility currently provided by spatial light modulators (SLM) comes at the expense of a slow response ($\sim$ 1 kHz) and a high cost.

In this work, a fast, reliable, and inexpensive q-plate-based device to encode classical (or quantum) information into different OAM states of a light beam was proposed. The polarization controlled mechanism of the q-plate allows to realize OAM switching by electro-optical devices, thus ensuring very fast commutation rates (up to $\sim$ GHz rates). The beam polarization state is not affected and can be further manipulated to store more information. If also the SAM is considered, our device may encode three classical (or quantum qu-) bits of information into a single photon. In our device, the q-plate is inserted into a triangular optical loop, as shown in Fig. 4.12. A polarizing beam-splitter (PBS) is used as the input and output gate, so that only the horizontally polarized light can enter and exit from the loop, the vertically polarized light being directly reflected by the PBS. The tuned q-plate was sandwiched between two quarter wave plates (QWPs) and inserted in the loop, as shown in Fig. 4.12. As it will be shown below, our loop device can

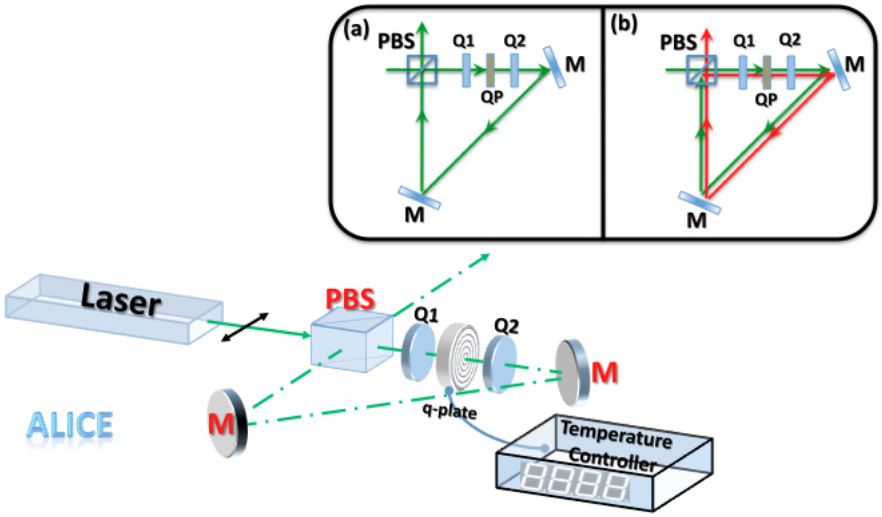

Figure 4.12: The q-plate sandwiched between two QWPs (Q_1 and Q_2) inserted in the triangular optical loop. The beam trajectory inside the loop device for the case of $(45°, 45°)$, $(-45°, -45°)$ where the beam passes once (inset a), and $(-45°, 45°)$ and $(45°, -45°)$ where the beam passes twice inside the cavity (inset b). The solid green and red lines show the first and second trip, respectively. Legend: M-mirror, PBS-polarizing beam splitter, Q-quarter wave plate, QP-q-plate.

1. generate the four OAM eigenstates $|\pm 2\rangle, |\pm 4\rangle$; the switch among these four states is made acting on the light polarization so that very fast commutation rate can be achieved;

2. generate qubits formed by any pair sorted from the four OAM eigenstates above; the relative amplitudes of the two states forming the qubit is controlled by acting on the light polarization only;

3. generate a state made of the superposition of all OAM eigenstates with even ℓ; the power spectrum of the superposition is controlled by acting on the light polarization only.

Let us consider a TEM_{00} laser beam with OAM $\ell = 0$ entering in the optical loop. The output beam is a pure state of order $|\ell| = 2, 4$ when the QWPs in the loop are set at $\pm 45°$. Let us consider, for example, the case where the two QWPs were set at $45°$. The first QWP changes the polarization of the beam circulating in the loop from the horizontal ($|H\rangle$) to the left circular ($|L\rangle$). The q-plate coherently transfers Spin-to-OAM, switches the polarization into the right circular ($|R\rangle$) and provides the beam with an OAM value $\ell = +2$. The second QWP switches back the right-circular polarization into the horizontal one ($|H\rangle$), so that the light was led out from

the loop. Because of the even number of reflections by mirrors, the OAM of the output beam is left to $\ell = +2$. The full sequence of changes of the photon state is

$$|H,0\rangle \overset{Q_1^{@45^\circ}}{\longrightarrow} |L,0\rangle \overset{QP}{\longrightarrow} |R,2\rangle \overset{Q_2^{@45^\circ}}{\longrightarrow} |H,2\rangle \tag{4.14}$$

The same process occurs with the two QWPs set at -45°. In this case, however, the output beam is left with $\ell = -2$. The full sequence is

$$|H,0\rangle \overset{Q_1^{@-45^\circ}}{\longrightarrow} |R,0\rangle \overset{QP}{\longrightarrow} |L,-2\rangle \overset{Q_2^{@-45^\circ}}{\longrightarrow} |H,-2\rangle \tag{4.15}$$

Figure 4.12-(a) shows the ray trajectory inside the optical loop for these two cases.

When the two QWPs are set at opposite angles $(45^\circ, -45^\circ)$ or $(-45^\circ, 45^\circ)$, the output beam is left with $\ell = \pm 4$, respectively. Let us consider, for example, the case where the first QWP is set at $+45^\circ$ and the second at -45°, respectively. The horizontal polarized beam circulating in the optical loop is changed into the left-circular polarization by the first QWP. The q-plate, then, coherently transfers the spin into OAM and the state changes into $|R,2\rangle$. The second QWP switches back the polarization into the vertical polarization state, so that the beam is reflected back into the loop by the PBS. However, the sign of the OAM changes due to the odd number of reflections by mirrors and PBS. In the second trip, the first QWP changes the vertical polarization into the right-circular polarization and the q-plate transfers the polarization state into the left-circular polarization and subtracts 2 to the the beam OAM leading to $\ell = -4$. After that, the second QWP changes back the left-circular polarization into the horizontal polarization so that the beam with $\ell = -4$ can leave the loop after an even number of reflections by mirrors and PBS. For the $(-45^\circ, 45^\circ)$ configuration the same process takes place, but the sign of the output OAM is reversed. Inset (b) in Fig. 4.12-(b) shows the ray trajectory inside the optical loop for the last two cases. The full sequences of changes of the photon states are (M represents here the two mirrors)

$$\begin{aligned} |H,0\rangle &\overset{Q_1^{@45^\circ}}{\longrightarrow} |L,0\rangle \overset{QP}{\longrightarrow} |R,2\rangle \overset{Q_2^{@-45^\circ}}{\longrightarrow} |V,2\rangle \overset{M+PBS}{\longrightarrow} \\ &\quad |V,-2\rangle \overset{Q_1^{@45^\circ}}{\longrightarrow} |R,-2\rangle \overset{QP}{\longrightarrow} |L,-4\rangle \overset{Q_2^{@-45^\circ}}{\longrightarrow} |H,-4\rangle \\ |H,0\rangle &\overset{Q_1^{@-45^\circ}}{\longrightarrow} |R,0\rangle \overset{QP}{\longrightarrow} |L,-2\rangle \overset{Q_2^{@-45^\circ}}{\longrightarrow} |V,-2\rangle \overset{M+PBS}{\longrightarrow} \\ &\quad |V,2\rangle \overset{Q_1^{@45^\circ}}{\longrightarrow} |L,2\rangle \overset{QP}{\longrightarrow} |R,4\rangle \overset{Q_2^{@-45^\circ}}{\longrightarrow} |H,4\rangle \end{aligned} \tag{4.16}$$

Therefore, the loop device is able to generate -4,-2,$+2$,$+4$ values of OAM by choosing the proper angles for the two QWPs. Table (4.1) shows

the four possible combinations of QWP angles and the corresponding OAM values of the output beam [2]. One may replace the QWP with electro-

Table 4.1: Four possible combinations of QWP angles and their corresponding beam's OAM values.

Logical bit	Q_1	Q_2	OAM
00	$+45°$	$+45°$	$+2$
01	$-45°$	$-45°$	-2
10	$+45°$	$-45°$	-4
11	$-45°$	$+45°$	$+4$

optical devices so to encode the information in the light beam with rate of the order of several megahertz. The optical loop setup proposed in this work can be used for classical communications in 8D SAM-OAM space. As we it was already mentioned, an additional classical bit can be encoded in the SAM of the output beam by inserting a further QWP at the exit of the optical loop. So, Alice can transmit to Bob the eight spinorbit photon states $(|L\rangle, |R\rangle)\otimes(|-4\rangle, |-2\rangle, |+2\rangle, |+4\rangle)$, corresponding to three bit of information per photon. Bob can use, for example, a QWP at 45° followed by a PBS to select the SAM state of the received photons and the holograms shown in Fig. (4.13) to discriminate the photon OAM [6]. The communication transmitter and receiver scheme shown in Fig. (4.13) can be fully realized by the available technology. Its main advantage is that three bits are encoded in each photon manipulating only the polarization degree of freedom, which can be achieved by very fast and efficient electro-optical switching. Because of the presence of the hologram in the detection stage the overall efficiency is low. However, it can be significantly increased by using a siutable fish-eye device as recently proposed [66]. Our apparatus has been intended for classical telecommunication, but it can be applied for single photon quantum communication too, since the q-plate can act as a quantum device (see chapter 5).

When the orientation angles of the QWPs are set to values different from those reported in Table (4.1), a superposition of OAM states is generated, in general. In this case, the light is trapped inside the cavity making infinite number of loops. The output state is then given by a superposition of different OAM eigenstates made by the portions of horizontally polarized light exiting the cavity at each loop. In the quantum regime, the superposition is among the probability amplitudes α_N that the photon exits the optical loop after N round trips. When the angle of one of the QWPs inside the

[2]Because we were only interested to the OAM value of the beam, we have neglected the phase delay between the first and second trip inside the optical loop. Indeed, the beam with OAM value $|\ell| = 4$ has a trip delay with respect to the beam with OAM value $|\ell| = 2$.

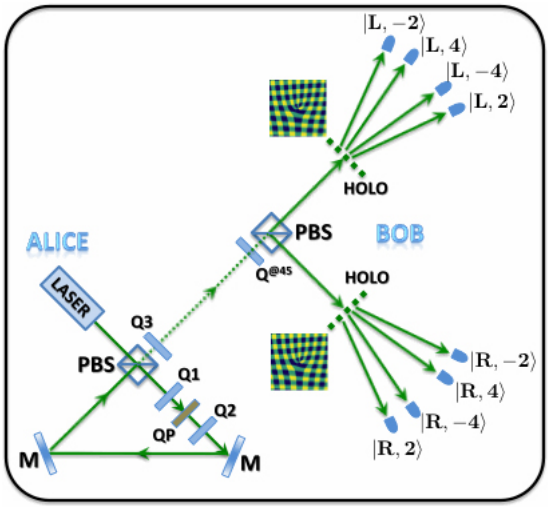

Figure 4.13: Alice apparatus is similar to what has already shown in figure (4.12). In order to encode another information bit, a third QWP (Q_3) is located at the exit face of the optical loop. Alice is able to generate ($|L,-4\rangle, |L,-2\rangle, |L,+2\rangle, |L,+4\rangle, |R,-4\rangle, |R,-2\rangle, |R,+2\rangle$ and $|R,+4\rangle$) by setting her QWPs at $\pm 45°$. Bob measures the photon SAM state by suitable QWP and a PBS and measures the photon OAM state by suitable holograms, as shown.

cavity is fixed at 45° (or −45°), four different qubits are produced made of any two of the four OAM states $|\pm 2\rangle, |\pm 4\rangle$.
More precisely, if the first (second) QWP is fixed at angle 45° the generated output state up to a global phase factor is given by

$$|\psi_1\rangle = C_1(\theta,\psi)[2(\cos(2\theta+\psi)-\sin\psi)|2\rangle - i(1-\sin 2\theta)|\mp 4\rangle] \qquad (4.17)$$

where $C_1(\theta,\psi)$ is a normalization factor depending on the round trip phase delay δ and on the orientation angle θ of the free QWP.
If the first (second) QWP is fixed at −45°, instead, the output state is given by

$$|\psi_2\rangle = C_2(\theta,\psi)[2(\cos(2\theta-\psi)-\sin\psi)|-2\rangle - i(1+\sin 2\theta)|\pm 4\rangle] \qquad (4.18)$$

where $C_2(\theta,\psi)$ is a new normalization factor. It is worth noting that the relative phase of the two OAM eigenstates forming the qubit is fixed to be ±90°, so that only the relative amplitude can be changed by the control parameters θ and ψ. The possibility of exploiting the photon polarization to control qubits formed by two OAM eigenstates with different m may be useful for quantum computing or other quantum applications.

When both the angles of the QWPs are different from ±45°, a complex superposition of even OAM eigenstates is generated, having the general form

$\sum_{n=-\infty}^{+\infty} c_{2n}|2n\rangle$, where c_{2n} depend on the angles θ_1 and θ_2 of the two QWPs and on the loop delay ψ. Figure 4.14 shows some examples of infinite OAM state superposition obtained for different orientations θ_1 and θ_2 of the two QWPs and for $\psi = 0$. Notice how the symmetry of the OAM power spectrum of the output beam is strongly affected by θ_1 and θ_2. The odd OAM components are missing because a $q = 1$ q-plate was used. A full OAM spectrum can be generated by using a $q = 1/2$ q-plate. The possibility of exploiting the light polarization to control full spectra of OAM eigenstates may be useful for future, yet not identified, applications. In our first exper-

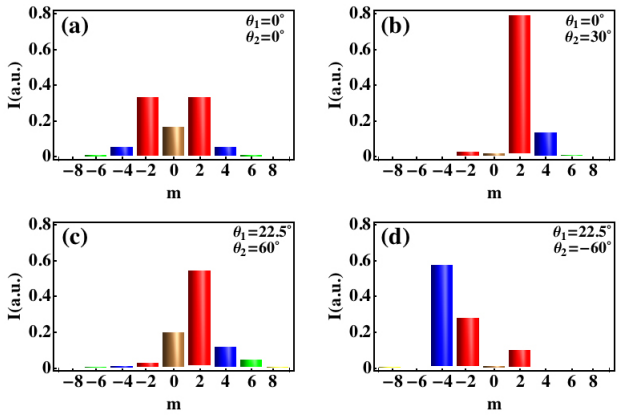

Figure 4.14: Calculated OAM power spectrum $I_n = |c_{2n}|^2$ of the beam emerging form the loop device for different angles θ_1 and θ_2 of the two QWPs for loop delay $\psi = 0$. The power spectrum can be either symmetric (a) or not symmetric (b,c,d) and the fundamental $\ell = 0$ component can be suppressed (b,d).

iment, we used a c.w. TEM_{00} laser source at $\lambda = 532$ nm and measured the output beam phase-front by making an interference with a plane-like phase-front of same frequency. We used an azimuthally oriented liquid crystal q-plate. The optical retardation of the q-plate was tuned by temperature controller [33] in such a way that it acted as a half-wave plate ($\delta = \pi$). Figure (4.15) shows the recorded interference pattern of the beam exiting the optical loop for different angles of the QWPs. The absolute value of the OAM is deduced from the number of prongs of the interference fork and the sign from the prongs up or down direction. In our second experiment, we fixed the first QWP at 45° and rotated the second one so to generate the qubit formed by the OAM eigenstates 2 and -4 as described before. The alignment of the loop were adjusted by moving the two mirrors so to obtain a good symmetric interference pattern [3]. For each angle θ of the second QWP, we measured the power flow associated to the $\ell = 2$ and $\ell = -4$ com-

[3] This pattern has the characteristic form of six-petal flower.

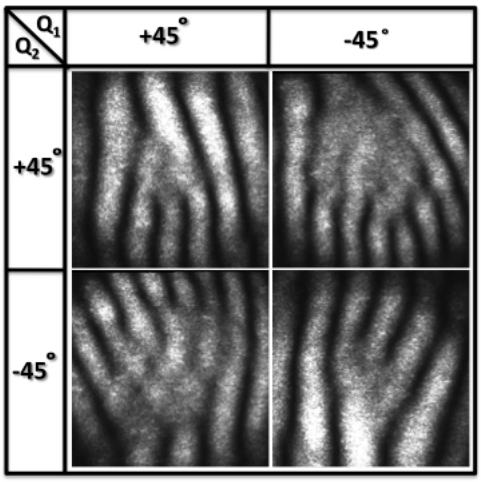

Figure 4.15: The interference of the output beam from the loop device and TEM_{00} beam for the four QWP angles shown in Table (4.1).

ponents of the beam exiting the loop device by suitable computer generated fork holograms displayed onto a Spatial Light Modulator (SLM). Beyond the hologram, the $\ell = 0$ component was selected by a pinhole posed in the focal plane of a convergent lens. Finally, the measured power flows were normalized so that their summation returned one. The result is shown in Fig. 4.16. The full curve is from Eq. (4.18). To fit the data we used the loop retardation ψ as best fit parameter.

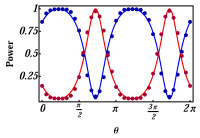

Figure 4.16: The normalized powers of the $\ell = 2$ (blue) and $m = -4$ (red) components of the loop output beam as functions of the orientation angle θ of the second QWP. The first QWP was held fixed at 45°. The continuous curve is the fit to Eq. (4.17). The optical retardation ψ of the loop was used as fitting parameter. In the case of the figure above we found a best fit value $\psi = 0$.

Chapter 5

Quantum Optics applications

5.1 Introduction

One of the most promising fields where the OAM can be applied is quantum optics. Since the first demonstration of the quantum nature of the OAM [8], a particular attention was drawn towards OAM degree of freedom. Photons by themselves showed to be good candidate for the realization of quantum information algorithms and up to now the photon polarization (SAM) degree of freedom is widely used as an implementation of the qubit - a basic information unit, thanks to easy methods of manipulation of the polarization of a photon and relatively easy methods of generation of single photons and photon pairs. OAM degree of freedom provides a different approach to quantum information. First of all, OAM is an additional Hilbert space that can be used parallel to the spin space. This allows to increase the amount of information carried by a single photon, by using two different space at the same time with a qubit, encoded into each degree of freedom or create entangled states, where one degree of freedom is entangled with the other, of the same particle. The multidimensionality of the OAM space, on the other side, allows to create information units called "qudits" – quantum systems with dimensions higher than two. Particular examples of qudits are tree-level "qutrits" or four-level "ququarts". This allows to encode more quantum information into a single degree of freedom, or to create photon pairs where qudits are entangled.

It was already demonstrated, that a q-plate can act in the photon count regime, where not a classical coherent beam is used as input, but single photons. A series of experiments were performed in collaboration with the group of Francesco De Martini, from the University of Rome "La Sapienza", where the q-plate was tested for the first time in the quantum optics and then exploited to realize some novel experiments that were never done in the OAM degree of freedom of the photons, or in the entangled spinorbit space of single photons.

The action of the q-plate on a single photon is basically the same as in the classical regime, however in the quantum mechanics framework this process must be observed from the different point of view. For example, when a horizontally polarized photon interacts with the q-plate, the final state is

$$\hat{QP}|H\rangle \rightarrow \frac{1}{\sqrt{2}}(|R, 2q\rangle + |L, -2q\rangle) \tag{5.1}$$

which is a non-separable single photon state with entangled SAM and OAM degrees of freedom. While this significant result was achieved by simply putting a q-plate on the way of a beam, further applications of the q-plates are numerous. The polarization control of the OAM generation process (see section 4.1) was also demonstrated in the single-photon regime [45] and was exploited to transfer the information encoded in a qubit of one Hilbert space into the other. With a q-plate of topological charge $q = 1$ this transfer was done as from SAM to OAM subspace of $|\ell| = 2$ and vice versa, and, by cascading the q-plates, to the subspaces of order $|\ell| = 4$ [50]. Exploiting the q-plate it was possible to demonstrate of the Hong-Ou-Mandel effect in the OAM, a milestone quantum optics experiment, made in 1987 for the polarization degree of freedom which describes the basic photon-photon interaction inside a beamsplitter. If two photons enter the symmetric $50\% - 50\%$ beamslpitter they tend to exit from the same side, when they are indistinguishable. Two labeled (either by a time delay, or by any other method) photons will have equal and independent probability of exiting from any side. A straightforward consequence is that if the two photons are indistinguishable, they will never exit the two sides separately. Afterwards, a cloning of the OAM photon state was done for the first time [67]. While the cloning of a quantum state with the preservation of the original one is forbidden by a no-cloning theorem, an imperfect cloning is still allowed. The "imperfection" consists in a less than one fidelity of the cloned state, or in other words, a less than unit probability of the successful creation of the exact copy. The cloning with the maximum allowed fidelity is called "optimal". Using the symmetrization technique that is based on the Hong-Ou-Mandel effect, such optimal cloning of the 2D OAM states was realized experimentally. From the spinorbit side, a thorough study of the q-plate ability to generate 4D ququart states of the single photon was also demonstrated [59]. After that, an optimal cloning of these 4D states was done. As in the case of the OAM 2D states the symmetrization technique was used for this purpose [65], however, the q-plates were the core devices, that allowed to generate the necessary states, realize the cloning procedure and detect the results.

In this chapter, I present some other approaches to the q-plate application to quantum optics. The first one is a proposal of an adjustable device, called Universal Unitary Gate, that can realize any unitary operation in the 4D spinorbit space of a single photon. Being a device mainly based on the

q-plates it does not require any interferometric setups and allows to manipulate the state of a photon without changing its propagation direction, with all the state changes done along one beam.

Another section of the chapter deals with a more fundamental aspects of quantum mechanics, not strictly related to computation and cryptography and devoted to demonstrate the non-local and contextual nature of quantum mechanics by Bell's inequalities violation. In these experiments we used entangled SAM + OAM states, prepared in three different ways: a single photon entanglement of the two Hilbert spaces of the same particle, a "hybrid" entanglement, where the OAM degree of freedom of one photon is entangled with the SAM degree of freedom of the other and a classical analog of the single photon entanglement, performed not with single photons, but with a continuous coherent laser beam. This work was performed in a joint collaboration with the research group from University of Glasgow, Glasgow, Scotland, United Kingdom, lead by Prof. Miles Padgett.

5.2 Universal unitary gate [68]

A proposal for a q-plate, as device able not only to generate, but also manipulate the states in 4D spinorbit space was also made. An advantage of the entanglement, where two Hilbert spaces of the same particle are entangled, compared to the standard two-photon entanglement is a possibility of realization of unitary gates – a quantum devices that perform a certain unitary operation on the state. A universal unitary gate (UUG) in the polarization space, i.e. an adjustable gate that can realize any unitary operation on the polarization state of the photon is easily realizable by a set of wave plates. For example a cascade of quarter-wave plate, half-wave plate and another quarter-wave plate can perform any operation in the $SU(2)$ space. Adding an isotropic phase retarder,as shown in the inset of Fig. 5.1, for controlling the global phase will expand the action into the $U(2)$ space.

Changing the retardation δ of the isotropic plate and the optical axis angles α, β, γ of the three birefringent wave plates allows one to realize any unitary transformation $\widehat{V}_\pi(\alpha, \beta, \gamma, \delta) \in U(2)$ in the photon polarization space [69]. For example, Pauli's operator, $\hat{\sigma}_x$, $\hat{\sigma}_y$, and $\hat{\sigma}_z$, in the circular polarization basis of the spin space, may be realized by setting $(\alpha, \beta, \gamma, \delta) = (0, \pi, \pi/2, \pi/2) \rightarrow \hat{\sigma}_x$, $(\alpha, \beta, \gamma, \delta) = (0, \pi/4, 0, \pi/2) \rightarrow \hat{\sigma}_y$, $(\alpha, \beta, \gamma, \delta) = (0, -\pi/4, \pi/2, \pi/2) \rightarrow \hat{\sigma}_z$ (this choice is by no means unique). The action of the SAM-UUG is defined by its action on the circular polarization basis states according to

$$(|1_\pi, \ell_o\rangle, |-1_\pi, \ell_o\rangle) \xrightarrow{\widehat{V}_\pi} (|1_\pi, \ell_o\rangle, |-1_\pi, \ell_o\rangle)\mathcal{V}_\pi \tag{5.2}$$

where $\mathcal{V}_\pi$ is a 2×2 unitary matrix.

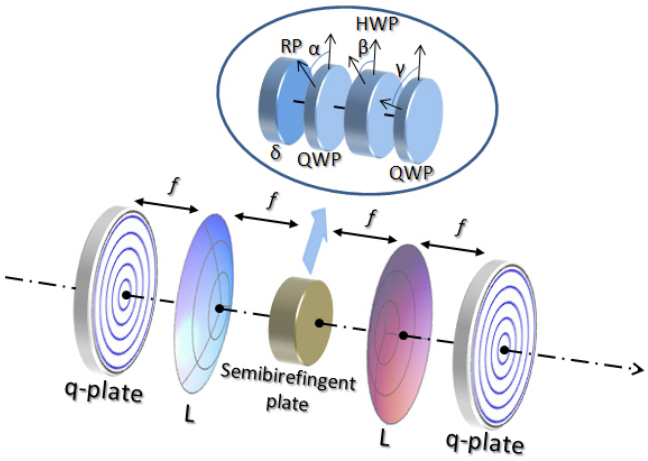

Figure 5.1: The scheme of the Q-box. The structure of the birefringent plate is shown in the inset. QWP, HWP, RP are the quarter-wave plate, half-wave plate and retardation plate respectively. α, β, γ indicate rotation of the QWP, HWP, QWP and δ is the retardation of the isotropic plate. The birefringent plate realizes a SAM-UUG affecting the OAM $\ell = 0$ part of the beam only and it is placed in the common focal plane of the two lenses (L). The topological charge of both q-plates is unit and the optical retardation is $\lambda/2$.

Some manipulations of the photon OAM can be made by using Dove prisms [70], transverse mode sorters [71], and cylindrical lens mode converters [72], but no UUG has been proposed for the photon OAM till now. However, even if such OAM-UUG were available, its use together with a SAM-UUG would still not reach the goal of a full manipulation of the ququart state encoded in the photon, because these two UUGs would act on the spin and OAM degrees of freedom separately and would not be able to handle two-qubit entangling. Entangled pairs of qubits, i.e., nonseparable ququarts, are central in most schemes that have been proposed for quantum communications, quantum information processing and secure key distribution. The SAM-OAM entangling ability of the q-plate allows us to introduce a UUG for spinorbit 4D Hilbert space, spanned by 2D SAM space and a 2D OAM space with $|2_o\rangle$ and $|-2_o\rangle$ basis states (all our results are easily generalized to an arbitrary $|\ell|$).

The basic element of our SO-UUG is the device, here named q-box (QB), that is shown in Fig. 5.1. The QB is made by cascading two QPs, the first for splitting the OAM $\ell = \pm 2$ components of the input beam into $\ell = 0$ and $\ell = \pm 4$ components, and the second to return them back into $\ell = \pm 2$ components. Between the two QPs, a SAM-UUG is inserted which performs an arbitrary unitary transformation $\widehat{V}_\pi(\alpha, \beta, \gamma, \delta)$ on the photon spin only,

and which acts selectively on the OAM $\ell = 0$ component of the beam, leaving the $\ell = \pm 4$ components unaffected. This is made possible, because the $\ell = 0$ and $\ell = \pm 4$ components of the beam, initially superimposed at the exit plane of the first QP, will spatially separate in their radial pattern by free propagation. In fact, the $\ell = 0$ part will become concentrated in a spot at the beam center, and the $\ell = \pm 4$ part will become distributed over a surrounding ring with zero intensity at center ("doughnut" beam shape).

An important issue that must be taken into account at this point is the transverse mode non-stationarity under free propagation, due to the beam radial profile arising at the output of devices like q-plates, fork holograms and other. In fact, we should have properly described our photon states by $|s_\pi, \ell\rangle|\varphi_\ell\rangle$, where $|\varphi_\ell\rangle$ is the radial state, whose evolution during propagation depends on the OAM eigenvalue ℓ. The transverse beam profile associated to the radial state $|\varphi_\ell\rangle$ is given by the radial function $\varphi_\ell(r) = \langle r|\varphi_\ell\rangle$, where $|r\rangle$ denotes the state of a photon localized at radial distance r from the optical axis. In general, the profile $\varphi_\ell(r)$ is a linear combination of infinite Laguerre-Gauss (LG) radial profiles $\mathrm{LG}_{p\ell}(r)$ with given ℓ and different radial numbers p. During free propagation, the Gouy phases of the different LG-mode components change relative to each other, so that the total radial profile $\varphi_\ell(r)$ resulting from the superposition is not stationary. In most quantum computation experiments, where OAM is not involved, the transverse profiles are ignored, since they are the same for every state and can be factorized out. As we shall see in a specific example, such factorization is not possible in our case and the profile change under free propagation will give rise to some transverse "cross-talk" between different ℓ-components of the beam reducing the fidelity of our SO-UUG.

Having a good separation between the $\ell = 0$ and the $\ell = \pm 4$ OAM components is crucial for obtaining an efficient SO-UUG. This can be obtained in several ways. In our work we considered a very simple sorting method, based on a semibirefringent circular mask posed at the back focal plane of the first lens shown in Fig. 5.1. The central part of the mask is a birefringent disk of radius R, while the surrounding corona is an isotropic medium. The central disk performs the required unitary transformation $\widehat{V}_\pi$ on the photon spin of the $\ell = 0$ component. The radius R of the active part of the semibirefringent plate can be adjusted to minimize the crosstalk among the transverse radial modes. The best spatial separation among radial modes occurs in the far field or, equivalently, at the back focal plane of the first lens in Fig. 5.1, where the Fourier transform of the field is collected. The second lens in Fig. 5.1 performs the inverse Fourier transform thus restoring the input beam transverse profile in the final output. To study the behavior of the QB in more detail, it is convenient to use the following logical states in the SO Hilbert space with OAM value $\ell = \pm 2$:

$$|00\rangle = |1_\pi, 2_o\rangle, \quad |01\rangle = |-1_\pi, -2_o\rangle$$

$$|10\rangle = |-1_\pi, 2_o\rangle, \;\; |11\rangle = |1_\pi, -2_o\rangle. \tag{5.3}$$

The action of any linear operator $\widehat{V}$ in the spinorbit space is given by its action on the basis states, according to

$$(|00\rangle, |01\rangle, |10\rangle, |11\rangle) \xrightarrow{\widehat{V}} (|00\rangle, |01\rangle, |10\rangle, |11\rangle)\mathcal{V} \tag{5.4}$$

where $\mathcal{V}$ is a 4×4 matrix. In particular, operators as $\widehat{V}_\pi$ acting only on the photon spin are mapped in spinorbit matrices having the general form

$$\mathcal{V}_\pi = \begin{pmatrix} v_{11} & 0 & v_{12} & 0 \\ 0 & v_{22} & 0 & v_{21} \\ v_{21} & 0 & v_{22} & 0 \\ 0 & v_{12} & 0 & v_{11} \end{pmatrix} \tag{5.5}$$

where v_{ij} are the entries of the 2×2 matrix $\mathcal{V}_\pi \in U(2)$ in Eq. (5.2). Similarly, operators $\widehat{U}$ acting in the OAM subspace only are mapped in spinorbit matrices having the general form

$$\mathcal{U} = \begin{pmatrix} u_{11} & 0 & 0 & u_{12} \\ 0 & u_{22} & u_{21} & 0 \\ 0 & u_{12} & u_{11} & 0 \\ u_{21} & 0 & 0 & u_{22} \end{pmatrix} \tag{5.6}$$

where u_{ij} are the entries of the 2×2 matrix $\mathcal{U} \in U(2)$. Assuming the first QP located in the front focal plane of the first lens of the QB, in the back focal plane we have the 2D-Fourier transform of the field exiting from the QP. The 2D-Fourier transform can be described by an operator $\widehat{J}_{|\ell|}$ acting only on the radial part of the state: viz. $\widehat{J}_{|\ell|}|s_\pi, \ell_o, \varphi_\ell\rangle = |s_\pi, \ell_o\rangle\widehat{J}_{|\ell|}|\varphi_\ell\rangle$. In the basis of the localized states $|r\rangle$ in the Fourier plane (lens back focal plane) the matrix elements of the operator $\widehat{J}_{|\ell|}$ are given by

$$\langle r'|\widehat{J}_{|\ell|}|r\rangle = \frac{1}{\lambda f} J_{|\ell|}\left(\frac{r'r}{\lambda f}\right) \tag{5.7}$$

where $J_{|\ell|}(x)$ are the Bessel functions of integer order $|\ell|$, λ is the wavelength and f is the lens focal length. The operators $\widehat{J}_{|\ell|}$ are hermitian and unitary, so that $\widehat{J}^2_{|\ell|} = 1$. The action of a semi-birefringent plate (SBP) with the birefringent disk of radius R with corresponding unitary spin operator $\widehat{V}_\pi$ is given by

$$\begin{aligned} &|s_\pi, m_o, \varphi_\ell\rangle \xrightarrow{\widehat{SBP}} \\ &\widehat{V}_\pi|s_\pi, m_o\rangle\widehat{U}(R)|\varphi_\ell\rangle + |s_\pi, m_o\rangle(\widehat{I} - \widehat{U}(R))|\varphi_\ell\rangle \end{aligned} \tag{5.8}$$

Where $\widehat{U}(R)$ is hermitian and idempotent operator that acts only on the radial profile state, selecting the portion of the beam at distance $r \leq R$

and $\widehat{I}$ is the identity operator. In the basis of the localized states $|r\rangle$ the operator $\widehat{U}(R)$ is represented by the Heaviside unit step function $\Theta(R-r)$ with diagonal matrix elements

$$\langle r'|\widehat{U}(R)|r\rangle = \Theta(R-r)\delta(r-r'). \tag{5.9}$$

The action of the QB on the logical basis states (5.3) can now be easily calculated

$$\begin{aligned}&(|00\rangle,|01\rangle,|10\rangle,|11\rangle)|\varphi_2\rangle \overset{\widehat{Q}_b}{\to} (|00\rangle,|01\rangle,|10\rangle,|11\rangle)\mathcal{Q}_b|\varphi_2\rangle + \\ &((v_{11}-1)|01\rangle + (v_{22}-1)|00\rangle + v_{12}|1_\pi,-6_o\rangle + v_{21}|-1_\pi,6_o\rangle)\widehat{J}_4\widehat{U}(R)\widehat{J}_4|\varphi_2\rangle + \\ &(|10\rangle,|11\rangle)(\mathcal{I}-\mathcal{V}_\pi)\widehat{J}_0(\widehat{I}-\widehat{U}(R))\widehat{J}_0|\varphi_\ell\rangle\end{aligned} \tag{5.10}$$

where v_{ij} are the entries of the 2×2 matrix $\mathcal{V}_\pi$ of the birefringent disk, $\mathcal{I}$ is the 2D-identity matrix and the $\mathcal{Q}_b$ is a 4×4 matrix given by

$$\mathcal{Q}_b(\mathcal{V}_\pi) = \begin{pmatrix} 1 & 0 & 0 & 0 \\ 0 & 1 & 0 & 0 \\ 0 & 0 & v_{11} & v_{12} \\ 0 & 0 & v_{21} & v_{22} \end{pmatrix} \tag{5.11}$$

The last two terms in the left side of Eq. (5.10) are the crosstalk terms that appear due to the small overlap of $\ell = 0$ and $\ell = \pm 4$ modes in the Fourier plane. The effects related to mode cross-talk will be discussed below in a specific example. For the moment, we define the *ideal* QB a QB where the transverse mode cross-talk is negligible. The action of an ideal QB is then given by

$$(|00\rangle,|01\rangle,|10\rangle,|11\rangle) \overset{\widehat{Q}_b}{\to} (|00\rangle,|01\rangle,|10\rangle,|11\rangle)\mathcal{Q}_b \tag{5.12}$$

The matrix $\mathcal{Q}_b$ in Eq. (5.11) has not the form of the matrices in Eqs. (5.5) and (5.6), showing that the QB acts on both the spin and OAM degree of freedom of the photon simultaneously, producing entangling. Because the matrix $\mathcal{V}_\pi$ of the semi-birefringent plate is unitary, it is evident from Eq. (5.11) that also $\mathcal{Q}_b$ is unitary and so is the action of the ideal QB. The main property of the QB is that although the first QP takes photons out of our initial SO logical space (5.3), the operator of the full ideal QB is well defined in this space, as shown by Eq. (5.12).

In this section, we show that the ideal QB defined by Eq. (5.12) can be used to make the required UUG in our SO space. The QB itself does not provide the most general unitary transformation of $U(4)$. We can see this just by considering that $\mathcal{Q}_b(\mathcal{V}_\pi)$ (as $\mathcal{V}_\pi$ itself) depends on four real parameters only, while the most general unitary operator $U_{so} \in U(4)$ has 16 free parameters. The UUG in the spinorbit space is therefore a device more complex than the QB. It is then remarkable that the sequence of

- an ideal QB $\mathcal{Q}_b(\mathcal{V}_2)$

- a quarter-wave plate at angle 0
- an ideal QB $\mathcal{Q}_b(\mathcal{V}_R)$
- a half-wave plate at angle 0
- an ideal QB $\mathcal{Q}_b(\mathcal{V}_L)$
- a quarter-wave plate at angle 0
- an ideal QB $\mathcal{Q}_b(\mathcal{V}_1)$

provides the required UUG in the SO Hilbert space. Here $\mathcal{V}_1, \mathcal{V}_R, \mathcal{V}_L, \mathcal{V}_2$ are the 2×2 unitary matrices characterizing the semi-birefringent plates inserted in each QB. We It is worth noting that all elements of the QB are transparent so that many of them can be cascaded along the beam direction maintaining optical losses at reasonable level. The SO-UUG described above has the proper number of free parameters and it is unitary. However, we should also demonstrate that it is universal, i.e. that *any* unitary matrix of $\mathcal{U}_{so} \in U(4)$ can be realized by the sequence above. The proof is based on the results by Englert et al. [73]. In fact, a straightforward calculation shows that the matrix $\mathcal{U}_{so}$ associated to our UUG has the block form

$$\mathcal{U}_{so} = \begin{pmatrix} \mathcal{S}_{LL} & \mathcal{S}_{LR} \\ \mathcal{S}_{RL} & \mathcal{S}_{RR} \end{pmatrix} \tag{5.13}$$

where the 2×2 blocks are given by

$$\begin{aligned} \mathcal{S}_{RR} &= \frac{1}{2}\mathcal{V}_2(\mathcal{V}_R + \mathcal{V}_L)\mathcal{V}_1 \\ \mathcal{S}_{LL} &= \frac{1}{2}(\mathcal{V}_R + \mathcal{V}_L) \\ \mathcal{S}_{RL} &= -\frac{i}{2}\mathcal{V}_2(\mathcal{V}_R - \mathcal{V}_L) \\ \mathcal{S}_{LR} &= \frac{i}{2}(\mathcal{V}_R - \mathcal{V}_L)\mathcal{V}_1. \end{aligned} \tag{5.14}$$

Equations (5.13) and (5.14) are identical to Eqs. (17) and (18) of Ref. [73], where it is also shown that for any given unitary matrix $\mathcal{U}_{so} \in U(4)$ one can find four unitary matrices $\mathcal{V}_1, \mathcal{V}_R, \mathcal{V}_L, , \mathcal{V}_2 \in U(2)$ such that $\mathcal{U}_{so}$ has the form (5.13) with (5.14). It is worth noting that all manipulations in our SO-UUG are made on the photon spin degree of freedom, and that QPs are used to transfer the required operations to the OAM degree of freedom, as in Ref. [50].

One SO-UUG can perform any $U(4)$ transformation in the SO space with $\ell = \pm 2$. However, many nontrivial operations can be realized with simpler devices. For example, a straightforward calculation shows that one QB with a half-wave plate inside is enough to implement the c-NOT operator on our

logical state ($|00\rangle \to |00\rangle, |01\rangle \to |01\rangle, |10\rangle \to |11\rangle, |11\rangle \to |10\rangle$). A more common set of logical states in the photon spinorbit space is the set where the first bit corresponds to the photon spin and the second bit to the photon OAM:

$$\begin{aligned} |0,0\rangle &= |1_\pi, 2_o\rangle, \quad |0,1\rangle = |1_\pi, -2_o\rangle \\ |1,0\rangle &= |-1_\pi, 2_o\rangle, \quad |1,1\rangle = |-1_\pi, -2_o\rangle. \end{aligned} \tag{5.15}$$

In this "natural" set of basis states, the action of our SO-UUG is different. For example, the matrix $\mathcal{Q}_n$ associated to a single QB in the "natural" states basis assumes the form

$$\mathcal{Q}_n(\mathcal{V}_\pi) = \begin{pmatrix} 1 & 0 & 0 & 0 \\ 0 & v_{11} & v_{12} & 0 \\ 0 & v_{21} & v_{22} & 0 \\ 0 & 0 & 0 & 1 \end{pmatrix} \tag{5.16}$$

in place of Eq. (5.11). This way, the single QB which realizes the c-NOT operation in the logical states basis (5.3), on the states (5.15) performs the swapping operation ($|00\rangle \to |00\rangle, |01\rangle \to |10\rangle, |10\rangle \to |01\rangle, |11\rangle \to |11\rangle$). Since the choice (5.15) of states is the most used in the literature, we will use this "natural" basis hereafter. The swapping gate is very useful, because it allows one to transfer any unitary action made on the spin qubit to the OAM qubit. For example, a gate mapping basis states into equal-weight maximally entangled orthogonal superpositions (called Hadamard gate), for the single-qubit in the spin degree of freedom, is simply realized by a QWP oriented at 45°. Insertion of the swapping gate after the QWP yields a Hadamard gate acting onto the OAM qubit, leaving the spin qubit unchanged for future manipulation. A Hadamard gate for general ququarts can be realized with three QBs by setting $\mathcal{V}_1 = \sigma_y, \mathcal{V}_2 = i\sigma_z, \mathcal{V}_L = \sigma_x, \mathcal{V}_R = 1$.

Another useful gate is the c-NOT gate. The c-NOT gate, realized by UUG, can be either a spin-controlled or a OAM-controlled NOT gate. The difference between them is whether the control bit is encoded in the SAM qubit or in the OAM qubit, respectively. These two gates are given by Eqs. (5.13) and (5.14) with $\mathcal{V}_1 = -i\sigma_x, \mathcal{V}_2 = i\sigma_x, \mathcal{V}_L = \sigma_z, \mathcal{V}_R = 1$ for the spin c-NOT and $\mathcal{V}_1 = -i, \mathcal{V}_2 = i, \mathcal{V}_L = \sigma_z, \mathcal{V}_R = 1$ for the OAM c-NOT, respectively. These gates are very useful in most quantum optics applications because of their universality.

A measurement of Bell states can be performed with a gate, which transforms Bell state basis in the natural one, where each state can be separated by common devices. The Bell's state measurement gate is provided by $\mathcal{V}_1 = 1, \mathcal{V}_2 = i\sigma_y, \mathcal{V}_L = \mathcal{V}_R = 1/\sqrt{2}(1 - i\sigma_y)$. This gate unties the entanglement between the photon SAM and OAM allowing to measure the two degrees of freedom separately.

Here we have listed just few of most useful gates indicating how they can be implemented. It is worth noting, however, that the implementation of

a gate is not unique, and the gates presented here can be realized, in some cases, in simpler ways.

A final issue to be addressed to is the "crosstalk" among radial modes taking place in our device. This effect lowers, in general, the overall quality of the QB (and hence of the SO-UUG) and must be maintained at tolerable levels. As it can be seen from Eq. (5.10), when some overlap of $\ell = 0$ and $\ell = \pm 4$ modes is present, crosstalk terms appear in the QB.

We made an evaluation of the effects due to the radial cross-talk in the case of the swapping gate (one QB with half-wave semibirefringent plate), using the radial Laguerre-Gauss mode LG_{02} profile as input [20]. The radial field profiles of the $\ell = 0$ and $\ell = \pm 4$ OAM components of the beam in the back focal plane of the first lens are shown in Fig. 5.2. We notice that, although the main part of the power of the $\ell = 0$ component is concentrated at the beam center, where the $\ell = \pm 4$ component vanishes, a small crosstalk is present due to the Airy secondary maxima of the $\ell = 0$ mode. As indication of the quality of the QB as an element of the unitary gate we used the "fidelity" of the photon state $|\psi_{real}\rangle$ produced by the swapping QB with respect to the state $|\psi_{ideal}\rangle$ that an ideal QB would have produced. The fidelity F is here defined by $F = |\langle\psi_{real}|\psi_{ideal}\rangle|$. The input photon state and the expected state from an ideal swapping gate are given by

$$|\psi_{in}\rangle = (a|0,0\rangle + b|0,1\rangle + c|1,0\rangle + d|1,1\rangle)|\mathrm{LG}_{02}\rangle \tag{5.17}$$

and

$$|\psi_{ideal}\rangle = (a|0,0\rangle + c|0,1\rangle + b|1,0\rangle + d|1,1\rangle)|\mathrm{LG}_{02}\rangle \tag{5.18}$$

respectively. The ideal QB given by Eq. (5.16) with $\mathcal{V}_\pi = \sigma_x$ has 100% fidelity with respect to the output state ψ_{ideal}. However, the action of a real swapping gate on the input state (5.17) is described by

$$\begin{aligned}
&(a|0,0\rangle + b|0,1\rangle + c|1,0\rangle + d|1,1\rangle)|\mathrm{LG}_{02}\rangle \overset{Swap}{\rightarrow} \\
&(a|0,0\rangle + c|0,1\rangle + b|1,0\rangle + d|1,1\rangle)|\mathrm{LG}_{02}\rangle - \\
&[(c-b)(|1,0\rangle + |0,1\rangle)\widehat{J}_0(\widehat{I} - \widehat{U}(R))\widehat{J}_0 - \\
&(a(|0,0\rangle - |-1_\pi, 6_o\rangle) + \\
&d(|1,1\rangle - |1_\pi, -6_o\rangle))\widehat{J}_4\widehat{U}(R)\widehat{J}_4]|\mathrm{LG}_{02}\rangle
\end{aligned} \tag{5.19}$$

Assuming b and c to be real-valued, we can pose ($x^2 = 1 - a^2 - d^2$)

$$b = x\cos\theta, \quad c = x\sin\theta. \tag{5.20}$$

The swapping gate fidelity function is then given by

$$F = |1 - x^2(1 - \sin 2\theta)(1 - \gamma_0(R)) - (1 - x^2)\gamma_4(R)| \tag{5.21}$$

where $\gamma_\ell(R) = \langle \mathrm{LG}_{02}|\widehat{J}_\ell\widehat{U}(R)\widehat{J}_\ell|\mathrm{LG}_{02}\rangle$ account for the radial mode cross-talk. The parameters $\gamma_\ell(R)$ depend on the radius R of the active disk of the

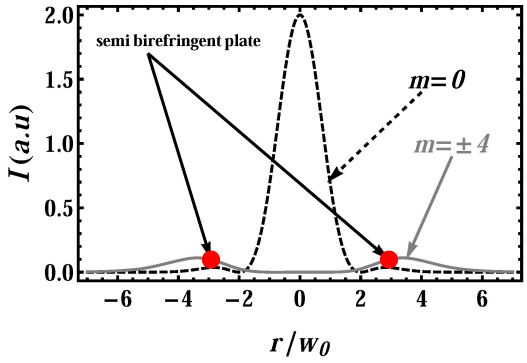

Figure 5.2: The transverse intensity profiles produced by an incident LG_{02} beam at the back focal plane of the first lens in Fig. 5.1, where the semi-birefringent plate is inserted. The two curves have been normalized to unit area, for better showing the mode crosstalk.

SBP inserted in the QB. In the case of the ideal QB, we have $\gamma_0(R) \to 1$, $\gamma_4(R) \to 0$, and $F \to 1$. We notice that the fidelity F given by Eq. (5.21) depends on the input state of the photon. The knowledge of the state to be swapped allows us to select the radius R of the birefringent disk so as to have maximum fidelity (that can vary from 83% to almost 100%, in some cases). A good compromise, however, can be obtained choosing $R = 2.928$ (in units of beam waist at the back focal plane), which gives us a flat minimum fidelity of 83.7% for *any* input state. Among the other ways to increase the fidelity of QB, one could, for example, put a non-transparent belt around the birefringent disk in order to absorb the photons in the mode-overlapping region. This method can increase the fidelity of the QB up to 100% at the price of decreasing transmission efficiency of the device. Another method could be to adjust the input beam profile or improving the design of the q-plate so as to minimize crosstalk of $\ell = 0$ and $\ell = \pm 4$ modes. The use of higher-order OAM modes could also help. We finally note that the full spinorbit UUG has many reflecting surfaces (about 70) so that high quality multireflection coating of all surfaces is highly desirable,since with the 1% reflection at each surface the total transmittance of the UUG is reduced to about 50%. With 0.1% reflection, the transmittance can be still larger than 90%.

5.3 Hybrid entanglement and Bell's inequalities [74]

Quantum entanglement became one of the most intriguing quantum mechanics paradoxes that immediately after its discovery by Einstein, Podolsky and Rosen [75] and with time they became a central point of discussion of the nature and interpretation of the quantum mechanics and becaabe essential

for many proposed quantum information and cryptography algorithms and experiments, from the wide-known, like the quantum teleportation [76] and superdence coding, to less popular, but nevertheless exciting, like Vaidman–Aharonov–Albert puzzle [77]. Entangled quantum states are also the basis of Bell's inequality violations, which ruled out classical hidden-variable theories in favor of quantum mechanics [78]. Bell's inequalities were originally derived for two particles, as a consequence of locality and realism. In almost all experimental demonstrations of these inequalities to date, the same degree of freedom of two particles has been used, e.g. the spin of a photon. Very recently, however, the case of so-called "hybrid entanglement", occurring when the involved degrees of freedom of the two particles are not the same, has attracted a certain interest, and the first experimental demonstrations with spin and spatial-mode degrees of freedom have been reported [79, 80]. Using different degrees of freedom also opens up another opportunity, i.e. that of realizing entanglement between different degrees of freedom of a single particle. In this case, no role is played by non-locality, but Bell-type inequalities can still be formulated by assuming realism and the so-called "non-contextuality" of the two involved observables, i.e. the assumption that the result of a particular measurement of one observable is determined independently of any simultaneous measurement of the other one [81, 82].Non-contextual hidden variable models have been excluded by recent experiments where the violation of suitable inequalities was observed using neutrons [83], ions [84], and single photons prepared in entangled spin-path states [85]. Finally, single-particle entanglement, in the case of bosons such as photons, has a "classical analog" that is obtained by replacing single-photon states with multi-photon coherent states realized within the same field mode [86]. Such a classical analog helps visualizing the nature of the single-particle entanglement.

SAM and OAM spaces provide a particularly convenient framework in which these concepts can be explored. In our work, we studied three conceptually re- lated experimental situations. Firstly, heralded single photons are prepared in a state where SAM and OAM are entangled, and are then used for testing the contextuality of different degrees of freedom of the same particle. Secondly, correlated photon pairs, where the SAM of one photon is entangled with the OAM of the other, i.e. photon pairs exhibiting SAM-OAM hybrid entanglement, are generated and used for testing the contextuality and non-locality of these degrees of freedom when they are spatially separated. Finally, optical coherent states involving many photons, are used to demonstrate a classical analog of SAM-OAM hybrid entanglement. The experimental layout we used in the quantum regime (the first two experiments) is presented in Fig 5.3. Our down-conversion source generates photon pairs that are entangled in the OAMdegree of freedom [88, 87], each photon

being horizontally polarized, as described by

$$|\psi\rangle = \sum_{\ell=-\infty}^{\infty} c_{|\ell|}|\ell\rangle^A|-ell\rangle^B|H\rangle^A|H\rangle^B. \tag{5.22}$$

Here A and B denote the signal and idler photons travel- ing along the two corresponding arms of the setup shown in Fig. 5.3.

a. Single-photon experiment. In this case we used photon B to herald a single photon A which we convert into an OAM-SAM maximally entangled state. Starting from state $|\psi\rangle$ given in Eq. (5.22), we post-selected photon pairs having $\ell = 0$, i.e. in state $|\psi\rangle = |0\rangle^A|0\rangle^B|H\rangle^A|H\rangle^B$, by coupling photon B into a single-mode optical fiber. Photon A is thus also projected into $\ell = 0$. Spatial light modulator SLM B in this case is patterned as a uniform grating, deflecting the beam but not affecting its transverse spatial mode (see upper-right inset of Fig. 5.3). Photon A is sent first through a q-plate so as to generate the maximally entangled SAM-OAM state [50]

$$|\Phi^+\rangle^A = \frac{1}{\sqrt{2}}\left(|R\rangle^A|+2\rangle^A + |L\rangle^A|-2\rangle^A\right). \tag{5.23}$$

The polarization state of A photons emerging from the q-plate is then measured by a half-wave plate (HWP) oriented at a variable angle $\theta/2$ and a fixed linear polarizer, restoring the horizontal polarization. This HWP-polarizer combination filters incoming photons having linear polarization at angle θ with respect to the horizontal direction. In the circular polarization basis, the state of the filtered photons is written as $|\theta\rangle_\pi = \frac{1}{\sqrt{2}}\left(e^{i\theta}|L\rangle + e^{-i\theta}|R\rangle\right)$. The SAM measurement does not affect the OAM degree of freedom. Non-contextuality can be assumed between the z-component of photon SAM and OAM, because, in the paraxial approximation, the SAM operator $\hat{S}_z$ commutes with the OAM operator $\hat{L}_z$. After SAM filtering, the photon OAM is also measured by a suitable computer-generated hologram, displayed on SLM A, followed by coupling into a single-mode fiber. The hologram pattern is defined by the four-sector alternated π-shift phase structure shown in the upper-right inset of Fig. 5.3, with the four sectors rotated at a variable angle χ (the grating fringes are not rotated). On diffraction, this hologram transforms the photons arriving in the OAM superposition state $|\chi\rangle = \frac{1}{\sqrt{2}}\left(e^{2i\chi}|+2\rangle + e^{-2i\chi}|-2\rangle\right)$ back into the $\ell = 0$ state, which is then filtered by coupling in fiber. The OAM superposition state $|\chi_\ell\rangle$ is the spatial mode analog of the linear polarization, and we may refer to its angle χ as to its "orientation" [1]. The overall effect of our apparatus is therefore to perform a joint measurement of the polarization and spatial mode orientations of A photons at angles θ and χ, respectively. When a A photon is in

[1] As was already mentioned, this spatial state corresponds to a hypergeometric-gaussian mode [20] having the same azimuthal profile as a Hermite-Gauss mode (1,1) rotated at angle χ with respect to the horizontal plane.

the entangled Bell state described by Eq. (5.23), we expect that the final probability to detect it (in coincidence with the B trigger photon) is given by

$$P(\theta,\chi) = |{}^{A}\langle\Phi^{+}| \cdot |\theta\rangle^{A}|\chi\rangle^{A}|^{2} \propto \cos^{2}(\theta - 2\chi). \tag{5.24}$$

To test entanglement we have adopted the Clauser-Horne-Shimony-Holt (CHSH) inequality, given by

$$S = |E(\theta,\chi) - E(\theta,\chi') + E(\theta',\chi) + E(\theta',\chi')| \leq 2, \tag{5.25}$$

where $E(\theta,\chi)$ is calculated from the A-B photon coincidence counts $C(\theta,\chi)$ according to

$$E(\theta,\chi) = \frac{C(\theta,\chi) + C(\theta+\frac{\pi}{2},\chi+\frac{\pi}{4}) - C(\theta+\frac{\pi}{2},\chi) - C(\theta,\chi+\frac{\pi}{4})}{C(\theta,\chi) + C(\theta+\frac{\pi}{2},\chi+\frac{\pi}{4}) + C(\theta+\frac{\pi}{2},\chi) + C(\theta,\chi+\frac{\pi}{4})}. \tag{5.26}$$

Whilst the CHSH inequality is commonly applied to non-local measurements on two spatially separated entangled photons, testing for hidden variable theories, here we apply it to single-photon entanglement to test for non-contextuality. In Fig. 5.4 (a) the coincidence counts are shown as a function of spatial mode orientation χ for different values of polarization angles θ. The occurrence of high-visibility fringes indicates the (single-particle) entanglement in the SAM-OAM spaces. The CHSH S value calculated from this data is shown in Fig. 5.5 (green dots). A violation of the CHSH inequality is clearly obtained, in good agreement with quantum theory predictions, confirming the entanglement and providing a demonstration of quantum SAM-OAM contextuality for single photons.

b. Two-photon experiment. In this case, we generated and verified entanglement between the SAM of one photon and the OAM of the other, i.e. we demonstrate non-local hybrid entanglement in these two degrees of freedom. To this purpose, the four-sector and uniform holograms of arms **A** and **B** were swapped, as displayed in the top-right inset of Fig. 5.3. The q-plate in arm **A** and the sector hologram in arm **B** of the apparatus, together with subsequent coupling into the single-mode fiber before detection, act so as to post-select the photons with $\ell = \pm 2$ in Eq. (5.22), i.e. the post-selected initial two-photon state is $|\psi\rangle = \frac{1}{\sqrt{2}}\left(|2\rangle^{A}|-2\rangle^{B} + |-2\rangle^{A}|2\rangle^{B}\right)|H\rangle^{A}|H\rangle^{B}$. The A photons pass through the q-plate, acting in this case as a OAM-to-SAM transferrer [50], so that the OAM eigenstates $\ell = \pm 2$ are mapped into L and R polarized photons with $\ell = 0$, respectively. After this process, the photon pair is projected into the nonlocal state

$$|\phi\rangle_{nl} = \frac{1}{\sqrt{2}}\left(|L\rangle^{A}|+2\rangle^{B} + |R\rangle^{A}|-2\rangle^{B}\right)|0\rangle^{A}|H\rangle^{B} \tag{5.27}$$

where the SAM of one photon is maximally entangled with the OAM of the other. Next, the polarization of the A photon is measured by the HWP

rotated at angle $\theta/2$ followed by the polarizer, and the spatial mode of the B photon by the sector hologram rotated at angle χ followed by coupling in fiber. Well-defined coincidence fringes with visibility up to 90% are obtained, as shown in Fig. 5.4 (b). Repeating the measurements for different angles θ and χ, the quantity S was evaluated from Eqs. (5.25) and (5.26) and the violation of the CHSH inequality was verified, as shown in Fig. 5.5 (blue dots). This violation provides a demonstration of SAM-OAM entanglement and non-locality, for separated photon pairs.

c. Classical light experiment. In our final experiment, we move to a classical regime of non-separable optical modes occupied by many photons, corresponding to coherent quantum states. A 100 mW frequency-doubled linearly-polarized continuous wave Nd:YVO_4 laser beam is sent in a optical line equal to arm **A** of our quantum apparatus, so as to obtain, after the q-plate, a coherent state in the SAM-OAM non-separable mode $|\Phi^+\rangle$ given by Eq. (5.23) [2]. The calculated structure of this mode is shown in Fig. 5.4(d), for a given input polarization. The mode non-separability is evident, as the polarization is spatially non-uniform [89]. The beam polarization was then filtered by the combination of the HWP at angle θ and polarizer and its spatial mode by the sector hologram rotated at angle χ, as in the single-photon experiment (a). In this case, no trigger is used and the count rates $C(\theta, \chi)$ in Eq. (5.26) are replaced by average power measurements, corresponding to photon fluxes. When the angles θ and χ are changed, high contrast sinusoidal fringes proportional to $\cos^2(\theta - 2\chi)$ were observed in the overall transmitted power fraction, as shown in Fig. 5.4c. This data can be also used to calculate a classical-equivalent to the S value with Eq. (5.25), that again violates the CHSH inequality, as shown in Fig. 5.5 (red dots). We note that the classical experiment is essentially identical to the single photon experiment, except for the random number and timing of the photons. If the existence of photons and the correspondence between optical intensity and photon flux is assumed "a priori", then this last experiment can be given the same interpretation as for the first (case a). However, the same experiment can be of course also interpreted without assuming the existence of photons. In this case, SAM and OAM measurements can be understood just as wave filtering procedures, and no conclusion can be drawn about discrepancies between classical-realistic and quantum behavior. Nevertheless, providing a classical analog of single-particle entanglement is interesting in itself and may offer the basis for some entirely classical implementations of quantum computational tasks [90].

[2] We note that, when the classical states are described as coherent quantum states, the state of the non-separable mode $|\alpha_{\Phi^+}\rangle$ is found to be decomposable in the direct product of the coherent states of the two SAM-OAM eigenmodes $|\frac{1}{\sqrt{2}}\alpha_{(R,2)}\rangle$ and $|\frac{1}{\sqrt{2}}\alpha_{(L,-2)}\rangle$, so that no SAM-OAM photon entanglement is actually present in the beam [89].

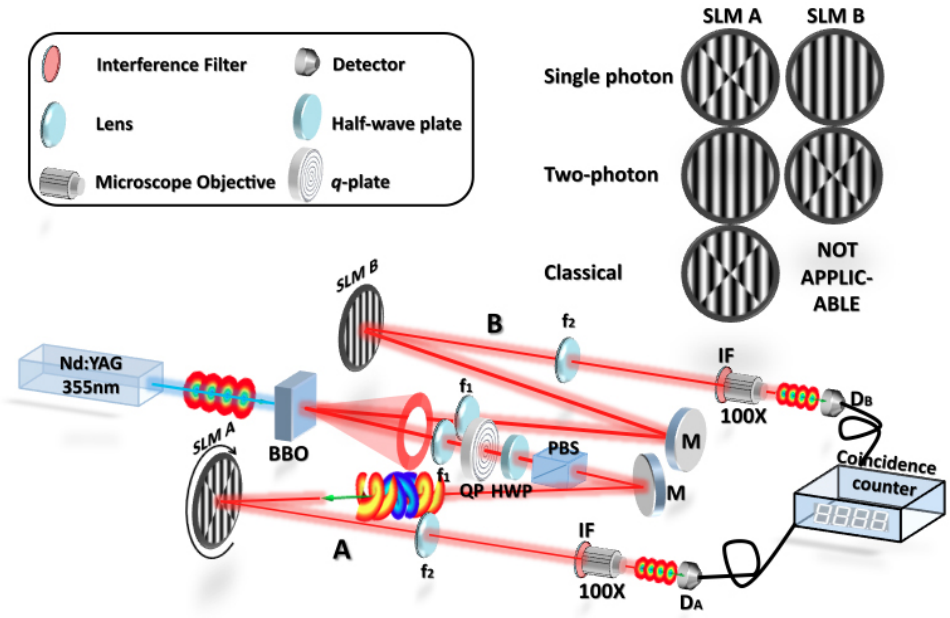

Figure 5.3: Setup used for the two quantum-regime experiments. A Nd:YAG laser with average power of 150 mW at 355 nm pumps a nonlinear crystal of β-barium borate crystal (BBO) cut for degenerate type-I non-collinear phase matching which emits OAM-entangled H-polarized photon pairs at 710 nm (see Ref. [87] for details). The photons of each pair are split in arms **A** and **B**, respectively. Legend of the main components (see also graphic symbol legend in the upper-left inset): f_1, f_2 - lenses for beam control; QP - q-plate; HWP - half-wave plate; PBS - polarizer; M - mirror; SLM A and SLM B - spatial light modulators; IF - interference filter for bandwidth definition; 100X - microscope objectives for fiber coupling; D_A, D_B - photon detectors. In the classical-regime experiment, the optical line is the same as arm **A**. Top-right inset: computer-generated hologram patterns displayed on the two SLMs in the three experiments.

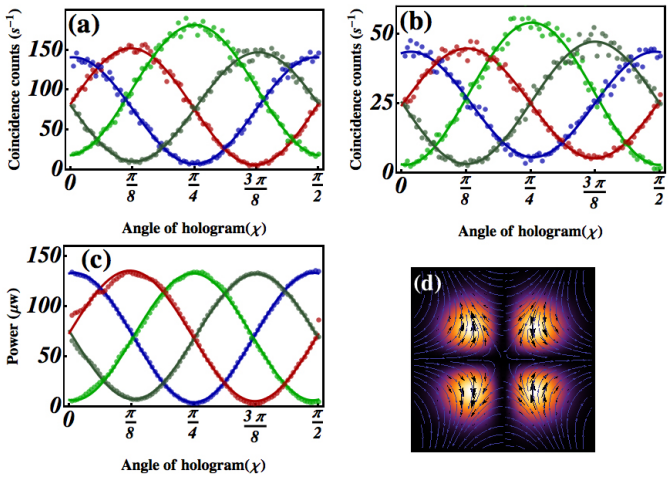

Figure 5.4: The experimental coincidence counts as a function of orientation of the sector hologram for different values of polarization direction, for heralded single photons (a), photon pairs (b) and coherent-states (c): blue dots - $\theta = 0$, red dots - $\theta = \pi/4$, green dots - $\theta = 2\pi/4$, gray dots - $\theta = 3\pi/4$. The solid lines are the best theoretical fit over the experimental data. The fringe contrast is about 90%, which is much larger than 70.7%, as required for Bell's inequality verification. (d) Simulated intensity and polarization distribution patterns of the optical field for the beam emerging from the q-plate in the case of horizontal polarization input beam.

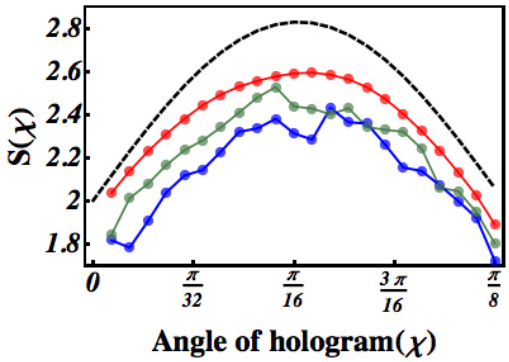

Figure 5.5: The CHSH S value in a region where it is larger than the classical limit 2. The choice of the variables appearing in Eq. (5.25) is the following: $\theta = 0$, $\theta' = \pi/4$, χ is the plot abscissa, $\chi' = \chi + \pi/8$. The green, blue, and red dots correspond to the experimental data in the case of single-photon, photon-pairs, and classical-wave SAM-OAM entanglement, respectively. The dashed line is the quantum mechanics ideal prediction. In the three cases, at $\chi = \pi/16$, the CHSH inequality is violated respectively by 17, 10, and 52 standard deviations.

Conclusions

Orbital angular momentum of light, being thoroughly studied during last two decades, still must overcome some obstacles. While numerous proposed applications based on the light OAM have significant advantages, compared with the polarization degree of photons, or are even not realizable by other means, the main problem for now is the lack of efficient, cheap and versatile devices to generate and manipulate this degree of freedom. A good candidate for this role is the q-plate and q-plate-based devices. This thesis had two main aims: first – to develop further the q-plate technology by introducing new materials and techniques for q-plate manufacturing, second – to demonstrate the versatility of this device in generating and manipulating the OAM of light.

An important step was to exploit the photoalignment technique for the q-plate fabrication in place of the previous rubbing methods. Photoalignment does not require any mechanical contact with the glass substrates during the manufacturing process, providing thus a higher quality of the liquid crystal alignment and allows to induce the topological charge once the sample is assembled, eliminating the need of precise superimposing of the singularities, imprinted in the two glass substrates. This lead to a better defined pattern of the optical axis distribution and decreases the central defect of the q-plate. While these advantages resulted in an increased quality of the q-plates, the main advantage of the photoalignment was the possibility to induce any topological charge to the cell, while rubbing is limited only to the circularly symmetric $q = 1$ charge. Between the different topological charges that were manufactured in this thesis work the $q = 0.5$ sample is of the particular interest, since it generates the lowest OAM mode $|\ell| = 1$.

The further possibility of tuning the optical phase retardation with electric field was demonstrated too. Compared with the previously introduced thermal tuning, the electric tuning not only increases the handiness of the q-plate efficiency manipulation, but allows to perform new tasks where real-time handling of OAM $|0\rangle_o$ and $|\pm\ell\rangle_o$ eigenstates superpositions is needed. With the electric tuning, it was possible to achieve conversion efficiencies up to 99% for any desired wavelength and real-time switching of the q-plates at speeds up to tens of milliseconds. Thanks to the STOC process, q-plates act as an interface between polarization and OAM degrees of freedom. Per-

forming all the necessary operations on the polarization state of photons and then transferring them into the OAM degree of freedom allows to adopt all devices for polarization manipulation into the orbital angular momentum space. To demonstrate the versatility of this idea a number of q-plate-based devices was proposed and demonstrated.

STOC process was also exploited to achieve an easy, fast, and continuous control on the transverse modes of a laser beam. A particular Dove prism-based Sagnac polarizing interferometric configuration allowed us to generate with efficiency higher than 90% arbitrary combinations of LG_2 modes, by changing the polarization of the input $\mathrm{TEM}_0 0$ linearly polarized laser beam. When closed paths are described on the SAM Poincaré sphere, identical closed path are described on the OAM Poincaré sphere and the resulting Pancharatnam geometric phase is transferred with no change from the SAM to the OAM degree of freedom.

Another device proposed in this thesis is a q-plate-based optical loop, that allowed to generate and encode two bits of classical information into the OAM of a single photon. Furthermore, the optical loop can be easily modified to encode three bits of information in a single photon by adding an additional polarization bit. The same setup allows also to generate qubits made of two different OAM orders or qudits with infinite number of OAM eigenstates. The generation process of single OAM eigenstates, OAM qubits and OAM qudits with $d = \infty$ is deterministic, has nominal 100% efficiency, and the output OAM state can be controlled (even if not completely) by very fast electro-optical devices. The encoding process, based once more on the STOC process is very efficient (nominal efficiency is 100%) and very fast. The information encoded in the light beam can be read with a computer generated hologram properly designed to detect all four OAM states simultaneously or by a second q-plate based device.

Both the Sagnac interferometer and the q-plate loop device work both in the classical and quantum regimes of light. In both cases the process is fully controlled by polarization only and can be driven by fast electro-optical devices which provide operation frequencies never achievable by SLM (that operates at the rates no more than a few KHz).

The Polarizing Sagnac Interferometer was studied separately as a device able to enhance the performance of the q-plate and to perform not trivial manipulations in the spinorbit space such as OAM modes sorting or realize quantum unitary gates such as OAM C-NOT gate, full Bell's states detection gate, a gate to generate Schmidt's photon states with controllable spinorbit entanglement and others. The PSI is more stable than Mach-Zehnder interferometers because of the self-compensated optical paths and it is easier to use because it requires only one Dove prism.

Another q-plate based device, the Universal Unitary Gate for 4D spinorbit space of photons was also proposed. This adjustable gate is able to perform any unitary operation in single photon spinorbit space. UUG is

highly transparent, which guarantees a high photon transmission efficiency, and can be inserted along the beam path in as much the same way as other optical components are inserted without changing the beam direction. This allows us to perform nontrivial two-qubit handling with optical assemblies having much less overall size and much more stability against environmental noise than interferometers. Although the proposed UUG is not beyond the technological possibilities nowadays available, its practical manufacturing presents many difficulties, so it was postponed to future work. Nevertheless, the UUG could have an impact in all fields where a complete manipulation of the light OAM and polarization is needed such as, for instance, in optical tweezers and traps, optical communications, optical computing, and fundamental quantum optics.

Finally, q-plates were used to create hybrid entanglement of the spin and the orbital angular momentum of light in three different regimes: single photons, entangled photon pairs, and classical many-photon modes. Although the experimental results appear very similar in the three analyzed regimes they provide different and complementary insight into the contextual and non-local quantum nature of light.

List of publications related to the thesis

[1]- **S. Slussarenko**, E. Karimi, B. Piccirillo, L. Marrucci and E. Santamato, Universal unitary gate for single-photon spin-orbit four-dimensional states, *Phys. Rev. A.* **80**, 022326 (2009).

[2]- E. Karimi, **S. Slussarenko**, B. Piccirillo, L. Marrucci and E. Santamato, Polarization-controlled evolution of light transverse modes and associated Pancharatnam geometric phase in orbital angular momentum, *Phys. Rev. A.* **81**, 053813 (2010).

[3]- E. Nagali, D. Giovannini, L. Marrucci, **S. Slussarenko**, E. Santamato, and F. Sciarrino, Experimental optimal cloning of four-dimensional quantum states of photons, *Phys. Rev. Lett.* **105**, 073602 (2010).

[4]- E. Karimi, J. Leach, **S. Slussarenko**, B. Piccirillo, L. Marrucci, L. Chen, W. She, S. Franke-Arnold, M. J. Padgett, and E. Santamato, Spin-orbit hybrid entanglement of photons and quantum contextuality, *Phys. Rev. A* **82**, 022115 (2010).

[5]- **S. Slussarenko**, V. D'Ambrosio, B. Piccirillo, L. Marrucci, E. Santamato, The Polarizing Sagnac Interferometer: a tool for light orbital angular momentum sorting and spin-orbit photon processing, *Opt. Express* in press

[6]- **S. Slussarenko**, E. Karimi, B. Piccirillo, L. Marrucci and E. Santamato, Efficient generation and control of different order orbital angular momentum states for communication links, *J. Opt. Soc. Am. A* in press

[7]- B. Piccirillo, V. D'Ambrosio, **S. Slussarenko**, L. Marrucci and E. Santamato, Photon spin-to-orbital angular momentum conversion via an electrically tunable q-plate, *arXiv:1010.4473*, *Appl. Phys. Lett.* in press

[8]- **S. Slussarenko**, A. Murauski, T. Du, V. Chigrinov, L. Marrucci and E. Santamato, Tunable liquid crystal q-plates with arbitrary topological charge, submitted.

Bibliography

[1] J. H. Poynting. The Wave Motion of a Revolving Shaft, and a Suggestion as to the Angular Momentum in a Beam of Circularly Polarised Light. *Proc. Roy. Soc. Lond. A*, 82(557):560–567, 1909.

[2] Richard A. Beth. Direct detection of the angular momentum of light. *Phys. Rev.*, 48(5):471, Sep 1935.

[3] Richard A. Beth. Mechanical detection and measurement of the angular momentum of light. *Phys. Rev.*, 50(2):115–125, Jul 1936.

[4] L. Allen, M. W. Beijersbergen, R. J. C. Spreeuw, and J. P. Woerdman. Orbital angular momentum of light and the transformation of Laguerre-Gaussian laser modes. *Phys. Rev. A*, 45(11):8185–8189, 1992.

[5] O. T. A. O'Neil, I. MacVicar, L. Allen, and M. J. Padgett. Intrinsic and extrinsic nature of the orbital angular momentum of a light beam. *Phys. Rev. Lett.*, 88(5):053601, 2002.

[6] G. Gibson, J. Courtial, M. J. Padgett, M. Vasnetsov, V. Pasko, S. M. Barnett, and S. Franke-Arnold. Free-space information transfer using light beams carrying orbital angular momentum. *Opt. Express*, 12(22):5448–5456, 2004.

[7] B. Thidé, H. Then, J. Sjöholm, K. Palmer, J. Bergman, T. D. Carozzi, Ya. N. Istomin, N. H. Ibragimov, and R. Khamitova. Utilization of photon orbital angular momentum in the low-frequency radio domain. *Phys. Rev. Lett.*, 99(8):087701, Aug 2007.

[8] Alois Mair, Alipasha Vaziri, Gregor Welhs, and Anton Zeilinger. Entanglement of the angular momentum states of photons. *Nature*, 412:313–315, 2001.

[9] Martin Harwit. Photon orbital angular momentum in astrophysics. *The Astrophysical Journal*, 597(2):1266, 2003.

[10] D. Sanvitto, F. M. Marchetti, M. H. Szymanska, G. Tosi, M. Baudisch, F. P. Laussy, D. N. Krizhanovskii, M. S. Skolnick, L. Marrucci,

A. Lemaitre, J. Bloch, C. Tejedor, and L. Vina. Persistent currents and quantized vortices in a polariton superfluid. *Nature Physics*, 6(7):527–533, JUL 2010.

[11] M. F. Andersen, C. Ryu, Pierre Cladé, Vasant Natarajan, A. Vaziri, K. Helmerson, and W. D. Phillips. Quantized rotation of atoms from photons with orbital angular momentum. *Phys. Rev. Lett.*, 97(17):170406, Oct 2006.

[12] L. Allen, S. M. Barnett, and M. J. Padgett. *Optical angular momentum.* Institute of Physics Publishing, Bristol, 2003.

[13] L. Allen, M. J. Padgett, and M. Babiker. The orbital angular momentum of light. *Prog. Opt.*, 39:291–372, 1999.

[14] A. S. Desyatnikov, Y. S. Kivshar, and L. Torner. Optical vortices and vortex solitons. *Prog. Opt.*, 47:291, 2005.

[15] Miles J. Padgett, Johannes Courtial, and Les Allen. Light's orbital angular momentum. *Phys. Today*, 57(5):35–40, 2004.

[16] M. S. Soskin and M. V. Vasnetsov. Singular optics. *Prog. Opt.*, 42:219–276, 2001.

[17] Enrico Santamato. Photon orbital angular momentum: problems and perspectives. *Fortschr. Phys.*, 52(11-12):1141–1153, 2004.

[18] L. Marrucci, C. Manzo, and D. Paparo. Optical spin-to-orbital angular momentum conversion in inhomogeneous anisotropic media. *Phys. Rev. Lett.*, 96:163905, 2006.

[19] L. Marrucci, C. Manzo, and D. Paparo. Pancharatnam-Berry phase optical elements for wavefront shaping in the visible domain: switchable helical modes generation. *Appl. Phys. Lett.*, 88:221102, 2006.

[20] Ebrahim Karimi, Gianluigi Zito, Bruno Piccirillo, Lorenzo Marrucci, and Enrico Santamato. Hypergeometric-gaussian modes. *Opt. Lett.*, 32(21):3053–3055, NOV 1 2007.

[21] E. Karimi, B. Piccirillo, L. Marrucci, and E. Santamato. Light propagation in a birefringent plate with topological unit charge. *Opt. Lett.*, 34:1225–1227, 2009.

[22] M. J. Padgett and J. Courtial. Poincaré-sphere equivalent for light beams containing orbital angular momentum. *Opt. Lett.*, 24(7):430–432, 1999.

[23] G. S. Agarwal. Su(2) structure of the poincaré sphere for light beams with orbital angular momentum. *J. Opt. Soc. Am. A*, 16(12):2914–2916, 1999.

[24] V. Y. Bazhenov, M. V. Vasnetsov, and M. S. Soskin. Laser beams with screw dislocations in their wavefronts. *Sov. Phys.–JETP Lett.*, 52:429–431, 1990. [Pis'ma Zh. Eksp. Teor. Fiz., **52**, 1037-1039 (1990)].

[25] M. W. Beijersbergen, R. P. C. Coerwinkel, M. Kristensen, and J. P. Woerdman. Helical-wavefront laser beams produced with a spiral phaseplate. *Opt. Commun.*, 112:321–327, 1994.

[26] *Collected works of S. Pancharatnam.* Oxford University Press, Oxford, 1975.

[27] M. V. Berry. Quantal Phase Factors Accompanying Adiabatic Changes. *Proceedings of the Royal Society of London. A. Mathematical and Physical Sciences*, 392(1802):45–57, 1984.

[28] R. Bhandari. Polarization of light and topological phases. *Phys. Rep.*, 281(1):1–64, 1997.

[29] Ze'ev Bomzon, Vladimir Kleiner, and Erez Hasman. Pancharatnam–berry phase in space-variant polarization-state manipulations with subwavelength gratings. *Opt. Lett.*, 26(18):1424–1426, 2001.

[30] Ze'ev Bomzon, Gabriel Biener, Vladimir Kleiner, and Erez Hasman. Space-variant pancharatnam-berry phase optical elements with computer-generated subwavelength gratings. *Opt. Lett.*, 27(13):1141–1143, 2002.

[31] Gabriel Biener, Avi Niv, Vladimir Kleiner, and Erez Hasman. Formation of helical beams by use of pancharatnam-berry phase optical elements. *Opt. Lett.*, 27(21):1875–1877, 2002.

[32] E Hasman, V Kleiner, G Biener, and A Niv. Polarization dependent focusing lens by use of quantized Pancharatnam-Berry phase diffractive optics. *Appl. Phys. Lett.*, 82(3):328–330, 2003.

[33] Ebrahim Karimi, Bruno Piccirillo, Eleonora Nagali, Lorenzo Marrucci, and Enrico Santamato. Efficient generation and sorting of orbital angular momentum eigenmodes of light by thermally tuned q-plates. *Appl. Phys. Lett.*, 94(23):231124, 2009.

[34] P. Chatelain. Orientation of liquid crystal. *Bull. Soc. Franc. Miner*, 66(105), 1943.

[35] Wayne M. Gibbons, Paul J. Shannon, Shao-Tang Sun, and Brian J. Swetlin. Surface-mediated alignment of nematic liquid crystals with polarized laser light. *Nature*, 351:49–50, May 1991.

[36] A. G. Dyadyusha, V. M. Kozenkov, T.Y. Marusii, Y. A. Reznikov, V.Y. Reshetnyak, and A. I. Khizhnyak. Light-induced planar alignment of nematic liquid-crystal by the anisotropic surface without mechanical texture. *Ukr. Fiz. Zhurnal*, 36(7):1059–1062, 1991.

[37] Martin Schadt, Klaus Schmitt, Vladimir Kozinkov, and Vladimir Chigrinov. Surface-induced parallel alignment of liquid crystals by linearly polymerized photopolymers. *Jpn. J. Appl. Phys.*, 31(Part 1, No. 7):2155–2164, 1992.

[38] Masaki Hasegawa and Yoichi Taira. Nematic homogeneous photo alignment by polyimide exposure to linearly polarized uv. *J. Photopolym. Sci. Technol.*, 8(2):241–248, 1995.

[39] Vladimir G. Chigrinov, Vladimir M. Kozenkov, and Hoi-Sing Kwok. *Photoalignment of Liquid Crystalline Materials: Physics and Applications*. Wiley Publishing, 2008.

[40] B. Piccirillo, V. DAmbrosio, S. Slussarenko, L. Marrucci, and E. Santamato. Photon spin-to-orbital angular momentum conversion via an electrically tunable q-plate. *Appl. Phys. Lett. arXiv:1010.4473*, in press.

[41] Jae-Hoon Kim, Satyendra Kumar, and Sin-Doo Lee. Alignment of liquid crystals on polyimide films exposed to ultraviolet light. *Phys. Rev. E*, 57(5):5644–5650, May 1998.

[42] S. Slussarenko, A. Murauski, T. Du, V. Chigrinov, L. Marrucci, and E. Santamato. Tunable liquid crystal q-plates with arbitrary topological charge. *submitted*.

[43] Sarik Nersisyan, Nelson Tabiryan, Diane M. Steeves, and Brian R. Kimball. Fabrication of liquid crystal polymer axial waveplates for uv-ir wavelengths. *Opt. Express*, 17(14):11926–11934, 2009.

[44] V. Friedericksz and V. Zolina. *Z. Krist.*, 79(255), 1931.

[45] Eleonora Nagali, Fabio Sciarrino, Francesco De Martini, Bruno Piccirillo, Ebrahim Karimi, Lorenzo Marrucci, and Enrico Santamato. Polarization control of single photon quantum orbital angular momentum states. *Opt. Express*, 17:18745–18759, 2009.

[46] Jonathan Leach, Miles J. Padgett, Stephen M. Barnett, Sonja Franke-Arnold, and Johannes Courtial. Measuring the orbital angular momentum of a single photon. *Phys. Rev. Lett.*, 88(25):257901, Jun 2002.

[47] Jonathan Leach, Johannes Courtial, Kenneth Skeldon, Stephen M. Barnett, Sonja Franke-Arnold, and Miles J. Padgett. Interferometric methods to measure orbital and spin, or the total angular momentum of a single photon. *Phys. Rev. Lett.*, 92(1):013601, Jan 2004.

[48] Marco Fiorentino and Franco N. C. Wong. Deterministic controllednot gate for single-photon two-qubit quantum logic. *Phys. Rev. Lett.*, 93(7):070502, Aug 2004.

[49] Ebrahim Karimi, Sergei Slussarenko, Bruno Piccirillo, Lorenzo Marrucci, and Enrico Santamato. Polarization-controlled evolution of light transverse modes and associated pancharatnam geometric phase in orbital angular momentum. *Phys. Rev. A*, 81(5):053813, 2010.

[50] Eleonora Nagali, Fabio Sciarrino, Francesco De Martini, Lorenzo Marrucci, Bruno Piccirillo, Ebrahim Karimi, and Enrico Santamato. Quantum information transfer from spin to orbital angular momentum of photons. *Phys. Rev. Lett.*, 103:013601, 2009.

[51] E. J. Galvez, P. R. Crawford, H. I. Sztul, M. J. Pysher, P. J. Haglin, and R. E.Williams. Geometric phase associated with mode transformations of optical beams bearing orbital angular momentum. *Phys. Rev. Lett.*, 90(20):203901, 2003.

[52] S. Slussarenko, V. D'Ambrosio, B. Piccirillo, L. Marrucci, and E. Santamato. The polarizing sagnac interferometer: a tool for light orbital angular momentum sorting and spin-orbit photon processing. *J. Opt. Soc. Am. A*, in press.

[53] M. J. Padgett and L. Allen. Orbital angular momentum exchange in cylindrical-lens mode converters. *J. Opt. B: Quantum Semicl. Opt.*, 4:S17–S19, 2002.

[54] Maik Frede, Ralf Wilhelm, Martina Brendel, Carsten Fallnich, Frank Seifert, Benno Willke, and Karsten Danzmann. High power fundamental mode nd:yag laser with efficient birefringence compensation. *Opt. Express*, 12:3581–3589, 2004.

[55] Efim A. Khazanov, Oleg V. Kulagin, Sanichiro Yoshida, David B. Tanner, and David H. Reitze. Investigation of self-induced depolarization of laser radiation in terbium gallium garnet. *IEEE J. Quantum Electron.*, 35:1116–1122, 1999.

[56] N. F. Andreev, O. V. Palashov, A. K. Potemkin, D. H. Reitze, A. M. Sergeev, and E. A. Khazanov. A 45-db faraday isolator for 100-w average radiation power. *Quantum Electron.*, 30:1107–1108, 2000.

[57] Lucien Hardy. Non locality for two particles without inequalities for almost all entangled states. *Phys. Rev. Lett.*, 71:1665–1668, 1993.

[58] Daniel F. V. James, Paul G. Kwiat, William J. Munro, and Andrew G. White. Measurement of qubits. *Phys. Rev. A*, 64:052312, 2001.

[59] E. Nagali, D. Giovannini, L. Marrucci, S. Slussarenko, E. Santamato, and F. Sciarrino. Experimental optimal cloning of four-dimensional quantum states of photons. *Phys. Rev. Lett.*, 105(7):073602, Aug 2010.

[60] S. Slussarenko, E. Karimi, B. Piccirillo, L. Marrucci, and E. Santamato. Efficient generation and control of different order orbital angular momentum states for communication links. *J. Opt. Soc. Am. A*, in press.

[61] Juan P. Torres, Yana Deyanova, and Lluis Torner. Preparation of engineered two-photon entangled states for multidimensional quantum information. *Phys. Rev. A*, 67:052313, 2003.

[62] A. Vaziri, J. W. Pan, T. Jennewein, G. Weihs, and A. Zeilinger. Concentration of higher dimensional entanglement: Qutrits of photon orbital angular momentum. *Phys. Rev. Lett.*, 91:227902, 2003.

[63] G. Molina-Terriza, A. Vaziri, J. Rehacek, Z. Hradil, and A. Zeilinger. Triggered qutrits for quantum communication protocols. *Phys. Rev. Lett.*, 92:167903, 2004.

[64] N. K. Langford, R. B. Dalton, M. D. Harvey, J. L. O'Brien, G. J. Pryde, A. Gilchrist, S. D. Bartlett, and A. G. White. Measuring entangled qutrits and their use for quantum bit commitment. *Phys. Rev. Lett.*, 93:053601, 2004.

[65] Eleonora Nagali, Linda Sansoni, Lorenzo Marrucci, Enrico Santamato, and Fabio Sciarrino. Experimental generation and characterization of single-photon hybrid ququarts based on polarization and orbital angular momentum encoding. *Phys. Rev. A*, 81(5):052317, May 2010.

[66] Gregorius C. G. Berkhout, Martin P. J. Lavery, Johannes Courtial, Marco W. Beijersbergen, and Miles J. Padgett. Efficient Sorting of Orbital Angular Momentum States of Light. *PHYSICAL REVIEW LETTERS*, 105(15), OCT 4 2010.

[67] Eleonora Nagali, Linda Sansoni, Fabio Sciarrino, Francesco De Martini, Lorenzo Marrucci, Bruno Piccirillo, Ebrahim Karimi, and Enrico Santamato. Optimal quantum cloning of orbital angular momentum photon qubits through hong-ou-mandel coalescence. *Nat. Photon.*, 3:720–723, 2009.

[68] Sergei Slussarenko, Ebrahim Karimi, Bruno Piccirillo, Lorenzo Marrucci, and Enrico Santamato. Universal unitary gate for single-photon spin-orbit four-dimensional states. *Phys. Rev. A*, 80(2):022326, Aug 2009.

[69] William. Swindell. *Polarized light / edited by William Swindell.* Dowden, Hutchinson & Ross ; distributed by Halsted Press, Stroudsburg, Pa. [New York], 1975.

[70] N. González, G. Molina-Terriza, and J. P. Torres. How a dove prism transforms the orbital angular momentum of a light beam. *Opt. Express*, 14(20):9093–9102, 2006.

[71] Hiroyuki Sasada and Megumi Okamoto. Transverse-mode beam splitter of a light beam and its application to quantum cryptography. *Phys. Rev. A*, 68:012323, 2003.

[72] M. W. Beijersbergen, L. Allen, H.E.L.O. van der Veen, and J. P. Woerdman. Astigmatic laser mode converters and transfer of orbital angular momentum. *Opt. Commun.*, 96:123–132, 1993.

[73] Berthold-Georg Englert, Christian Kurtsiefer, and Harald Weinfurter. Universal unitary gate for single-photon two-qubit states. *Phys. Rev. A*, 63(3):032303, Feb 2001.

[74] Ebrahim Karimi, Jonathan Leach, Sergei Slussarenko, Bruno Piccirillo, Lorenzo Marrucci, Lixiang Chen, Weilong She, Sonja Franke-Arnold, Miles J. Padgett, and Enrico Santamato. Spin-orbit hybrid entanglement of photons and quantum contextuality. *Phys. Rev. A*, 82(2):022115, Aug 2010.

[75] A. Einstein, B. Podolsky, and N. Rosen. Can quantum-mechanical description of physical reality be considered complete? *Phys. Rev.*, 47(10):777–780, May 1935.

[76] Charles H. Bennett, Gilles Brassard, Claude Crépeau, Richard Jozsa, Asher Perez, and Wiliam K. Wootters. Teleporting an unknown quantum state via dual classical and einstein-podolsky- rosen channels. *Phys. Rev. Lett.*, 70:1895–1899, 1993.

[77] Lev Vaidman, Yakir Aharonov, and David Z. Albert. How to ascertain the values of $]sigma_x$, σ_y, and σ_z of a spin-1/2 particle. *Phys. Rev. Lett.*, 58(14):1385–1387, Apr 1987.

[78] John S. Bell. Bell-inequality violations with single photons entangled in momentum and polarization. *Rev. Mod. Phys.*, 38:447–452, 1966.

[79] Xiao-song Ma, Angie Qarry, Johannes Kofler, Thomas Jennewein, and Anton Zeilinger. Experimental violation of a bell inequality with two different degrees of freedom of entangled particle pairs. *Phys. Rev. A*, 79(4):042101, Apr 2009.

[80] Leonardo Neves, Gustavo Lima, Aldo Delgado, and Carlos Saavedra. Hybrid photonic entanglement: Realization, characterization, and applications. *Phys. Rev. A*, 80(4):042322, Oct 2009.

[81] R. M. Roy and Virenda Singh. Quantum violation of stochastic noncontextual hidden-variables theories. *Phys. Rev. A*, 48:3379–3381, 1993.

[82] N.D. Mermin. Hidden variables and the two theorems of john bell. *Rev. Mod. Phys.*, 65:803, 1993.

[83] Yuji Hasegawa, Rudolf Loidl, Gerald Badurek, Matthias Baron, and Helmut Rauch. Violation of a bell-like inequality in single-neutron interferometry. *Nature*, 425:45–48, 2003.

[84] G. Kirchmair, F. Zähringer, R. Gerritsma, M. Kleinmann, O. Gühne, A. Cabello, R. Blatt, and C. F. Roos. State-independent experimental test of quantum contextuality. *Nature*, 460:494–498, 2009.

[85] B. R. Gadway, E.J. Galvez, and F. DeZela. Bell-inequality violations with single photons entangled in momentum and polarization. *J. Phys. B*, 42:015503, 2009.

[86] Robert J. C. Spreeuw. A classical analogy of entanglement. *Found. Phys.*, 28:361–374, 1998.

[87] J. Leach, B. Jack, J. Romero, M. Ritsch-Marte, R. W. Boyd, A. K. Jha, S. M. Barnett, S. Franke-Arnold, and M. J. Padgett. Violation of a bell inequality in two-dimensional orbital angular momentum state-spaces. *Opt. Express*, 17(10):8287–8293, 2009.

[88] B Jack, J Leach, H Ritsch, S M Barnett, M J Padgett, and S Franke-Arnold. Precise quantum tomography of photon pairs with entangled orbital angular momentum. *New Journal of Physics*, 11(10):103024, 2009.

[89] C. V. S. Borges, M. Hor-Meyll, J. A. O. Huguenin, and A. Z. Khoury. Bell-like inequality for the spin-orbit separability of a laser beam. *Phys. Rev. A*, 82(3):033833, SEP 28 2010.

[90] Robert J. C. Spreeuw. Classical wave-optics analogy of quantum-information processing. *Phys. Rev. A*, 63:062302, 2001.